Design considerations for synthetic cells

Thesis by
Manisha Kaushik Kapasiawala

In Partial Fulfillment of the Requirements for the
Degree of
Doctor of Philosophy in Bioengineering

CALIFORNIA INSTITUTE OF TECHNOLOGY
Pasadena, California

2026
Defended August 1, 2025

Manisha Kaushik Kapasiawala
ORCID: 0000-0002-0302-2921

ACKNOWLEDGEMENTS

Throughout my academic journey, I have had the support of many individuals — professors, colleagues, peers, friends, and family — who have helped me grow as a scientist and as a person.

I would like to begin by thanking my advisor, Richard Murray. It is rare to find a PhD advisor that will let you pursue your scientific interests almost entirely without restriction and with seemingly limitless support (both financial and moral). When I first began my PhD, I came to Caltech with lots of excitement, an abysmal set of wet lab skills, some computational interests, and zero experience in synthetic biology. I will admit I was initially a little (actually very) lost, chasing too many different ideas and quickly getting stuck at each turn. But Richard's steady support has allowed me to grow into a confident, disciplined, and curiosity-driven scientist, and for that I will forever be grateful.

I would also like to thank my other committee members, Erik Winfree, Matt Thomson, and Rebecca Voorhees. Our committee meetings were extremely helpful in encouraging me to think about how I might frame my research and its significance within the context of the field, and their feedback has been critical in maximizing the impact of my work.

In the Murray Lab, I have had the opportunity to work alongside wonderful people who are simultaneously an incredible set of bioengineers. They have each left an impact on this work — whether that impact was in the form of a collaboration, inspiration, or motivation and optimism — but I would like to highlight a few people that have truly shaped my time in the lab. Miki Yun taught me all the basic tools of synthetic biology and graciously lent an ear whenever I was stuck in a rut. William Poole first helped me as an informal mentor, even after graduating, and later as a collaborator, and our many scientific discussions culminated in the work shown in Chapters 2 and 3 of this thesis. Zoila Jurado helped me get started in the field of synthetic cell research, and she has been a wonderful person to bounce ideas off of and also go rock climbing with. Ayush Pandey helped me learn and become proficient with the various Murray Lab modeling tools. John Marken and Yan Zhang have provided incredible feedback on the work over the years, particularly on how to frame my work and identify interesting research questions, and in general have set an incredibly high bar for good science that I have only hoped to achieve; the latter is

also a good source of motivation in the gym. Matthieu Kratz has been a great office mate and a excellent person to discuss modeling with. Alex Johnson's and Zach Martinez's "crazy ideas" and unbridled optimism for synthetic cell research have inspired me to think more creatively about my own research vision. Various other Murray Lab members — especially Mark Prator — have indulged me in countless hours of board games and have created a positive social atmosphere in the lab.

I have also had the good fortune to mentor many summer students: Peter, Hannah, Alina, Robert, Citli, Grace, Jeylin, and Trinity. Beyond providing me with a creative outlet to explore research ideas that I could not explore myself, mentoring these students has shaped the way I approach, teach, and communicate research, and I thank them for giving me the opportunity to do so.

Beyond the lab, Justin Bois has profoundly shaped my standards for reproducible research and has taught many of the classes I took in my early years at Caltech that made me excited about mathematics and statistics in biology. In a similar vein, I must thank Stanislav Shvartsman and Caroline Doherty, my undergraduate advisor and graduate student mentor, respectively, for getting me excited about research in biology, teaching me a lot of the foundational tools of research, and encouraging me to apply for graduate school.

Having received so much support in my own academic and professional journey, I first sought out the Caltech Y to engage in service. I soon discovered that the Y was not just a place to give back but also a source of community, joy, and perspective. My involvement with the Y has encouraged me to think more broadly about the impact of science on society and, beyond science, shown me the difference a single person can make in their community. I have had the pleasure of working with many incredible staff members — Athena Castro, Greg Fletcher, and Liz Jackman — and students — including Manni He, Cecilia Abramson, Sulekha Kishore, and many others — at the Y, and I thank them for broadening my world view and encouraging me to pursue a career in science policy.

Outside the lab, my friends in SoCal and those scattered across the US have done incredible work to lift my spirits throughout this journey: Olivia (and Ninja, the most incredible kitty known to mankind — RIP), Annie, Robert, Kevin, Jeanne, Sarah, Sam, Erik, Val, Felix, Rhea, Jess, Glenda, Priya, Shawrav, Cai, and no doubt many others I am missing here. Besides being an awesome roommate and wonderful friend, Olivia is an excellent scientist whose discipline in the lab is one I have sought to replicate.

I am lucky enough to be surrounded by an incredible and loving family, both old and new. My parents Kaushik and Anita have instilled in me a strong sense of determination and sent their love from across the country. My siblings Akshita and Jay simultaneously confuse me and inspire me with their own career paths and other life choices, and in doing so they have taught me that there is more than one right way to do something (but also infinitely many wrong ways to do something). The Shur family, and especially Nataliya and Sergei, have provided me with good food, great conversation, much-needed comfort, and infinite love over the past few years.

Finally, I must thank Andrey, my husband and the love of my life. The countless hours we have spent outdoors — sampling fruits from random people's trees in Pasadena, buying too many succulents at the Huntington, aimlessly biking around the Arroyo admiring flowers and insects alike, traversing terrains of trees, rocks, deserts, mountains, and rivers — have reminded me to slow down and admire all that is beautiful in this world. His ability to think calmly and solve any problem in the face of chaos is one I have attempted to emulate both in my PhD and in tackling life's other challenges. I am endlessly grateful for his love and support, and I am excited for our many adventures ahead.

ABSTRACT

Efforts to understand life as we know it and life as it can be have culminated in the field of synthetic cell research, which aims to build life from the bottom up using individual biological components. Recent progress in the field has enabled the reconstitution of many functions of living cells in synthetic cells, from cell-cell communication to membrane protein expression and function. However, future progress in the field is limited by many challenges, including irreproducibility, lack of predictability, difficulties in integrating existing synthetic cell modules (or subsystems), and the need for autonomous functionalities.

In this work, I describe my efforts towards addressing these challenges. In Chapter 2, I describe sources of variability in transcription-translation (TX-TL) systems, the biological machinery used to implement biomolecular programs in synthetic cells. In Chapter 3, I describe a novel methodology for readily building more predictive models of TX-TL performance. In Chapter 4, I present a design for a proof-of-concept for integrating an energy regeneration subsystem and a motility subsystem to achieve autonomous programmable motility and highlight some early successes towards achieving that goal. Throughout this work, I highlight many design principles for building synthetic cells reproducibly, more predictably, and with novel functionalities.

PUBLISHED CONTENT AND CONTRIBUTIONS

[1] William Poole, Manisha Kapasiawala, Ankita Roychoudhury, Matthew Haines, Paul Freemont, and Richard M. Murray. "Metabolomics-informed coarse-grained model enables prediction of cell-free protein expression dynamics." In: *bioRxiv* (2025). DOI: 10.1101/2025.06.20.660830.
W.P. and M.K. contributed equally to this work. M.K. conceived, designed, and implemented the fine-tuning work with feedback from W.P. and under the supervision of R.M.M. Both M.K. and W.P. wrote the manuscript equally.

[2] Manisha Kapasiawala and Richard M. Murray. "Metabolic perturbations to an Escherichia coli-based cell-free system reveal a trade-off between transcription and translation." In: *ACS Synthetic Biology* 13.12 (2024), pp. 3976–3990. DOI: 10.1021/acssynbio.4c00361.
M.K. conceived and designed the study, performed experiments, acquired and analyzed the data, and wrote the manuscript under the supervision of R.M.M.

TABLE OF CONTENTS

Chapter 1

INTRODUCTION

1.1 Synthetic biology as a tool to understand and engineer life

Over the past few decades, synthetic biology has emerged as a powerful tool to understand and engineer life. The vast majority of synthetic biology applications rely on top-down approaches, where existing biological systems are engineered from the top down via systematic changes at the molecular level. In top-down approaches, proteins, nucleic acids, metabolic pathways, and other components are modified, added to, or removed from biological systems, which typically consist of whole cells or whole organisms. Recent examples of synthetic biology applications using top-down approaches include microorganisms engineered to upcycle plastic waste into commodity chemicals, CAR T-cell therapy for autoimmune diseases, engineering plant roots and root-associated microooorganisms (bacteria and fungi) to improve crop resilience, engineering and visualizing morphogen gradients with Green Fluorescent Protein (GFP) to understand animal development, and thousands of other applications [1–4].

While top-down approaches have had great success, using these approaches to engineer cells and organisms — which are extremely complex, poorly characterized, and often unpredictable systems — has been time-consuming, costly, and inefficient. Even *E. coli*, a model microorganism that is one of the most well-studied systems, is not always easy to engineer. Large swaths of its genome and physiology remain uncharacterized, and engineering *E. coli* to perform complex tasks still requires years of effort due to undesired interactions with non-engineered cell components and attempts by cells to resist engineering efforts. For engineering non-model cell types and organisms, these issues are exacerbated. Beyond engineering biological systems to perform a desired task, top-down synthetic biology has also had limited success in increasing our understanding of life, because large-scale perturbations to these systems result in the death of the engineered cells or organisms.

1.2 Cell-free synthetic biology as a bottom-up approach to understand and engineer life

A complementary strategy to top-down approaches is using bottom-up approaches, which aim to engineer simpler biological systems from a minimal set of well-

characterized parts. Bottom-up approaches came into use in the 1940s, when scientists found that they could prepare *in vitro* systems known as "extracts" or "lysates" by extracting the contents of living cells after growing the cells and performing cell lysis [5]. These cell-free systems — prepared from diverse cell types including bacteria, wheat germ, and rabbit reticulocytes — contained functional cellular machinery of the cytosol. Although these cell-free systems still contained thousands of different proteins and were not fully characterized systems, the near-elimination of cell membrane processes as well as the elimination of cell growth and division greatly reduced the complexity of these cell-like systems, and thus they allowed scientists to probe living processes in an open and more controlled reaction environment [5]. Among various other discoveries, cell-free systems led scientists to discover the relationship between nucleotide triplets and their corresponding amino acids, to learn that protein synthesis requires ATP and GTP, to understand gene regulation, and to establish "the central dogma" [5].

While in continuous use for the past several decades, cell-free systems became more widespread in the early 2000s as a tool of synthetic biology. Cell-free synthetic biology is a growing field aimed at engineering biological parts and systems in a cell-free context, as opposed to *in vivo* (i.e., engineering living cells and organisms) [6]. Beyond greater control over the reaction environment, the cell-free approach offers many advantages over engineering cellular systems, including the ability to produce toxic small molecules or proteins that are difficult to express in living cells and scalability for biomanufacturing and other applications. Many cell-free applications rely on cell-free protein synthesis, where crude cell lysate or purified proteins are supplemented with DNA and an energy buffer containing small molecules that enable *in vitro* transcription and translation (TX-TL) [7–9].

In recent years, cell-free applications have expanded to include protein engineering [6, 10], metabolic engineering [11–14], high-throughput prototyping of engineered biological components and systems [15–17], biosensing and diagnostics [18–20], studying the synthesis and assembly of complex biological structures such as membrane proteins and bacteriophages [21–25], and biomanufacturing [26]. During this time, cell-free synthetic biology — as well as synthetic biology more broadly — has enabled efforts not just to understand life under through the lens of molecular biology but also to engineer biology for novel applications in healthcare, biotechnology, and sustainability [26].

1.3 Synthetic cells: towards a minimal, autonomous life form

As the capabilities of cell-free synthetic biology have grown, researchers have used it as a platform for a new approach to understand and engineer life: building synthetic biological cells. Beyond engineering biomolecular components and systems, would it be possible to (1) combine these modules and capabilities and (2) encapsulate them in a contained environment to create a synthetic biological cell? Using top-down biological approaches has been helpful in validating the functions of biological components, pathways, and modules, but these approaches make it difficult to disentangle the effects of interacting or coupled components in cells. However, building a cell using a bottom-up approach — i.e., assembling a synthetic cell from individual components — would enable researchers to fully understand the contribution and function of each component in a way that is not possible with previous approaches.

Although a fully autonomous synthetic cell has not yet been realized, the past few decades have seen rapid development of the capabilities that will ultimately be necessary to build a cell [27–29]. While varying in their definition, form, and function, synthetic cells typically consist of a biomolecular program encapsulated by a biomimetic boundary. A variety of biomolecular programs have been reconstituted to date, ranging from DNA strand displacement programs in a suitable aqueous solution to genetic circuits enabled by cell-free protein synthesis systems. Compartmentalization has also been achieved successfully, through the use of materials including lipids (to make liposomes), polymers (to make polymersomes), and protein capsids [29].

Inspired by living cells, researchers have functionalized many components and systems of living cells in synthetic cells. These modules include TX-TL, membrane proteins, organelles, cell-cell communication, metabolism, lipid biosynthesis, DNA replication, motility, energy regeneration, and cell division [29, 30]. Although research labs across the globe typically work on different components and subsystems of synthetic cells, recent years have seen the development and growth of many collaborative synthetic cell communities — including Build-a-Cell (global), fabriCELL (United Kingdom), MaxSynBio (Max Planck Institute, Germany), BaSyC (Netherlands), SynCellEU (European Union), SynCell Asia, and SynCell Africa — that are actively working towards combining different modules towards the goal of achieving a fully autonomous synthetic cell.

As the field of synthetic cells has grown, researchers' goals have also expanded

beyond their primary focus on building cells to understand life. The field has also focused on engineering synthetic cells for applications in nanomedicine and environmental monitoring [31, 32]. Another growing aim of the field is to focus not on life as we know it, but life as it can be; this is especially relevant in the field of astrobiology, where researchers are working to reproduce environmental conditions of distant astronomical bodies in the lab to study if and how "protocells" may thrive in places like Mars and Europa [33, 34].

1.4 Challenges and opportunities in engineering synthetic cells

Despite rapid progress in the field, many critical roadblocks remain in the path to building a fully autonomous synthetic cell. Below, I highlight four major categories that capture many of these challenges.

Subsystem integration

In the past few years, there have been relatively few efforts aimed at integrating synthetic cell subsystems. Some examples include integrating DNA replication with TX-TL and with membrane biosynthesis [35, 36]. Other efforts include integrating different membrane proteins to reconstitute energy regeneration pathways [30, 37]. However, most labs in the field of synthetic cell research have focused on individual modules for the synthetic cell, such as cell division, metabolism, and TX-TL. While this approach allows labs to build tools, techniques, and expertise and to excel in a particular research area, it poses a challenge for efforts aimed at combining different modules together. Improvements in protocol writing have reduced the barrier to addressing this issue, but gaining the expertise to perform tasks as diverse as purifying membrane proteins, using microfluidics to generate liposomes, and preparing cell-free protein synthesis systems reproducibly is not trivial for a graduate student or even a lab.

Beyond the issue of research expertise, which can be overcome with more technical training and improved protocols, bioengineering has unique challenges compared to other engineering disciplines. Biological components and systems used for building cells are derived from living cells and organisms, which have evolved to perform as many functions as necessary to survive with as little biomass as possible. As a consequence, these components and systems have both redundancy (where multiple components and systems can perform the same task, often synergistically) and extreme versatility (where a single component or system can perform multiple functions). While these properties serve living organisms well, they pose challenges

for researchers who wish to understand and predict the function of each subsystem, let alone integrated systems consisting of many different subsystems.

Thus, as researchers begin integrating different synthetic cell subsystems together, they will have to answer many questions. Are these subsystems compatible, especially if parts are derived from different organisms? Are these subsystems coupled through the use of a shared resource, such as energy carriers like adenosine triphosphate (ATP), and does that pose a challenge for system performance? Given that we don't fully understand how living cells work, how might we learn which additional parts are necessary and sufficient to integrate multiple subsystems?

Reproducibility

A lack of reproducible research is a challenge in synthetic cell research and stems primarily from two sources. First, as with many other fields of research, insufficiently detailed protocols and restrictions on sharing materials can hinder efforts to reproduce a different lab's work, which is essential for synthetic cell subsystem integration (see **Subsystem integration** above).

The second source of irreproducibility arises from user-introduced variability in the preparation of biological parts and systems. For example, the composition and concentrations of proteins in cell lysates can vary among batches of lysate due to indiscernible differences in their preparation, including the growth stage at which cells are harvested for lysis, variations in instrument usage for cell lysis, and the quality of chemicals used for lysate preparation and processing. As another example, components such as proteins, DNA, or small molecules that are purified from cells or purchased commercially can similarly have variability, albeit arising from user-introduced variations such as DNA plasmid design, purification quality control, or instability resulting from long-term freezer storage.

When cell lysate or other additives are then used as components of cell-free protein synthesis systems to drive biomolecular programs inside synthetic cells, this variability is propagated to the performance of synthetic cells. For example, these synthetic cells may not be able to make enough protein for researchers to observe a phenotype, such as the expression of a fluorescent molecule or morphological changes in the synthetic cell. In other cases, for synthetic cells containing multiple subsystems, variability in each subsystem may push the fully integrated system into an experimental regime it is unable to operate in.

Predictability

Related to the previous two problem areas, limited characterization of biological components and systems has inhibited researchers' ability to predict the performance of synthetic cells. Most synthetic cell research thus far has focused on proof-of-concept experiments that demonstrate the functionality of individual components and subsystems in synthetic cells, mitigating a need for prediction. However, as researchers begin to engineer more complex synthetic cells with multiple subsystems (see **Subsystem integration** above), prediction will be necessary to help inform design considerations of the individual modules and to determine if the fully integrated system meets desired performance standards.

Mathematical models of synthetic cells have focused primarily on predicting cell-free protein synthesis, which is the most common type of biomolecular program encapsulated inside synthetic cells. Varying in complexity, these models have incorporated some important processes of protein synthesis, such as utilization of nucleotide triphosphates (NTPs) and amino acids by transcription and translation [38–43]. Validating these models outside of their original experimental context, however, has remained a challenge due to difficulties in reproducing or adapting computational workflows.

New functionalities

As mentioned previously, researchers have worked on various modules for synthetic cells, from metabolism to energy regeneration to cell division. However, most efforts have focused on protein synthesis of single proteins within the synthetic cell or encapsulation of simple purified components within the synthetic cell. Examples of these efforts include construction of a synthetic mechanosensitive signaling pathway in compartmentalized artificial cells [44], genetically encoded tissue formation by expression of pore-forming proteins in synthetic cells [45], and expression and assembly of bacterial microtubules for shaping synthetic cells [46].

More recently, advanced capabilities are beginning to be implemented in synthetic cells. These efforts include work towards a genetically encoded divisome [47], an energy regeneration pathway [37], and motility [48] in synthetic cells. However, these capabilities (1) have not been fully realized, (2) are incompatible with other modules in their current implementation, or (3) are not fully autonomous as they would be in a living cell. For example, current efforts have been successful in reconstituting and aligning an FtsZ division ring in synthetic cells, but division,

contraction, and complete scission has not yet been fully realized in synthetic cells. Meanwhile, efforts to create energy regeneration pathways in synthetic cell membranes often rely on purification and reconstitution of membrane proteins in liposomes using a process that is incompatible with encapsulation of a cell-free protein synthesis system. Existing efforts to reconstitute synthetic cell motility currently require external modulation or are incompatible with control mechanisms. Thus, as researchers work to expand the capabilities of synthetic cells, there are many opportunities for expanding the functionalities for synthetic cells while ensuring that these functionalities are compatible with other synthetic cell modules.

1.5 Outline of thesis chapters

In this thesis, I describe my efforts to address some of the aforementioned challenges in engineering synthetic cells.

In Chapter 2, I focus on irreproducibility in synthetic cells by investigating sources of variability in *in vitro* transcription-translation (TX-TL) systems, a widely used platform to implement biomolecular programs in synthetic cells. Our results show clear roles for how magnesium (Mg^{2+}), fuel, cell lysate preparation, and other TX-TL reaction components separately affect transcription and translation and give rise to TX-TL variability. We also show a high-level trend that TX-TL performance is broadly constrained by energy availability, and that the performance space can be traversed predictably by varying the concentrations of these TX-TL reaction components.

In Chapter 3, I focus on improving predictability of synthetic cell performance, by exploring whether an existing model of TX-TL coupled to cell-free metabolism can be adapted outside its original experimental context. Using Bayesian parameter inference, we show that it is relatively straightforward and remarkably powerful to take the existing model and adapt it to new contexts by modifying just a few model parameters. We first show that the model architecture is sufficient to capture a broad range of protein expression dynamics, after which we demonstrate that the model can both be predictive and provide experimental insights into variability among TX-TL systems.

In Chapter 4, I focus on new functionalities and subsystem integration and show preliminary efforts towards the construction of an ATP synthase-based "proto-flagellum." In designing a mechanism for autonomous, programmable motility, we simultaneously attempt to create a proof-of-concept for integrating an energy

regeneration subsystem with a motility subsystem. We show that these initial efforts contain some experimental successes, and we highlight promising next steps towards achieving a “self-driving” synthetic cell.

References

[1] Ga Hyun Lee et al. "Biotechnological plastic degradation and valorization using systems metabolic engineering." In: *International journal of molecular sciences* 24.20 (2023), p. 15181. DOI: 10.3390/ijms242015181.

[2] Georg Schett et al. "Advancements and challenges in CAR T cell therapy in autoimmune diseases." In: *Nature Reviews Rheumatology* 20.9 (2024), pp. 531–544. DOI: 10.1038/s41584-024-01139-z.

[3] Carin J Ragland, Kevin Y Shih, and José R Dinneny. "Choreographing root architecture and rhizosphere interactions through synthetic biology." In: *Nature Communications* 15.1 (2024), p. 1370. DOI: 10.1038/s41467-024-45272-5.

[4] Christine Ho and Leonardo Morsut. "Novel synthetic biology approaches for developmental systems." In: *Stem Cell Reports* 16.5 (2021), pp. 1051–1064. DOI: 10.1016/j.stemcr.2021.04.007.

[5] Shaorong Chong. "Overview of cell-free protein synthesis: historic landmarks, commercial systems, and expanding applications." In: *Current Protocols in Molecular Biology* 108.1 (2014), pp. 16.30.1–16.30.11. DOI: 10.1002/0471142727.mb1630s108.

[6] David Garenne et al. "Cell-free gene expression." In: *Nature Reviews Methods Primers* 1.1 (2021), p. 49. ISSN: 2662-8449. DOI: 10.1038/s43586-021-00046-x.

[7] Yoshihiro Shimizu et al. "Cell-free translation reconstituted with purified components." In: *Nature Biotechnology* 19.8 (2001), pp. 751–755. ISSN: 1546-1696. DOI: 10.1038/90802.

[8] Zachary Z Sun et al. "Protocols for implementing an Escherichia coli based TX-TL cell-free expression system for synthetic biology." In: *Journal of Visualized Experiments: JoVE* 79 (2013). DOI: 10.3791/50762.

[9] Nicole E. Gregorio, Max Z. Levine, and Javin P. Oza. "A user's guide to cell-free protein synthesis." eng. In: *Methods and Protocols* 2.1 (2019). ISSN: 2409-9279. DOI: 10.3390/mps2010024.

[10] August Brookwell, Javin P. Oza, and Filippo Caschera. "Biotechnology applications of cell-dree expression systems." In: *Life* 11.12 (2021). ISSN: 2075-1729. DOI: 10.3390/life11121367.

[11] Ashty S. Karim and Michael C. Jewett. "A cell-free framework for rapid biosynthetic pathway prototyping and enzyme discovery." In: *Metabolic Engineering* 36 (2016), pp. 116–126. ISSN: 1096-7176. DOI: 10.1016/j.ymben.2016.03.002.

[12] Ashty S. Karim et al. “In vitro prototyping and rapid optimization of biosynthetic enzymes for cell design.” In: *Nature Chemical Biology* 16.8 (2020), pp. 912–919. ISSN: 1552-4469. DOI: 10.1038/s41589-020-0559-0.

[13] Xiunan Yi et al. “Establishing a versatile toolkit of flux enhanced strains and cell extracts for pathway prototyping.” In: *Metabolic Engineering* 80 (2023), pp. 241–253. ISSN: 1096-7176. DOI: 10.1016/j.ymben.2023.10.008.

[14] Bastian Vögeli et al. “Cell-free prototyping enables implementation of optimized reverse beta-oxidation pathways in heterotrophic and autotrophic bacteria.” In: *Nature Communications* 13.1 (2022), p. 3058. ISSN: 2041-1723. DOI: 10.1038/s41467-022-30571-6.

[15] Richard Kelwick et al. “Development of a *Bacillus subtilis* cell-free transcription-translation system for prototyping regulatory elements.” In: *Metabolic Engineering* 38 (2016), pp. 370–381. ISSN: 1096-7176. DOI: 10.1016/j.ymben.2016.09.008.

[16] Melissa K. Takahashi et al. “Characterizing and prototyping genetic networks with cell-free transcription–translation reactions.” In: *Bacterial and Archaeal Transcription* 86 (2015), pp. 60–72. ISSN: 1046-2023. DOI: 10.1016/j.ymeth.2015.05.020.

[17] Zoe Swank and Sebastian J. Maerkl. “CFPU: a cell-free processing unit for high-throughput, automated in vitro circuit characterization in steady-state conditions.” In: *BioDesign Research* 2021 (2021), p. 2968181. ISSN: null. DOI: 10.34133/2021/2968181.

[18] Caitlin E. Sharpes et al. “Assessment of colorimetric reporter enzymes in the PURE System.” In: *ACS Synthetic Biology* 10.11 (2021), pp. 3205–3208. DOI: 10.1021/acssynbio.1c00360.

[19] Yan Zhang et al. “Point-of-care analyte quantification and digital readout via lysate-based cell-free biosensors interfaced with personal glucose monitors.” In: *ACS Synthetic Biology* 10.11 (2021), pp. 2862–2869. DOI: 10.1021/acssynbio.1c00282.

[20] Peter Q. Nguyen et al. “Wearable materials with embedded synthetic biology sensors for biomolecule detection.” In: *Nature Biotechnology* 39.11 (2021), pp. 1366–1374. ISSN: 1546-1696. DOI: 10.1038/s41587-021-00950-3.

[21] Jonghyeon Shin, Paul Jardine, and Vincent Noireaux. “Genome replication, synthesis, and assembly of the bacteriophage T7 in a single cell-free reaction.” In: *ACS Synthetic Biology* 1.9 (2012), pp. 408–413. DOI: 10.1021/sb300049p.

[22] Erik Henrich et al. “Membrane protein production in *Escherichia coli* cell-free lysates.” In: *FEBS Letters* 589.15 (2015), pp. 1713–1722. ISSN: 0014-5793. DOI: 10.1016/j.febslet.2015.04.045.

[23] Lena Thoring et al. “High-yield production of “difficult-to-express” proteins in a continuous exchange cell-free system based on CHO cell lysates.” In: *Scientific Reports* 7.1 (2017), p. 11710. ISSN: 2045-2322. DOI: 10.1038/s41598-017-12188-8.

[24] Pawel Leznicki et al. “Co-translational biogenesis of lipid droplet integral membrane proteins.” In: *Journal of Cell Science* 135.5 (2021), jcs259220. ISSN: 0021-9533. DOI: 10.1242/jcs.259220.

[25] Yutaro Yamaoka et al. “Characterization and utilization of disulfide-bonded SARS-CoV-2 receptor binding domain of spike protein synthesized by wheat germ cell-free production system.” In: *Viruses* 14.7 (2022). ISSN: 1999-4915. DOI: 10.3390/v14071461.

[26] David Garenne et al. “Cell-free gene expression.” In: *Nature Reviews Methods Primers* 1.1 (2021), p. 49. ISSN: 2662-8449. DOI: 10.1038/s43586-021-00046-x.

[27] Eunhee Cho and Yuan Lu. “Compartmentalizing cell-free systems: toward creating life-like artificial cells and beyond.” In: *ACS Synthetic Biology* 9.11 (2020), pp. 2881–2901. DOI: 10.1021/acssynbio.0c00433.

[28] N. Amy Yewdall, Alexander F. Mason, and Jan C. M. van Hest. “The hallmarks of living systems: towards creating artificial cells.” In: *Interface Focus* 8.5 (2018), p. 20180023. DOI: 10.1098/rsfs.2018.0023.

[29] Lynn J. Rothschild et al. “Building synthetic cells - from the technology infrastructure to cellular entities.” In: *ACS Synthetic Biology* (2024). DOI: 10.1021/acssynbio.3c00724.

[30] Sungwoo Jeong et al. “Toward artificial cells: novel advances in energy conversion and cellular motility.” In: *Advanced Functional Materials* 30.11 (2020). _eprint: https://onlinelibrary.wiley.com/doi/pdf/10.1002/adfm.201907182, p. 1907182. DOI: https://doi.org/10.1002/adfm.201907182. URL: https://onlinelibrary.wiley.com/doi/abs/10.1002/adfm.201907182.

[31] Sibel Emir Diltemiz et al. “Use of artificial cells as drug carriers”. In: *Materials Chemistry Frontiers* 5.18 (2021), pp. 6672–6692.

[32] Corina L. Logigan, Cristian Peptu, and Catalina A. Peptu. “Chapter 17 - Liposomes for delivery of substances for other (non-therapeutic) applications”. In: *Liposomes in Drug Delivery*. Ed. by Sophia G. Antimisiaris. Academic Press, 2024, pp. 435–460. ISBN: 978-0-443-15491-1. DOI: 10.1016/B978-0-443-15491-1.00014-6.

[33] David Deamer. “Perspective: Protocells and the Path to Minimal Life”. In: *Journal of Molecular Evolution* 92.5 (2024), pp. 530–538.

[34] Lynn Rothschild. “How the" Build a Cell" Effort Can Aid Astrobiology”. In: *The Astrobiology Science Conference (AbSciCon) 2024*. 4. 2024, pp. 218–04.

[35] Zhanar Abil et al. “Darwinian evolution of self-replicating DNA in a synthetic protocell”. In: *Nature Communications* 15.1 (2024), p. 9091.

[36] Ana María Restrepo Sierra et al. “A synthetic cell with integrated DNA self-replication and membrane biosynthesis”. In: *bioRxiv* (2025). DOI: 10.1101/2025.01.14.632951. eprint: https://www.biorxiv.org/content/early/2025/01/14/2025.01.14.632951.full.pdf.

[37] Sabina Deutschmann et al. “Modulating Liposome Surface Charge for Maximized ATP Regeneration in Synthetic Nanovesicles”. In: *ACS Synthetic Biology* 13.12 (2024), pp. 4061–4073.

[38] Michael Vilkhovoy et al. “Sequence specific modeling of *E. coli* cell-free protein synthesis.” In: *ACS Synthetic Biology* 7.8 (2018). Publisher: American Chemical Society, pp. 1844–1857. DOI: 10.1021/acssynbio.7b00465.

[39] Nicholas Horvath et al. “Toward a genome scale sequence specific dynamic model of cell-free protein synthesis in *Escherichia coli*.” In: *Metabolic Engineering Communications* 10 (2020), e00113. ISSN: 2214-0301. DOI: 10.1016/j.mec.2019.e00113.

[40] Grace E. Vezeau and Howard M. Salis. “Tuning cell-free composition controls the time delay, dynamics, and productivity of TX-TL expression.” In: *ACS Synthetic Biology* 10.10 (2021), pp. 2508–2519. DOI: 10.1021/acssynbio.1c00136.

[41] Zoila Jurado, Ayush Pandey, and Richard M. Murray. “A chemical reaction network model of PURE”. In: *bioRxiv* (2023). DOI: 10.1101/2023.08.14.553301. eprint: https://www.biorxiv.org/content/early/2023/08/14/2023.08.14.553301.full.pdf.

[42] Ayush Pandey et al. “Characterization of Integrase and Excisionase Activity in a Cell-Free Protein Expression System Using a Modeling and Analysis Pipeline”. In: *ACS Synthetic Biology* 12.2 (2023), pp. 511–523. DOI: 10.1021/acssynbio.2c00534.

[43] Jan Müller, Martin Siemann-Herzberg, and Ralf Takors. “Modeling cell-free protein synthesis systems-approaches and applications.” eng. In: *Frontiers in bioengineering and biotechnology* 8 (2020), p. 584178. ISSN: 2296-4185. DOI: 10.3389/fbioe.2020.584178.

[44] James W. Hindley et al. “Building a synthetic mechanosensitive signaling pathway in compartmentalized artificial cells”. In: *Proceedings of the National Academy of Sciences* 116.34 (2019), pp. 16711–16716. DOI: 10.1073/pnas.1903500116.

[45] Alexander Harjung, Alessandro Fracassi, and Neal K Devaraj. “Encoding extracellular modification of artificial cell membranes using engineered self-translocating proteins”. In: *Nature Communications* 15.1 (2024), p. 9363.

[46] Johannes Kattan et al. “Shaping liposomes by cell-free expressed bacterial microtubules”. In: *ACS Synthetic Biology* 10.10 (2021), pp. 2447–2455.

[47] Shunshi Kohyama, Adrián Merino-Salomón, and Petra Schwille. “In vitro assembly, positioning and contraction of a division ring in minimal cells”. In: *Nature Communications* 13.1 (2022), p. 6098.

[48] Désirée Sauter et al. “Artificial cytoskeleton assembly for synthetic cell motility”. In: *Macromolecular Bioscience* 23.8 (2023), p. 2200437.

Chapter 2

METABOLIC PERTURBATIONS TO AN *ESCHERICHIA COLI*-BASED CELL-FREE SYSTEM REVEAL A TRADE-OFF BETWEEN TRANSCRIPTION AND TRANSLATION

This chapter has been published in the journal article indicated below and reprinted with permission. It has been reformatted and included here with minor edits.

Manisha Kapasiawala and Richard M. Murray. "Metabolic perturbations to an Escherichia coli-based cell-free system reveal a trade-off between transcription and translation." In: *ACS Synthetic Biology* 13.12 (2024), pp. 3976–3990. DOI: 10.1021/acssynbio.4c00361.

2.1 Introduction

Cell-free synthetic biology is a rapidly growing field that leverages synthetic biology tools and techniques to engineer biological systems outside the traditional context of living cells [1]. The cell-free approach offers many advantages over engineering cellular systems, including greater control over the reaction environment, the ability to produce toxic small molecules or proteins that are difficult to express in living cells, and scalability for biomanufacturing and other applications. In recent years, cell-free systems have been used for protein engineering [1, 2], rapid and high-throughput prototyping of engineered biological components and systems [3–7], biosensing and diagnostics [8–10] and the development of synthetic life [11–13].

Most cell-free applications rely on cell-free protein synthesis, where crude cell lysate or purified proteins are supplemented with DNA and an energy buffer containing small molecules that enable *in vitro* transcription and translation (TX-TL) [14–16]. Although cell lysate-based TX-TL systems have many uses, their performance and scope are limited by issues such as batch-to-batch variability [17], lack of predictability [18], and limited lifetime [19]. These issues arise because cell lysate's proteomic composition largely reflects the cytosolic protein content of living cells. While some of these proteins are harnessed to regenerate energy molecules for TX-TL processes, most of them generate metabolites that are benign or even harmful for TX-TL.

To address these concerns, previous studies have sought to gain insight into TX-TL dynamics through a variety of experimental approaches. Most of these studies have focused on gaining detailed insight into how perturbations to TX-TL reaction conditions - including salts [20, 21], fuel sources [22, 23], crowding agents [20, 24], and other components [15, 19, 25–28] - affect TX-TL performance. Some studies have taken a less targeted approach, with the authors opting instead to harness lab automation and machine learning along with experiments to rapidly optimize TX-TL systems [27, 29]. While these studies have helped elucidate which reaction components and preparation steps affect TX-TL performance and predictability most significantly, more work is necessary to determine why these factors contribute to variability and limited TX-TL lifetime as well as the broader implications they have for design principles for TX-TL systems.

Aiming to get a more holistic view of cell-free reaction dynamics, more recent studies have focused on measuring small molecules - including NTPs, amino acids, and central carbon metabolites - that participate in cell-free metabolism and studying or modeling their effects on TX-TL [30–33]. In one such study, the authors found that the majority of *E. coli* metabolic pathways are active during TX-TL [33], and they subsequently used these insights to form a phenomenological model of TX-TL coupled to cell-free metabolism, with the model containing "fuel," "energy," and "waste" species and their effects on TX-TL. By linking cell-free metabolism's effects on TX-TL dynamics to specific TX-TL reaction components, these studies have suggested that further insight into TX-TL predictability, variability, and lifetime could come from further investigation of the effects of metabolism on TX-TL.

Building off the experiments and insights from these previous studies, to understand the effect of cell-free metabolism on TX-TL variability, we focused our efforts on the chemical composition of the buffer that is used with cell lysate and DNA to form a TX-TL reaction. We targeted two classes of small molecules to modulate: "energy" molecules, specifically nucleotide triphosphates (NTPs), which power TX-TL processes, and "fuel" molecules, which regenerate NTPs via cell lysate metabolism. We also considered the effects of magnesium (Mg^{2+}), both because of its biological importance - in stabilizing nucleic acids and ribosomes, acting as an essential cofactor for many enzymes, and making ATP bioactive in the form of Mg-ATP - and because of several previous findings suggesting its role in modulating TX-TL dynamics [21, 24, 25, 28].

Using malachite green mRNA aptamer (MG aptamer) and destabilized enhanced

green fluorescent protein (deGFP) as transcriptional and translational readouts, respectively, we report the presence of a trade-off between optimizing total protein yield and optimizing total mRNA yield, as measured by integrating the area under the curve for mRNA time-course dynamics. We found that the trade-off is present across different fuel sources, that a system's position along the trade-off curve is determined strongly by Mg^{2+} concentration and fuel type, and that the trade-off curve's location shifts and range becomes larger as DNA concentration is increased. In systems where transcription and translation were decoupled, we found that a distinct regime optimized for translation exists in the translation-only system, but no distinct regime was optimized for transcription in the transcription-only system, suggesting that the trade-off arises at the translational level. Finally, in systems where additional energy is supplied and a fuel source is absent, the trade-off is absent. Overall, our results suggest that the trade-off arises from limitations in translation regulation and inefficient energy regeneration. By improving our understanding of the effects of fuel and energy metabolism on TX-TL in cell-free systems, this work provides insight into design considerations for future studies aimed at improving TX-TL performance, lifetime, standardization, and prediction.

2.2 Results

E. coli Rosetta2 cell-free systems exhibit a trade-off between transcription and translation across fuel sources and concentrations

As most previous studies have utilized either a design of experiments approach (e.g., randomly surveying many reaction compositions) or modulated components one at a time, we chose to simultaneously vary the fuel and Mg^{2+} concentrations. We performed TX-TL reactions consisting of fuel versus Mg^{2+} panels, where the former was varied between 0 and 45 mM, the latter was simultaneously varied between 0 and 10 mM, and all other reaction components were kept the same [14] (see Materials and Methods for more details) (Figure 2.1a). As the preparation of cell lysate varies significantly from lab to lab and is difficult to keep consistent [18], we performed experiments in two cell lysate preparations - prepared by different lab members and using different lysis methods, among other differences to see if these chemical factors acted consistently.

For fuel molecules, we focused on four fuel metabolites with varying degrees of energy regeneration and waste generation capacity that spanned central carbon metabolism to gain insight into how different fuel molecules affect TX-TL through their effect on metabolism. We chose four central carbon metabolites: 3-

phosphoglyceric acid (3PGA), maltose, pyruvate, and succinate (Figure 2.1b). We targeted 3PGA - whose conversion to pyruvate regenerates ATP during glycolysis - because it is one of the standard molecules [14] used for energy regeneration in cell lysate-based TX-TL systems (the others being phosphoenolpyruvate (PEP) and pyruvate). We chose pyruvate because it is located downstream of 3PGA in the glycolysis pathway and can also participate in energy regeneration, albeit without contributing potential waste molecule inorganic phosphate (P_i) to the system [21]. We selected maltose, which consumes P_i and outputs a glucose molecule and glucose-6-phosphate (G6P) molecule, because it has been used previously to improve energy regeneration by recycling P_i [34]. However, as one maltose molecule can be used to generate two G6P molecules and thus four 3PGA molecules, maltose produces more candidate waste molecules per molecule of fuel compared to the other three fuels. These candidate waste molecules include acetate, ethanol, lactate, and formate (and their conjugate organic acids), which may inhibit TX-TL either directly or indirectly by reducing pH too low for optimal enzyme activity [35–37]. Finally, we considered succinate, whose conversion from succinyl-CoA regenerates GTP. As the succinyl-CoA to succinate reaction is reversible, we believed that the addition of succinate could slow down GTP regeneration by favoring the reverse reaction, thereby reducing the overall rate of energy regeneration to a level where energy could be used more efficiently by TX-TL. TX-TL reactions were supplied with one of two different preparations of cell lysate along with plasmid DNA encoding the sequence for the expression of MG aptamer, which fluoresces upon binding to malachite green (MG) dye, and deGFP, under a P_{OR1OR2} promoter. For each reaction condition, the total integrated area under MG aptamer fluorescence curve and maximum deGFP were calculated as measurements of transcription and translation, respectively. The results of these experiments are shown in Figure 2.1.

By plotting maximum deGFP versus integrated MG aptamer for all fuel sources across different fuel and Mg^{2+} concentrations, we observed a trade-off between optimizing maximum deGFP and optimizing integrated MG aptamer (Figure 2.1c, d). The same trade-off curve was observed across all fuel sources, and points corresponding to systems with no added fuel also fell along the same curve (Figure 2.1c). Furthermore, when all fuels are treated equally, a system's position along the trade-off curve was mostly unaffected by the concentration of fuel (Figure 2.1d, bootstrapped Spearman's rho correlation of 0.22 ± 0.05). Control experiments indicated that the fluorescence of deGFP was robust across different 3PGA and Mg^{2+} concentrations used in these experiments and that MG aptamer fluorescence

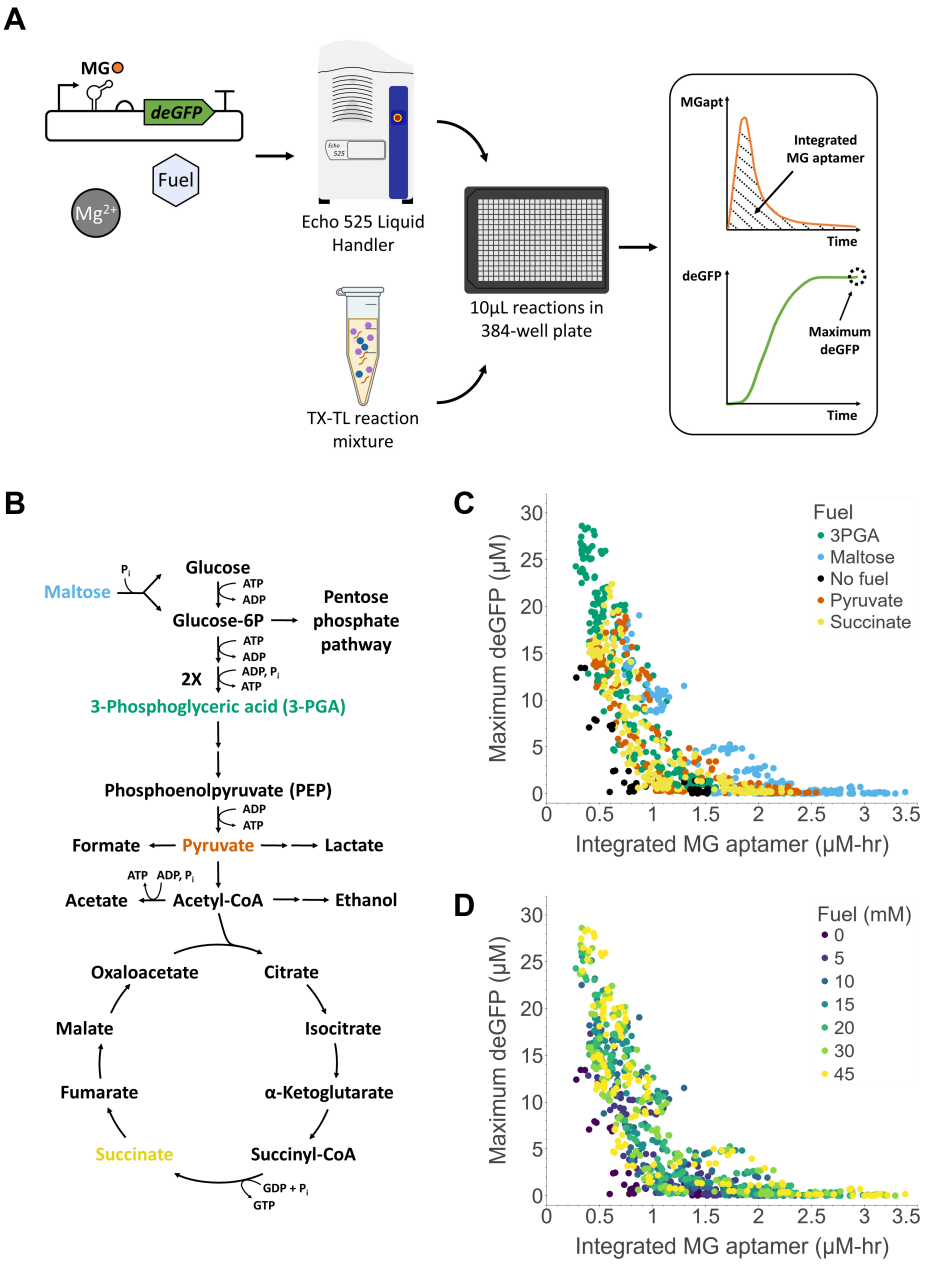

Figure 2.1: TX-TL trade-off across fuel sources and concentrations. (a) Overview of experimental workflow. (b) Simplified map of *E. coli* core metabolism with NTP consumption and regeneration. A simplified glycolysis, TCA cycle, and interacting branch of the Pentose Phosphate Pathway are shown. Consumption or regeneration of other cofactors - such as NADH, FADH, QH2, H_2O, and CO_2 - is omitted for simplicity. (c,d) Maximum deGFP values versus integrated MG aptamer values, colored by either (c) fuel type or (d) fuel concentration. Each point represents one of three replicates of a particular set of fuel and Mg^{2+} concentrations. The data shown reflect experiments performed in two preparations of cell lysate, Preparation 1 and Preparation 2 (see Materials and Methods for details), and all experiments were performed using 5 nM DNA.

was robust to changes in Mg^{2+} and pH (Figure S2.1a,c). While deGFP fluorescence was sensitive to pH, it was robust to Mg^{2+} in the relevant range of 0-10 mM and to pH across the estimated range of 6.5-7 [22, 23] (Figure S2.1b). As there was no observed trend of decreasing deGFP (or increasing MG aptamer) fluorescence with increasing fuel concentration, there did not appear to be a fuel concentration-dependent effect on fluorescence, including but not limited to pH. This suggested that expression of MG aptamer and deGFP, rather than their fluorescence alone, were changing across the various fuel and Mg^{2+} concentrations. Overall, these results suggest the presence of a trade-off between transcription and translation for the fuels considered here.

The results of this initial experiment were surprising because all points fell along the same trade-off curve, regardless of fuel type or lysate preparation. These results seem to suggest that while these TX-TL systems with different fuel types and concentrations exhibit variability in transcriptional and translational performance, their performance is constrained to a single trade-off curve that could be traversed for a given fuel type and desired performance.

Variability along the trade-off curve is controlled by Mg^{2+} concentration and lysate preparation

To investigate which factors controlled a system's position along the trade-off curve, we colored the data in Figure 1 by Mg^{2+} concentration and cell lysate preparation, as shown in Figure 2.2. We found that when considering all fuels equally, as the concentration of added Mg^{2+} increases, a TX-TL system generally shifts from a translation-optimized regime to a transcription-optimized regime (Figure 2.2a, bootstrapped Spearman's rho correlation of 0.63 ± 0.02). We also found that while data for the two preparations of lysate fell along the same curve, variability along the curve could be further explained by lysate preparation (Figure 2.2b).

As the Mg^{2+} trend is present across a variety of fuel sources (Figure S2.2), our results suggest that Mg^{2+} concentration can be tuned for a given set of cell lysate preparation, fuel type, and fuel concentration to reduce variability, improve predictability, or design TX-TL systems optimized for performance, including optimizing transcription, translation, or some combination of both. As Mg^{2+} is an essential cofactor for many proteins, these results also suggest that the TX-TL trade-off originates in part from Mg^{2+}-dependent regulation of TX-TL and/or metabolism machinery.

Inspecting Figure 2.2a more closely revealed that the Mg^{2+} trend was not completely

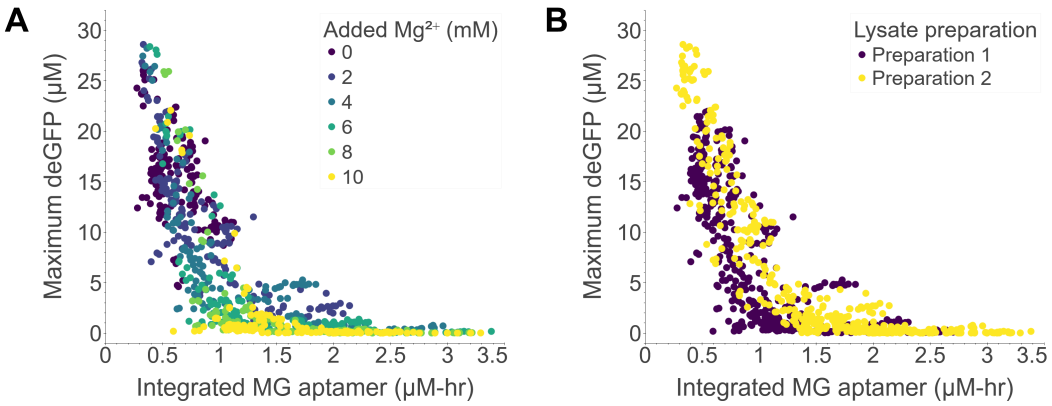

Figure 2.2: Effects of varying Mg^{2+} concentration and lysate preparation on the TX-TL trade-off. These panels show the same data from Figure 1C,D colored by the (a) concentration of added Mg^{2+} (in addition to the Mg^{2+} that is already in the cell lysate from its preparation in S30B buffer) or (b) lysate preparation. Each point represents one of three replicates of a particular set of fuel and Mg^{2+} concentrations. The data shown reflect experiments performed in two preparations of cell lysate, Preparation 1 and Preparation 2, in systems using 5 nM DNA.

consistent; plotting the trade-off separately for each fuel source revealed that a system's position along the trade-off curve was less correlated with Mg^{2+} in 3PGA-fueled systems than in systems using other fuels (Figure S2.2a, see figure caption for Spearman's rho correlation values). Specifically, while TX-TL systems fueled by pyruvate, succinate, and maltose were able to optimize translation at 0 mM added Mg^{2+} and optimize transcription at 10 mM added Mg^{2+}, some 3PGA-fueled systems were able to achieve high deGFP yields at high concentrations of added Mg^{2+}.

In 3PGA-fueled systems, increasing fuel pushes a system from a transcription-optimized to a translation-optimized regime

To understand why 3PGA-fueled systems deviated from the Mg^{2+} trend, we plotted the data from Figure 2.1d separately for each fuel type, as shown in Figure 2.3. While systems fueled by maltose, pyruvate, and succinate displayed a weak trend along the trade-off curve with increasing fuel concentration (Figure 2.3b-d, bootstrapped Spearman's rho correlations of 0.33 ± 0.09, 0.14 ± 0.07, and 0.27 ± 0.07, respectively), we found that in 3PGA-fueled systems, increasing fuel concentration was more strongly correlated with a system's position along the trade-off curve (Figure 2.3a, bootstrapped Spearman's rho correlations of 0.55 ± 0.05). Specifically, increasing 3PGA concentration generally shifted a TX-TL system from a transcription-optimized regime to a translation-optimized regime. This phenomenon was also

observed in 3PGA-fueled TX-TL systems where the volume fraction of cell lysate in a TX-TL reaction was increased or decreased by 25% (Figure S2.3), with the trend becoming stronger as the lysate fraction was increased (Figure S2.3d), thus extending the relevance of the trend to TX-TL systems using alternative cell lysate volume fractions [25].

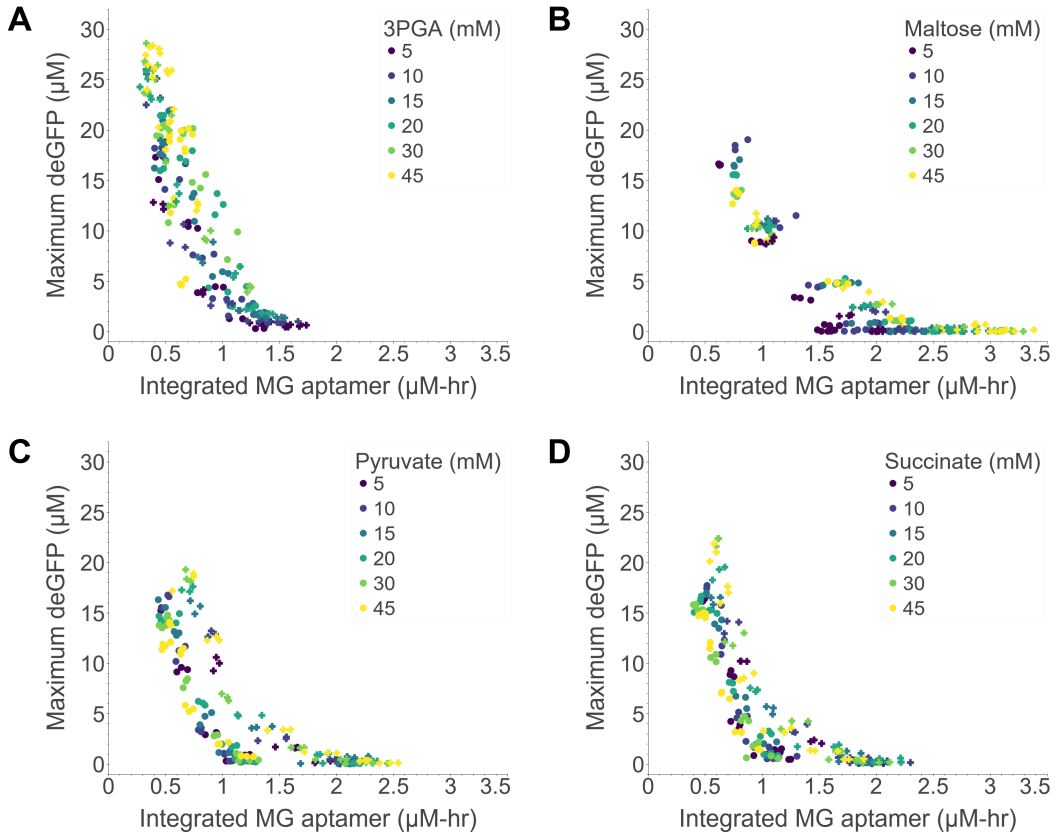

Figure 2.3: Effects of varying fuel concentration on the TX-TL trade-off by fuel type. The same data are shown as in Figure 2.1c,d with points colored by fuel concentration. Each point is one of three replicates of a set of fuel and Mg^{2+} concentrations, where fuel is either (a) 3PGA, (b) maltose, (c) pyruvate, or (d) succinate. Experiments were performed in two preparations of cell lysate, Preparation 1 (o) and Preparation 2 (+), in systems using 5 nM DNA.

We next sought to confirm whether the TX-TL trade-off and 3PGA trend extended to systems using different reporter plasmids. The results of these 3PGA versus Mg^{2+} panels are shown in Figure 2.4. We first switched the promoter from P_{OR1OR2} to P_{T7}, where we found that the TX-TL trade-off and 3PGA trend were present across P_{T7}-driven TX-TL systems (Figure 2.4b, bootstrapped Spearman's rho correlation of 0.58 ± 0.06), including in a system where the order of fluorophores was flipped (Figure S2.4), just as they were in P_{OR1OR2}-driven systems (Figure 2.4a, bootstrapped

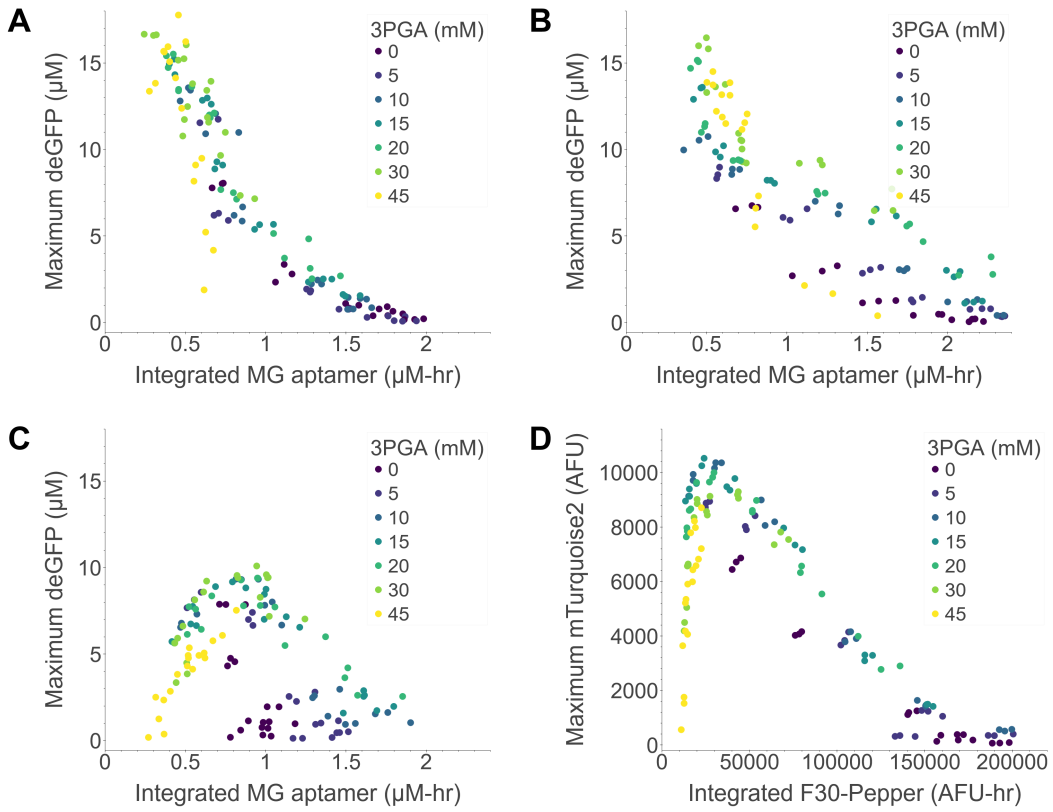

Figure 2.4: Effects of 3PGA concentration on the TX-TL trade-off across different reporter plasmids. Shown are trade-off curves corresponding to (a) P_{OR1OR2}-MG aptamer-deGFP, (b) P_{T7}-MG aptamer-deGFP, (c) P_{Tet}-MG aptamer-deGFP, and (d) P_{Tet}-F30 Pepper-mTurquoise2. P_{OR1OR2}, a strong promoter, and P_{Tet}, a medium strength promoter, are constitutive promoters, and P_{T7} is a strong non-*E. coli* promoter expressed in TX-TL reactions supplemented with 10 μM T7 RNA polymerase. Each point represents one of three replicates of a set of 3PGA and Mg^{2+} concentrations and is colored by 3PGA concentration. The data shown in (a-c) reflect experiments performed in cell lysate Preparation 3, while the data in (d) reflect experiments performed in cell lysate Preparation 2. All experiments were performed using 5 nM DNA.

Spearman's rho correlation of 0.69 ± 0.05). When the promoter was changed to P_{Tet}, however, the TX-TL trade-off curve was no longer visible, and the 3PGA trend was weaker (Figure 2.4c, bootstrapped Spearman's rho correlation of 0.44 ± 0.08). In P_{Tet}-driven TX-TL systems, it appeared that only some portion of the data, corresponding to about 15-30 mM 3PGA, fell along the common trade-off curve (Figure S2.5). The data corresponding to 0-5 mM 3PGA did not give the highest MG aptamer yields as in Figure 2.4a,b, and at high 3PGA concentrations, the left edge of the curve dipped, reflecting decreased deGFP yields at high 3PGA concentrations. To determine if this was a behavior unique to this promoter, we also performed a 3PGA versus Mg^{2+} panel in systems expressing the F30-Pepper aptamer and mTurquoise2 under a P_{Tet} promoter (Figure 2.4d). Here, the trade-off curve and 3PGA trend were present as before (bootstrapped Spearman's rho correlation of 0.51 ± 0.06), although as in systems using the P_{Tet}-MG aptamer-deGFP plasmid, there was a decrease in protein yields at higher 3PGA concentrations.

While it is not clear what caused this change in the shape of the trade-off curve in P_{Tet}-driven systems, this finding is consistent with the hypothesis that the TX-TL trade-off is indicative of a fundamental trade-off in fuel and energy metabolism. In such systems, weaker promoters would not be able to maximize rates of transcription and translation output as effectively, resulting in less deGFP being expressed before energy is dissipated by metabolic processes competing for the same energy pool and before translation-inhibiting waste is accumulated compared to TX-TL under strong promoters. This could explain why deGFP yields tend to drop at high 3PGA concentrations in Figure 2.4c,d, although this explanation is insufficient to explain the shape of the data in Figure 2.4c. While more promoters need to be tested to determine the generalizability of the TX-TL trade-off to systems using different genetic parts, the presence of the trade-off in P_{T7}-driven MG aptamer and deGFP expression was notable, considering that the P_{T7} promoter is widely used in applications aimed at maximizing protein expression.

In 3PGA-fueled systems, the TX-TL trade-off and fuel trend are consistent across DNA concentrations

Having confirmed that the TX-TL trade-off was present in a wide variety of TX-TL systems, we next sought to confirm whether the trade-off curve scaled with DNA concentration, as previous experiments had all been performed with 5 nM DNA. For this set of experiments, we decided to focus on 3PGA-fueled systems since 3PGA and its downstream metabolic product PEP are the most widely used metabolites

for energy regeneration in TX-TL systems, and gaining insight into the TX-TL trade-off in 3PGA-fueled systems would have greater relevance for studies aimed at characterizing and improving these systems.

We performed 3PGA panels versus Mg^{2+} panels at DNA concentrations of 1, 2.5, 5, 7.5, and 10 nM, and these results are shown in Figure 2.5. We found that the TX-TL trade-off curve's location shifted, and the range of MG aptamer and deGFP concentrations increased, as DNA concentration was increased, with a curve first becoming apparent at 2.5 nM DNA and then becoming more apparent as the DNA concentration was increased (Figure 2.5a).

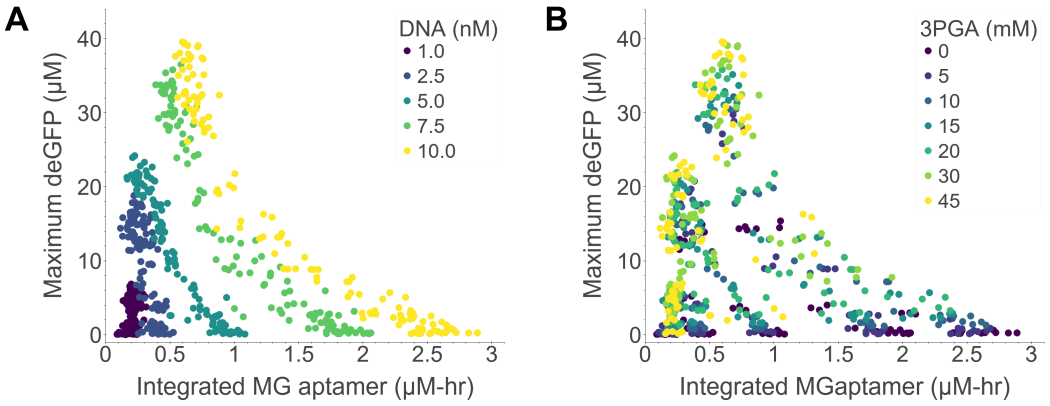

Figure 2.5: Effects of varying DNA concentration on the TX-TL trade-off. (a) Each point represents one of three replicates of a particular set of 3PGA and Mg^{2+} concentrations, where points are colored by DNA concentrations ranging from 1 to 10 nM. (b) Same data are shown as in (a), albeit with the points colored by 3PGA concentration rather than DNA concentration. The data shown reflect experiments performed in cell lysate Preparation 2 (see Materials and Methods for details).

As in the 5 nM DNA cases discussed in the previous section, the trend in shifting a system from a transcription-optimized regime to a translation-optimized regime at higher 3PGA concentrations was also consistent in the trade-off curves at DNA concentrations higher than 1 nM (Figure 2.5b, bootstrapped Spearman's rho correlations of 0.46 ± 0.08, 0.60 ± 0.07, 0.63 ± 0.06, 0.66 ± 0.06, and 0.69 ± 0.06 for DNA concentrations of 1, 2.5, 5, 7.5, and 10 nM, respectively). Preliminary analyses also revealed that transcription scaled linearly with increasing DNA concentration in systems along lines that intersected the trade-off curves (Figure S2.6). This finding is particularly relevant for transcription-only systems, where this linear relationship may make it easier to predict the performance of transcriptional circuits based on the concentrations of DNA species. More experiments are needed to determine

whether this linear transcriptional scaling is a general phenomenon in the TX-TL systems.

Trade-off arises at the translational level in 3PGA-fueled systems

Having confirmed that there was a TX-TL trade-off that controlled a system's transcriptional and translational capacity as a function of Mg^{2+} concentration broadly, and additionally as a function of 3PGA concentration when that fuel source was used, we next sought to gain more insight into the cause of the trade-off in 3PGA-fueled systems. It was not clear from our previous data whether conditions that optimized transcription versus conditions that optimized translation were mutually exclusive in that optimal Mg^{2+} and 3PGA concentrations were simply different for transcription versus translation. An alternative explanation was that either or both of the processes, transcription and translation, had an inhibitory effect on the other process; in the case where only one process inhibited the other, the first process could be inhibited by the reaction environment. A third possible explanation was that transcription and translation were processes competing for the same resources but that one process had a preferred regime for optimization. In this scenario, the energy-dominating process would have an optimal regime, and the other process would only be optimal where the energy-dominating process was strictly not optimal, thereby leaving more resources for the nondominating process. Combinations of these explanations, or others, could also explain the observed trade-off.

To gain insight into the individual processes of transcription and translation, we decoupled the TX-TL system into a transcription-only (TX-only) system and a translation-only (TL-only) system. In the TX-only system, tetracycline was added to the system to block translation via inhibition of translation initiation through its binding to the 30S subunit of the ribosome [38]. In the TL-only system, mRNA was added instead of DNA. The results of these experiments are shown in Figure 2.6.

Using heatmaps to display integrated mRNA and maximum deGFP data, we found that in the TX-TL system (Figure 2.6a), the regime of Mg^{2+} and 3PGA concentrations that optimized transcription was distinct and different than the regime that optimized translation (Figure 2.6d). Specifically, optimal transcription preferred low 3PGA and high Mg^{2+} concentrations, and optimal translation preferred high 3PGA and low Mg^{2+} concentrations; both findings are consistent with the trade-off curve. However, in the TX-only system (Figure 2.6b), MG aptamer expression was not optimized at low 3PGA and high Mg^{2+} as in the case of Figure 2.6d; rather, it was broadly optimal

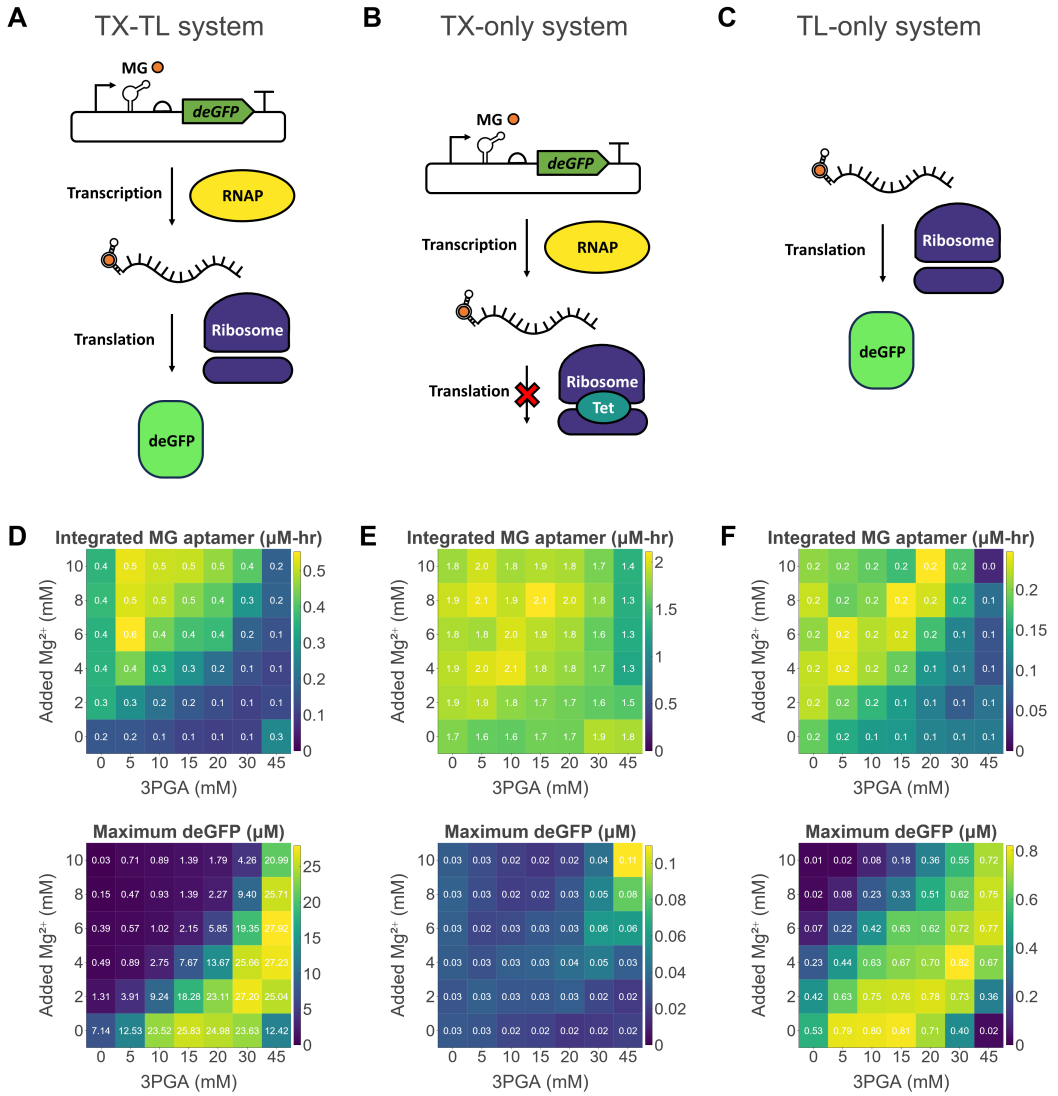

Figure 2.6: Decoupling of transcription (TX) and translation (TL). (a-c) Experimental schemes corresponding to the data shown in (d-f), respectively. (a) Simplified view of TX-TL: P_{OR1OR2}-MG aptamer-deGFP DNA is translated by *E. coli* RNA polymerase to mRNA, which fluoresces upon binding to MG dye. The mRNA is then translated by ribosomes into deGFP protein. (b) Simplified view of TX-only system: TX proceeds as in (a), but translation is inhibited by tetracycline, which binds to ribosomes and inhibits translation initiation. (c) Simplified view of TL-only system: MG aptamer-deGFP mRNA, rather than DNA, is added to the system, and the mRNA is translated into deGFP protein. (d-f) Integrated mRNA (top) and maximum deGFP measurements (bottom) for the (d) TX-TL system, (e) TX-only system, to which 200 μg/mL tetracycline was added, and (f) TL-only system, where 0.3 μM mRNA was added at the beginning of the reaction. All reactions shown used lysate Preparation 2, and the TX-TL and TX-only systems used 5 nM DNA. Each measurement is the average of three replicates for that experimental condition. Color bars are scaled separately for each plot.

at 3PGA concentrations ranging from 0 to 30 mM and 0 to 10 mM added Mg^{2+} (Figure 2.6e). Overall transcription was also higher, likely due to the abundance of energy in the absence of translation. Meanwhile, in the TL-only system (Figure 2.6c), higher deGFP yields were achieved, as before, at low Mg^{2+} and high 3PGA concentrations, despite reduced mRNA degradation in the regime of high Mg^{2+} and low 3PGA concentrations (Figure 2.6f).

These data suggest that the TX-TL trade-off is caused by a combination of translation optimization at low Mg^{2+} and high 3PGA concentrations, increased MG aptamer stability at high Mg^{2+} and low 3PGA concentrations, and competition for resources in the TX-TL system. In other words, optimal translation occurs where conditions are ideal for that process, and optimal transcription occurs where translation is suboptimal and leaves more fuel and energy resources for transcription. While these experiments did not shed light on the mechanism governing translation optimization at lower Mg^{2+} and higher 3PGA concentrations, they suggest that the TX-TL trade-off arises at the translational level in 3PGA-fueled systems.

TX-TL trade-off is absent when TX-TL systems are supplied with no fuel or Mg^{2+} and additional energy

The TX-TL decoupling experiments had implied that the TX-TL trade-off arose in part due to competition for fuel and energy resources between transcription and translation. By this hypothesis, TX-TL systems with abundant energy should not fall along the trade-off curve, particularly in a regime of low Mg^{2+} concentration where both transcription and translation were favorable when not limited by a competing process (Figure 2.6e,f). To test this hypothesis, we next performed experiments in which TX-TL systems were supplied with an excess of energy. To mitigate the potential effects of waste accumulation that came with adding high levels of central carbon-based fuel sources, we decided against using any central carbon fuel source (i.e., 3PGA, maltose, pyruvate, or succinate) for energy regeneration. As Mg^{2+} also had a translation-inhibition effect, for these experiments, we also decided against adding additional Mg^{2+}. Instead, to explore the space of different energy sources and concentrations, we performed a three-dimensional panel of ATP versus GTP versus NTPs, where each solution was added at a final concentration of 0, 5, 10, or 15 mM. The results of these experiments are shown in Figure 2.7.

As expected, TX-TL systems supplied with additional energy molecules and no fuel or no Mg^{2+} did not fall along the previously found trade-off curve corresponding

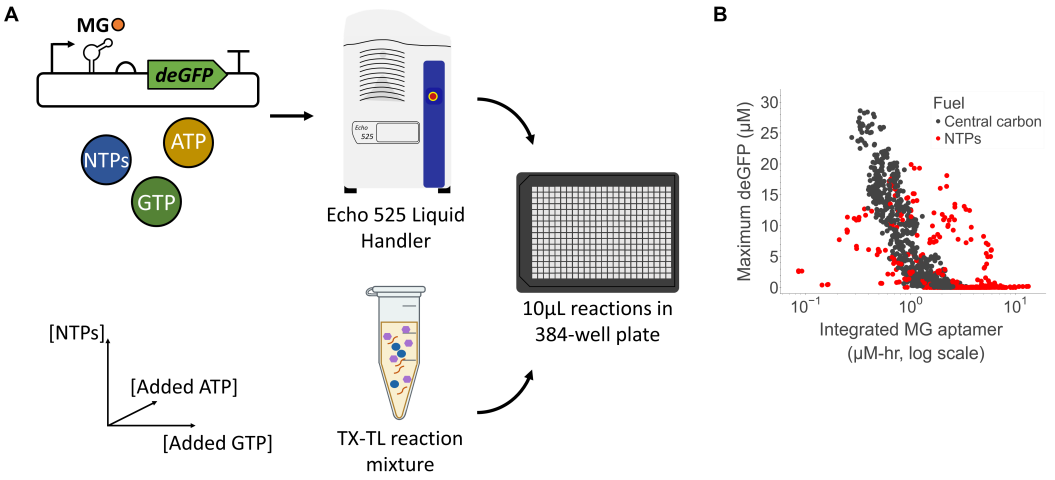

Figure 2.7: Absent TX-TL trade-off in the absence of fuel or Mg^{2+}. (a) Overview of experimental workflow. (b) Maximum deGFP values versus integrated MG aptamer value. A log scale was chosen for the latter axis to prevent high MG aptamer values from skewing the data in a way that made it difficult to view the original trade-off data. Each point represents one of three replicates of a particular set of NTP, added ATP, and added GTP concentrations, colored by the fuel type. Here, the "central carbon" fuel data is the same as in Figure 1, and those reactions all contain 4.8 mM NTPs. The "NTPs" fuel data reflect experiments where no central fuel or Mg^{2+} has been added. The data shown reflect experiments performed in two preparations of cell lysate, Preparation 1 and Preparation 2 (see Materials and Methods for details), and all experiments were performed using 5 nM DNA.

to that DNA concentration (5 nM), and overall, these NTP-fueled systems displayed a weaker trend of decreasing deGFP with increasing integrated MG aptamer (Spearman's rho correlation of -0.47) compared to central carbon-fueled systems (Spearman's rho correlation of -0.90). Additionally, NTP-fueled systems could achieve deGFP yields comparable to systems supplied with pyruvate or maltose, and integrated MG aptamer yields 3-10× higher than in TX-TL systems supplied with those fuels and Mg^{2+}. While there was no clear trend in ATP, GTP, or total NTP concentration for the data shown in Figure 7B, generally, as the concentration of NTPs increased, integrated MG aptamer values increased, and deGFP values decreased (Figure S2.7), which is consistent with a previous finding [28] The decrease in deGFP yields despite the abundance of energy was likely due to the NTP chelation of Mg^{2+}, which is necessary for ribosomes and other translation machinery. Although Mg^{2+} was not directly added to the reactions, it was present at a concentration of around 4 mM due to the presence of S30B buffer (used in the preparation of cell lysate) in the reaction. Our results suggest that fuel-supplied TX-TL systems

are indeed energy-limited and that the TX-TL trade-off curve exists in part due to competition for a limited pool of energy for transcription and translation.

The data revealed three additional insights. First, systems with no fuel or no Mg^{2+} and high NTPs often exhibited unusual transcriptional and translational dynamics (Figure 2.5). Some systems exhibit long time delays in transcription (Figure 2.5a) or translation (Figure 2.5e,f). Other systems exhibited biphasic expression (Figure 2.5b,d) or steady-state transcription rates as opposed to the typical transcription pulse (Figure 2.5c).

Second, although NTP-fueled TX-TL systems did not achieve protein yields as high as those achieved in systems with 3PGA, supplying systems with 10 mM NTPs helped achieve integrated MG aptamer and deGFP yields comparable to systems with about 5 mM NTPs and 10 mM 3PGA, the latter of which should have regenerated 10 mM ATP. This suggests that while energy regeneration is likely occurring in 3PGA-fueled systems, energy being regenerated is not being used efficiently. A large fraction of that regenerated energy, perhaps the majority, is likely fueling metabolic processes that are irrelevant to transcription or translation.

Third, if the TX-TL trade-off curve was indicative of a greater trade-off between efficient energy regeneration and waste minimization, then any potential translation-inhibiting waste product was likely not produced as a result of total transcription, since relatively high maximum deGFP yields were achieved with high integrated MG aptamer values in the case of NTP-fueled systems (Figure 2.7b). The waste product also did not appear to be solely a product of fast transcription; while there was negative correlation between the maximum rate of transcription and maximum deGFP in central carbon-fueled systems (Spearman's rho correlation of -0.63), there was a positive correlation between the maximum rate of transcription and maximum deGFP in NTP-fueled systems (Figure S2.9). These data suggest that the waste was likely derived from the metabolism of the central carbon fuels. Mg^{2+} versus fuel panels performed with all fuels in the regime of low DNA concentration (i.e., 1 nM) showed that in a transcription-limited regime, central carbon-fueled TX-TL systems indeed preferred low fuel concentrations for high deGFP yields (Figures S2.10-S2.13). These results suggest that these systems were not able to sufficiently utilize central carbon-fueled energy regeneration and thus could not rapidly make protein before waste accumulated compared to systems with 5 nM DNA, thereby supporting the idea that waste products were, in part, central carbon metabolism-derived.

2.3 Discussion

An improved understanding of cell-free TX-TL systems is essential for scaling up, expanding the scope of, and improving the performance of TX-TL applications in academic and industrial settings. By using metabolic perturbations as a tool to gain insight into the behavior of TX-TL systems in different metabolic regimes, this study has shed light on how Mg^{2+} and fuel contribute to TX-TL variability and how these two components and NTPs affect TX-TL performance. Our results indicate the presence of a trade-off between transcription and translation in *E. coli*-based TX-TL systems and show clear roles for how Mg^{2+}, fuel, cell lysate preparation, and other factors affect transcription and translation and give rise to TX-TL variability.

Armed with these insights, other users of TX-TL systems aiming to reduce variability and standardize their systems may consider calibrating the concentrations of the relevant small molecules (fuel, Mg^{2+}, and DNA) for their application so that TX-TL curves for different systems have similar locations, shapes, and other characteristics. By characterizing different preparations of cell lysate by the shape and location of their trade-off curves, for example, we can understand their respective transcriptional and translational limits. Beyond reducing variability and improving standardization, this study also has relevance for efforts aimed at increasing the predictability and performance of TX-TL systems for desired uses. A user can optimize transcription versus translation optimization in different preparations of cell lysate by choosing the appropriate set of fuel types, fuel concentrations, and Mg^{2+} concentrations for a particular genetic program, whether it be a complex transcriptional circuit or a simple program for maximum protein yield. The data included with this paper provide hundreds of unique reaction conditions that can serve as a starting point for exploring conditions that are optimized for high protein yields, long reaction lifetime, specific temporal dynamics, or other desired behaviors.

In addition to providing insight into design considerations for TX-TL systems, the TX-TL trade-off curve, initially a surprising finding, has also provided a simple yet powerful way of gaining insight into fundamental trade-offs in fuel and energy metabolism. Taken together, our results suggest that the TX-TL trade-off is present in energy-limited systems and is indicative of a trade-off between energy regeneration and waste accumulation that results from fuel metabolism. In other words, while fuel molecules enable energy regeneration, their own metabolism also results in waste accumulation (through the generation of immediate or downstream products) that affects TX-TL processes. While the identities of the waste molecules remain

unknown, our results suggest that in 3PGA-fueled systems, the waste is partially 3PGA-derived and affects translation. This insight, along with results from the TX-TL decoupling experiments, have helped us to create a new model of cell-free metabolism coupled to cell-free TX-TL (Figure 2.8). While this model has not been validated computationally, doing so may enable improved prediction of TX-TL performance, perhaps even in non-lysate-based TX-TL systems (e.g., PURE-based systems [16]), and this remains an active area of future work.

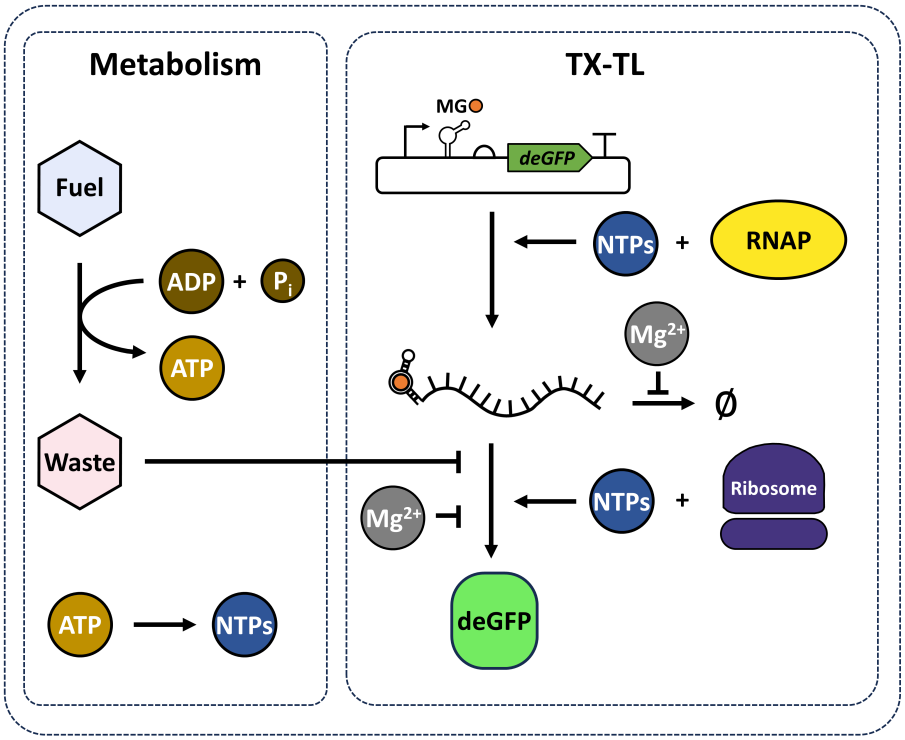

Figure 2.8: New model for cell-free metabolism coupled to cell-free TX-TL. The conversion of fuel to waste regenerates energy, which can power transcription and translation, but the accumulation of waste inhibits translation. The fuel-energy-waste paradigm is derived from an existing model [33]. This model's key contribution is providing roles for Mg^{2+} via its inhibition of mRNA degradation and translation.

In revealing the fundamental metabolic trade-offs in TX-TL systems, this work has also shed light on why previous studies aimed at increasing protein yield have been largely unsuccessful. Our data suggest that low Mg^{2+} concentrations, strong promoters, and high DNA concentrations - and high 3PGA concentrations where 3PGA is used - are necessary for high deGFP yields. However, it is not possible to remove more Mg^{2+} from the system without compromising the function of proteins

in the cell lysate, nor is adding more fuel possible, as the inability of TX-TL systems to take advantage of faster energy regeneration will make faster waste accumulation an issue at high fuel concentrations. Adding too much DNA may skew the systems toward transcription rather than translation. Previous studies aimed at improving deGFP yields have focused on other mechanisms of energy regeneration and waste mitigation, such as using combinations of fuels like 3PGA and maltose [34], and such approaches and others, including at the level of plasmid design, will be necessary for vastly improving protein yields in lysate-based TX-TL systems.

Overall, by elucidating the effects of cell-free metabolism on TX-TL systems, this work lays a foundation for improving TX-TL performance, lifetime, standardization, and prediction. Ultimately, it represents one of many such steps that will be necessary for further improvement of TX-TL systems, whether that be for applications in biomanufacturing, for gaining insight into natural biological systems, or for the development of synthetic life.

2.4 Materials and methods

Preparation of cell lysate

Cell lysate was prepared from *E. coli* BL21 Rosetta2 cells using the protocol established by Sun and co-workers [14] with some modifications. Briefly, cells were grown sequentially in 6 mL, 100 mL, and 1 L cultures, where smaller cultures were used to inoculate larger ones. Once 6 L of culture had grown to roughly an OD600 of 2, cells were repeatedly centrifuged and washed with S30B buffer by resuspension. Cells were then resuspended in S30B buffer and subjected to cell lysis.

For lysate Preparation 2 and Preparation 3, cells were resuspended at 1.4 g of cells per mL of S30B buffer and lysed by a French cell press at a pressure of 640 psi. For lysate Preparation 1, cells were resuspended to 1 g of cells per mL of S30B buffer and lysed by sonication at a probe frequency of 20 kHz and an amplitude of 50%. Cells were sonicated at 10 s ON/OFF intervals for a total of 60 s ON (6 ON/OFF cycles), resulting in approximately 300 Joules of energy delivered. After both methods of cell lysis, 3 µL of 1 M DTT was added per mL of the cell lysate, and the lysates were then centrifuged to remove cell debris. All preparations of lysate were then subjected to a 1 h runoff reaction at 37°C, after which they were subjected to centrifugation to remove additional debris.

Lysate Preparation 2 and Preparation 3 were additionally subjected to dialysis at 4°C via Slide-a-Lyzer G3 cassettes (10 kDa, 15 mL) placed in a beaker containing

S30B buffer and a magnetic stir bar to facilitate diffusion. Excess air was removed by using a syringe. Lysate Preparation 2 was dialyzed for 4 h (where cassettes were transferred to a beaker of fresh S30B at the 2 h mark) at 140 rpm. Lysate Preparation 3 was dialyzed for 2 h (where cassettes were transferred to a beaker of fresh S30B at the 35 min mark) at 160 rpm.

Finally, both preparations of cell lysate were aliquoted, flash-frozen in liquid nitrogen, and stored at –80°C until further use. Bradford assays determined that the final protein concentrations for the cell lysates were 30-40 mg/mL.

Cloning plasmids used to express deGFP

The P_{OR1OR2}-MG aptamer-deGFP plasmid used to express deGFP was originally prepared by Dan Siegal and modified by Zoila Jurado via site-directed mutagenesis to change the P_{T7} promoter to a P_{OR1OR2} promoter and the T7 terminator to a T500 terminator. This plasmid is the P_{OR1OR2}-MG aptamer-UTR1-deGFP-T500. The P_{Tet}-MG aptamer-UTR1-deGFP-T500 plasmid was subsequently constructed using site-directed mutagenesis to change the P_{OR1OR2} promoter to a P_{Tet} promoter to make expression results as comparable as possible. The P_{T7}-MG aptamer-UTR1-deGFP-T7terminator plasmid was originally prepared by Siegal and modified using site-directed mutagenesis to add a few extra bases to the P_{T7} promoter. The P_{Tet}-F30Pepper-UTR1-mTurquoise2-ECK120029600 plasmid was constructed using Golden Gate Assembly of CIDAR MoClo part plasmids. All plasmid sequences are given in the Supporting Information section.

Preparation of template DNA plasmids

In experiments in which the P_{OR1OR2}-MG aptamer-UTR1-deGFP-T500 plasmid was used, template DNA for the cell-free reactions was prepared from *E. coli* KL740 cells (purchased from Arbor Biosciences) that had been transformed with the plasmid described above. Cells were grown overnight at 30°C, in lysogeny broth (LB) medium supplemented with 100 μg/mL carbenicillin, and either Mini-prepped (using a Qiagen Mini-prep kit) or Midi-prepped (using a Macherey-Nagel NucleoBond Xtra Midi kit) the next day using the appropriate protocols. When Mini-prepping, DNA was eluted with nuclease-free water; when Midi-prepping, after the concentration step, DNA was eluted with IDTE buffer (10 mM Tris-HCl, 0.1 mM EDTA).

The P_{Tet}-MG aptamer-UTR1-deGFP-T500, P_{T7}-MG aptamer-UTR1-deGFP-T7terminator, and P_{Tet}-F30Pepper-UTR1-mTurquoise2-ECK120029600 plasmids were

prepared from cells grown overnight at 37°C in LB medium supplemented with 100 µg/mL carbenicillin (for the deGFP plasmids) or 50 µg/mL kanamycin. The cells were Mini-prepped using a Qiagen Mini-prep kit, where DNA was eluted with nuclease-free water.

The P_{T7}-UTR1-deGFP-MG aptamer-T7terminator plasmid was constructed from the plasmid pTXTL-T7p14-deGFP (Arbor Biosciences, myTXTL Toolbox 2.0 plasmid collection, now discontinued). The plasmid was modified by the insertion of a MG aptamer sequenced after the deGFP sequence with the use of the following primers: CGAGGGGATCCCGACTGGCGAGAGCCAGGTAACGAATGGATCCCTTAGGAGATCCGGCTG (forward primer) and GGGATCCATTCGTTACCTGGCTCTCGCCAGTCGGGATCCCCTCGAGTTAGATCCCGGC (reverse primer). The template plasmid was first added to a PCR reaction with these primers, using an annealing temperature of 60°C and an elongation time of 2.5 min. Next, the PCR reaction was subjected to a 1 h DpnI digest to remove the template DNA via the addition of 0.25 µL of DpnI enzyme (purchased from New England Biolabs at 20,000 units/mL) per 25 µL reaction and subsequent incubation at 37°C for 1 h. Next, PCR cleanup was performed using the Qiagen Mini-prep kit to extract linear DNA. Finally, the linear DNA was recircularized by performing a Gibson reaction using NEBuilder HiFi DNA Assembly Master Mix, after which 0.5 µL of the reaction mix was then used to transform 50 µL of competent cells, which were grown overnight at 37°C on LB agar plates with 100 µg/mL carbenicillin. Transformed colonies were sequence verified for insertion of the MG sequence and subsequently cultured overnight at 37°C with 100 µg/mL carbenicillin and Mini-prepped for plasmid DNA extraction.

Preparation of cell-free reactions

Cell-free reactions were prepared as per the protocol by Sun and co-workers [14]. Unless otherwise noted, each reaction consisted of the following: 33% (by volume) of cell lysate, 1.5 mM of each amino acid (except for leucine, which was added at 1.25 mM), 4.8 nM of NTP mix (containing 1.5 mM each of ATP and GTP, 0.9 mM each of CTP and UTP, pH adjusted to 7.5 using KOH), 50 mM HEPES pH 8, 0.2 mg/mL tRNA, 0.26 mM coenzyme A, 0.33 mM NAD+, 0.75 mM cyclic AMP (cAMP), 0.068 mM folinic acid, 1 mM spermidine, 10 µM MG dye, and 30 mM 3PGA. Depending on the preparation of cell lysate, a standard reaction used either 8 mM magnesium glutamate and 80 mM potassium glutamate (for lysate Preparations 2 and 3) or 6 mM magnesium glutamate and 140 mM potassium glutamate (for

lysate Preparation 1); these salt concentrations were chosen because they optimized deGFP expression in TX-TL reactions supplied with 1 nM P_{OR1OR2}-MG aptamer-deGFP plasmid for a particular lysate preparation (Figure S2.15). For the Mg^{2+} versus fuel panels, 3PGA and Mg^{2+} were omitted from the master mix, and the appropriate concentration of Mg^{2+} and fuel was added to reactions individually. Finally, depending on the experiments, a variable amount of DNA plasmid was added, and the remaining volume of the 10 µL of reaction mixture was filled with nuclease-free water.

As reactions were all performed in 384-well glass-bottom plates, water, DNA, and other added components were titrated into the TX-TL reaction using the Echo 525 liquid handler, while the remaining components were added to a bulk solution and electronically dispensed by a multidispense pipette. Unless otherwise specified, all reactions containing DNA were supplied with the P_{OR1OR2}-MG aptamer-deGFP plasmid. To prevent the reaction from starting before all the components had been added in, all reagents were kept on ice until they were added to the reaction mixture and added sequentially to reduce evaporation and/or degradation. First, a master mix minus the cell lysate was created and kept on ice in an Eppendorf tube; then, components to be added by Echo were added to the 384-well plate, where all stock concentrations were diluted to less than 500 mM so that they could be effectively dispensed via Echo; next, the cell lysate was added to the master mix; finally, the master mix was pipetted to the wall of each well. Once the plate was covered with a plastic seal, it was centrifuged at 4000*g* for 1 min at 4°C. Finally, the bottom of the plate was quickly cleaned by Kimwipe to remove any debris and immediately transferred to a BioTek H1MF plate reader that had reached its set point of 29°C.

Preparation of no-fuel, No Mg^{2+} cell-free reactions

Reactions were prepared as described in the "Preparation of cell-free reactions" with minor changes. No fuel or additional Mg^{2+} were added to the reactions, apart from what was already there from the preparation of the cell lysate. For the addition of the NTP mix, we prepared an NTP stock solution at a molar ratio of 1.5:1.5:0.9:0.9 for ATP/GTP/CTP/UTP, and the pH was adjusted to 7.5 using KOH. For the ATP and GTP solutions, we prepared stock solutions in nuclease-free water. Each solution was added at 0, 5, 10, or 15 mM.

Dynamic measurements of fluorescent molecules

Fluorescence measurements were performed by a BioTek H1MF plate reader at 29C, and measurements were read from the bottom of the plate every 3 min (preceded by 5 s of linear shaking) at excitation/emission wavelengths suitable for MG aptamer (610/650 nm, gain 150) and deGFP (485/515 nm, gain 61) for 18 h. For the experiment corresponding to Figure 4, excitation/emission wavelengths suitable for F30-Pepper (580/620 nm, gain 150) and mTurquoise2 (434/474 nm, gain 61) were used.

For MG aptamer and deGFP, arbitrary fluorescence units were converted to micromolar concentrations using a calibration curve prepared using purified deGFP protein and MG aptamer mRNA. To create a deGFP fluorescence calibration curve, serial dilutions of eGFP (purchased from Cell Biolabs) were performed in 1× PBS, after which 3 sample replicates of 10 µL each were loaded onto a 384-well plate and read by a BioTek H1MF plate reader at 29°C and at excitation/emission wavelengths of 485/515 and a gain of 61. Three technical replicates were read over 3 min at 1-min intervals to generate 4 points per replicate, and the average of these 12 points was used as a single point at a given concentration through which the calibration line was fit with a zero intercept.

To create a MG aptamer fluorescence calibration curve, mRNA of MG aptamer sequence only - specifically rArCrUrGrGrArUrCrCrCrGrArCrUrGrGrCrGrArGrCrCrArGrCrArGrGrUrArCrG rArArUrGrGrArUrCrCrArArU - was purchased from IDT DNA. The lyophilized mRNA was resuspended in nuclease-free water, and its concentration was determined by a NanoDrop 2000c. Next, serial dilutions of MG aptamer mRNA were performed in 1× PBS containing 10 µM MG dye, after which 3-4 sample replicates of 10 µL each were loaded onto a 384-well plate and read by a BioTek H1MF plate reader at 29°C and at excitation/emission wavelengths of 610/650 and a gain of 150. Four technical replicates were read over 10 min at 2.5 min intervals to generate 5 points per replicate, and the average of these 20 points was used as a single point at a given concentration through which the calibration line was fit with a zero intercept. The slope of the background-subtracted calibration curve was used to calibrate the measurements.

mRNA purification for a translation-only system

To obtain an mRNA sequence containing MG aptamer-UTR1-deGFP, a linear DNA template was first prepared, followed by DNA isolation, *in vitro* transcription, DNase

treatment, and mRNA isolation. First, for the generation of the linear DNA template, primers of the following sequences were first used to amplify the relevant sequence off the POR1OR2-MG aptamer-deGFP plasmid by PCR: CCAGAAAAC-CGAATTTTGCTGG and ATGATAAAGAAGACAGTCATAAGTGCG. A 1 mL PCR reaction was performed using NEB Q5 2X Master Mix and run for 30 cycles with an elongation time of 45 s and an annealing temperature of 65°C.

After the PCR reaction was performed, the PCR was aliquoted in three 1.7 mL Eppendorf tubes (i.e., 333 µL per tube), and DNA was precipitated by adding 33 µL of 3 M sodium acetate and 1 mL of 100% ethanol per tube. After chilling the tubes at –80°C for 20 min, the tubes were centrifuged at 16,000*g* for 30 min at 4°C. Finally, all supernatant was pipetted out, and residual ethanol was allowed to evaporate by leaving the tubes open and uncovered at room temperature. The DNA was resuspended in 50 µL of nuclease-free water per tube.

In vitro transcription was performed using the HiScribe T7 High Yield RNA Synthesis Kit, and instructions included in the kit's manual were used for DNase I treatment of the reaction. Finally, the synthesized mRNA was isolated using the PureLink RNA Mini kit. 100% ethanol was first added to the reaction to a final concentration of 35%, after which the kit's "Protocol for RNA clean-up and purification from liquid samples" was used (omitting the lysis step). mRNA concentration was determined by a NanoDrop 2000c.

Translation inhibition using tetracycline

The translation inhibition experiments were performed in lysate Preparation 2 by adding 200 µg/mL tetracycline to the TX-TL reactions. Stock tetracycline solutions were created at 80 mg/mL in DMSO, where they were stored at –80°C until further use. For addition to TX-TL reactions, the stock solution was diluted to 5 mg/mL in nuclease-free water and subsequently dispensed using an Echo 525 liquid handler. To determine the optimal concentration of tetracycline to use for translation-inhibition, titrations were performed (see Figure S14).

Data analysis

Fluorescence measurements of deGFP and MG aptamer were converted to micromolar concentrations via the calibration curves. Maximum deGFP concentration was determined to be the maximum deGFP concentration achieved for a given experimental condition at any point over the course of the 18 h experiment. Integrated MG aptamer measurements were made by using the NumPy [39] **trapz** function

for numerical integration using the trapezoidal method. Plots were generated using the Python package Bokeh [40]. The Jupyter notebooks that were used for creating tidy data and for subsequent data analysis and plot generation are included with this work, in addition to all the data that was collected for this study.

Spearman's rho correlation computation

For figures where a Spearman's rho correlation value was computed, the SciPy [41] **stats.spearmanr** function was used to compute correlation values. A Spearman rho correlation value has a minimum possible value of –1, corresponding to a perfect negative rank correlation between two variables, and a maximum possible value of 1, corresponding to a perfect positive rank correlation between two variables. A value of 0 suggests no rank correlation.

Where a bootstrapped Spearman's rho correlation value was computed, the pseudocode below shows the algorithm used to perform the computation. Briefly, we first split our data into training and test sets in a 75/25 ratio, where the predictor variable was Mg^{2+} or 3PGA and the predicted data were the 2D trade-off data. We next trained a partial least squares regression (PLS Canonical) model on the training data using the Python Scikit-learn [42] package. This training simultaneously reduced the dimensionality of the trade-off data from 2D to 1D; redimensionalized the predictor variable (i.e., Mg^{2+} or 3PGA) so that it had a mean value of zero; and created a model capable of predicting position along the 1D trade-off data for the predictor variable. The model was then used to map the test data to the new 1D spaces. A Spearman rho correlation value was computed for the mapped test data between the 1D predictor variable and the 1D trade-off data using the SciPy [41] **stats.spearmanr** function. This process was repeated 5000 times to randomize the splitting of data. The mean and standard deviation of this "bootstrapped" Spearman's rho correlation value are reported for each plot where applicable.

Although many cross decomposition methods exist, we chose PLS regression because it is better at preserving variance compared to methods such as principal component regression (PCR) during the dimensionality reduction step (due to the addition of supervising learning). PLS is also particularly suitable when there is collinearity among columns of the predictor or predicted data (as in the case of MG aptamer and deGFP, where we observed a negative correlation between the two variables). The Python Scikit-learn package has several functions for PLS: PLSCanonical, PLSSVD, and PLSRegression (which can implement the PLS1 and

PLS2 algorithms); in the case of a 1D PLS model, as we have chosen, the underlying algorithm is the same for all of them, so we arbitrarily chose PLSCanonical.

Due to the redimensionalization of data during PLS regression, the bootstrapped Spearman's rho correlations range from 0 to 1 (unlike the traditional Spearman's rho correlation that ranges from -1 to 1). In the bootstrapped case, a value of 0 corresponds to no rank correlation, and a value of 1 corresponds to a perfect rank correlation (with a direction of positive or negative stated in the Results section where applicable).

ALGORITHM 1: BOOTSTRAPPED SPEARMAN'S RHO CORRELATION

```
function BootstrapPLS(X, Y, n_bootstrap):
    Input:
        Y: trade-off curve 2-D coordinates, Y ∈ ℝ^(sx2), where
        Y is a two-column matrix with one column of MG
        aptamer values and the other column of deGFP
        values and s is the number of points on the trade-off
        curve
        X: corresponding values of the predictor variable X ∈
        ℝ^(sx1), where X is a column vector of length s (e.g., a
        column vector of Mg2+ values where each value has
        a corresponding 2-D coordinate of MG aptamer and
        deGFP values)
        n_bootstrap: number of iterations of the basic
        procedure (bootstraps), set as a default to 5000
    Output:
        mean and standard deviation of the Spearman's rho
        correlation values obtained over all bootstraps

initialize one-dimensional PLSCanonical model
initialize spearman_rho_bootstrap vector to store
Spearman's rho correlation values
i = 0
while i < n_bootstrap:
    randomly shuffle rows of X, Y to create
    X_shuffled, Y_shuffled
    split X_shuffled into X_train (top ¾ of total
    rows) and X_test (bottom ¼ of total rows)
    split Y_shuffled into Y_train (top ¾ of total
    rows) and Y_test (bottom ¼ of total rows)
    train PLSCanonical model on X_train, Y_train
        X_train is normalized to a mean value
        of 0 → X_train_r, and Y_train is
        simultaneously re-dimensionalized
        from 2D to 1D → Y_train_r using
        supervised learning to maximize the
        covariance between X_train_r and
        Y_train_r
        the PLSCanonical model is trained to
        find α ∈ ℝ that satisfies Y_train_r =
        α*X_train_r
    transform X_test, Y_test into X_test_r,
    Y_test_r using trained PLSCanonical model
    compute Spearman's rho correlation p between
    X_test_r and Y_test_r
    spearman_rho_bootstrap[i] = p
    i ← i +1
compute mean, standard deviation of
spearman_rho_bootstrap array → p_mean, p_std
return p_mean, p_std
```

Acknowledgments

The work described here would not be possible without the initial ideas that came out of extensive discussions with William Poole. His suggestions to probe the roles of Mg^{2+} and different fuel sources helped generate new questions and analyses that ultimately led to the experiments discussed here, and we thank him for his insights. Apart from Poole, additional members of the lab – specifically Ankita Roychoudhury, David Alexander Johnson, Miryong (Miki) Yun, and Zoila Jurado – also contributed to the work shown here. Zoila was present in and contributed to many of these early discussions with William, and she also prepared the P_{OR1OR2}-MG aptamer-deGFP and P_{T7}-deGFP-MG aptamer plasmids used throughout this study. All four individuals helped prepare the cell lysate batches used in the experiments here, and we thank them for their help. We thank Paul Freemont for his helpful comments, particularly those pertaining to cell-free metabolism. We also thank lab members John Marken, Yan Zhang, and Zoila Jurado for providing critical feedback on this manuscript. Finally, ChatGPT was used to write part of the introduction section, which has been an interesting and helpful endeavor.

Research was sponsored by the Army Research Office and was accomplished under Cooperative Agreement Number W911NF-22-2-0210. The views and conclusions contained in this document are those of the authors and should not be interpreted as representing the official policies, either expressed or implied, of the Army Research Office or the U.S. Government. The U.S. Government is authorized to reproduce and distribute reprints for Government purposes notwithstanding any copyright notation herein.

2.5 Supporting information

Supporting figures

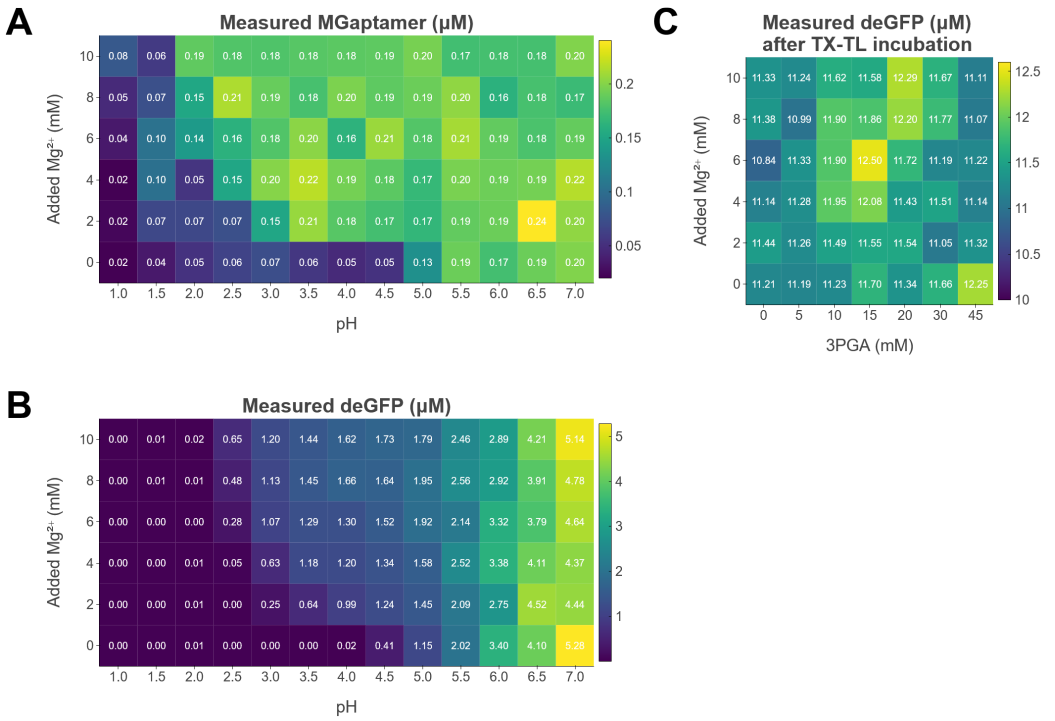

Figure S2.1: Exploring the dependence of MG aptamer and deGFP fluorescence on pH, Mg^{2+}, and 3PGA concentration. In (a) and (b), either (a) 0.2 μM MG aptamer-UTR1-deGFP mRNA or (b) 6.02 μM purified deGFP was added to 9 μL of phosphate-buffered saline (PBS) of the appropriate pH, some amount of 100 mM Mg-glutamate to the appropriate concentration, and nuclease-free water to 10 μL. The 384-well plate was incubated for 18 hours in a plate-reader at 29°C, and the endpoint concentrations, as determined by the fluorescence calibration data, are indicated in the plots shown. (c) 10 μM purified deGFP was added to TX-TL reactions and incubated at 29°C for 18 hours. The final deGFP concentrations, as reported by the fluorescence values that were calibrated to micromolar units, are shown in the figure. Fluorescence calibrations were performed using concentrations of 2-40 μM purified deGFP in PBS, where the linear slope of the calibration was dominated by higher concentrations of deGFP compared to the concentrations used in (b) and (c). Thus, fluorescence values are lower than expected in (b), where a higher percentage of the deGFP is likely adsorbed onto the walls of the 384-well plate (compared to the calibration), and higher than expected in (c), where a lower percentage of deGFP is adsorbed (compared to the calibration) since the proteins from the cell lysate are competing for adsorption.

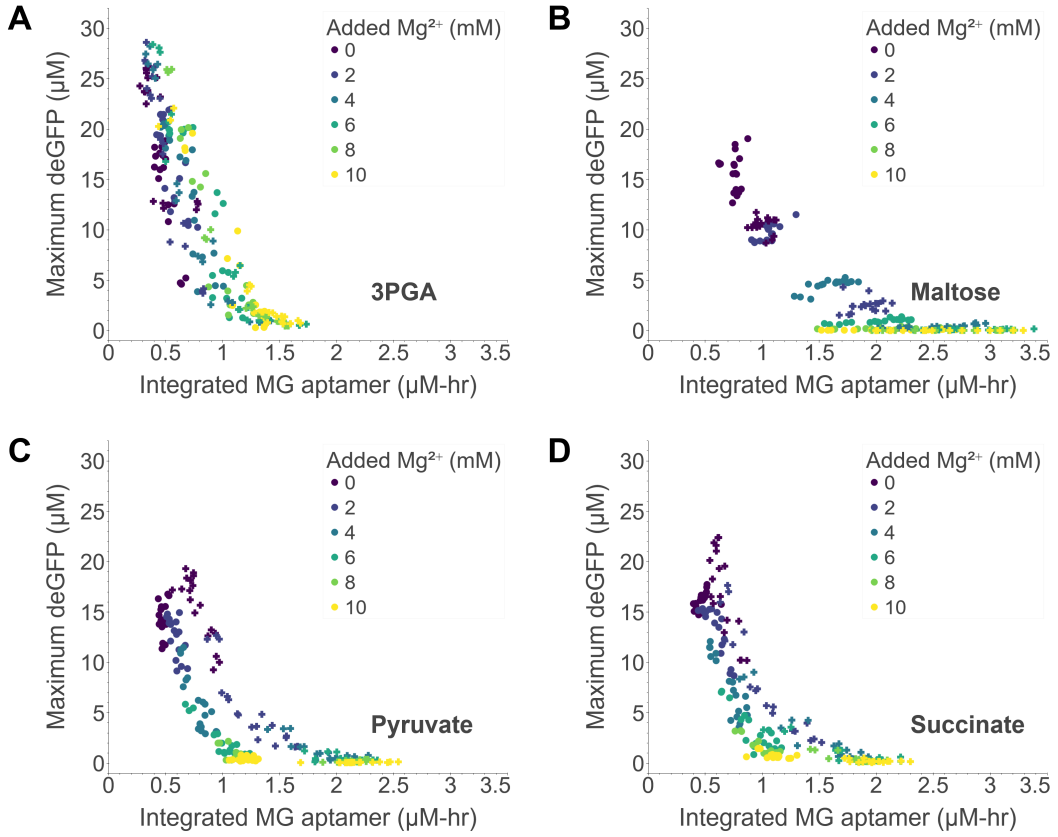

Figure S2.2: Effects of Mg^{2+} concentration on the TX-TL trade-off by fuel type. Each point represents one of three replicates of a particular set of fuel and Mg^{2+} concentrations, where fuel is either (a) 3PGA, (b) maltose, (c) pyruvate, or (d) succinate, with corresponding bootstrapped Spearman's rho correlations of 0.63 ± 0.05, 0.75 ± 0.04, 0.76 ± 0.04, and 0.78 ± 0.04, respectively. The data shown reflect experiments performed in two preparations of cell lysate, Preparation 1 (o) and Preparation 2 (+) (see **Materials and methods** for details), and all experiments were performed using 5 nM DNA.

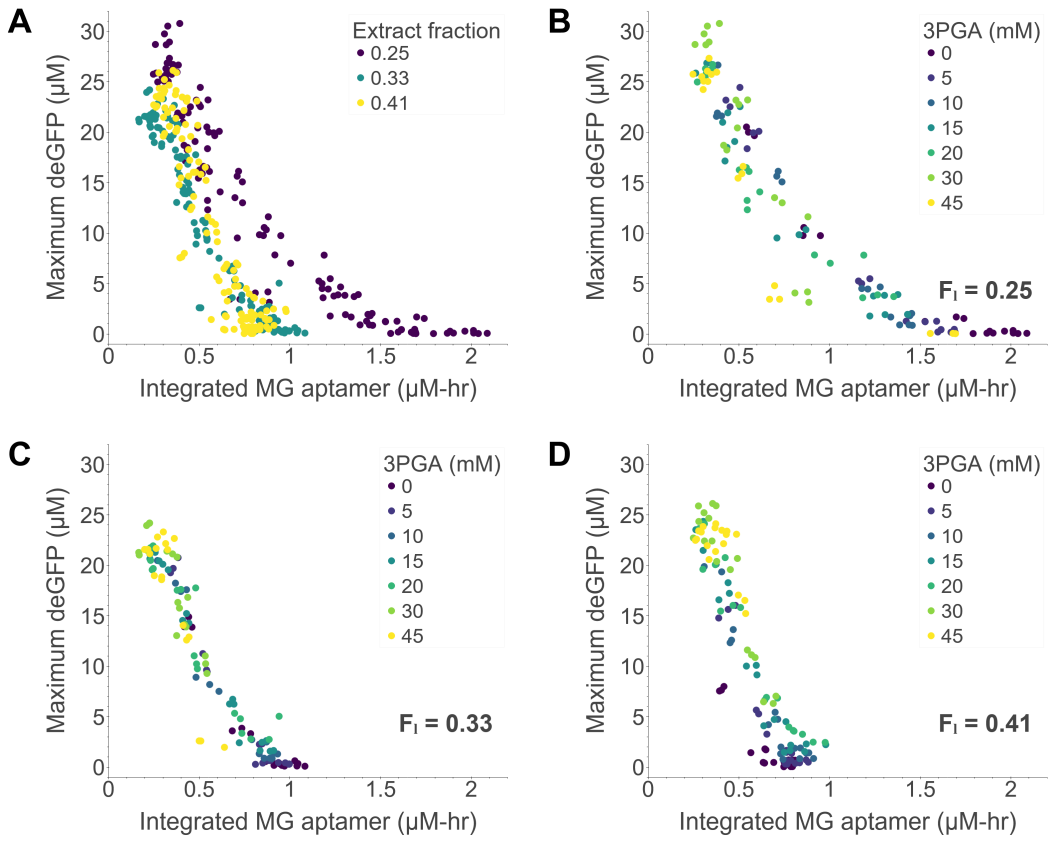

Figure S2.3: Effects of 3PGA concentration on the TX-TL trade-off across different lysate volume fractions. Each point represents one of three replicates of a particular set of 3PGA and Mg^{2+} concentrations. (a) Trade-off curves from three different lysate volume fractions are overlaid, where the lysate volume fraction is the volume fraction of a TX-TL reaction that is made up of cell lysate. (b) - (d) Individual lysate fraction trade-off curves are shown and points are colored by 3PGA concentration, where the curves correspond to lysate fractions (b) F_L = 0.25, (c) F_L = 0.33, the nominal case; and (d) F_L = 0.41, with corresponding bootstrapped Spearman's rho correlations of 0.49 ± 0.09, 0.63 ± 0.06, and 0.63 ± 0.05, respectively. The data shown reflect experiments performed in cell lysate Preparation 2 (see **Materials and methods** for details), and all experiments were performed using 5 nM DNA.

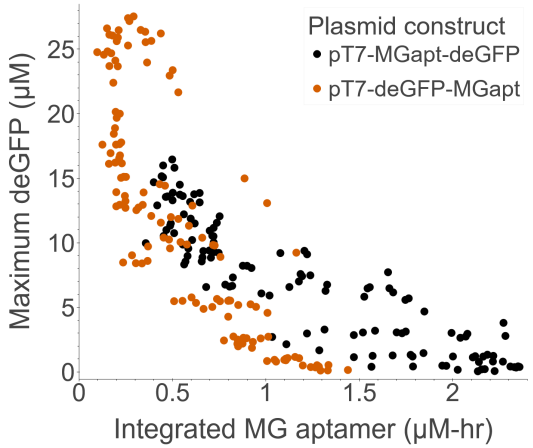

Figure S2.4: The TX-TL trade-off in systems expressing MG aptamer and deGFP in different order under a P_{T7} promoter. Each point represents one of three replicates of a particular set of 3PGA and Mg^{2+} concentrations. The data for P_{T7}-MG aptamer-deGFP are the same shown in Figures 2.4b and S2.5. The data shown reflect experiments performed in Preparation 3 of cell lysate (see **Materials and methods** for details), and all experiments were performed using 5 nM DNA.

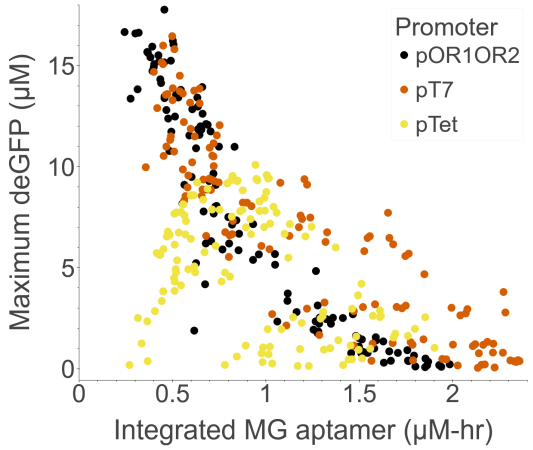

Figure S2.5: The TX-TL trade-off in systems expressing MG aptamer and deGFP under different promoters. Each point represents one of three replicates of a particular set of 3PGA and Mg^{2+} concentrations. The data are the same shown in Figure 2.4, albeit with the data from panels (a), (b), and (d) overlaid and colored by promoter type. The data shown reflect experiments performed in Preparation 3 of cell lysate (see **Materials and methods** for details), and all experiments were performed using 5 nM DNA.

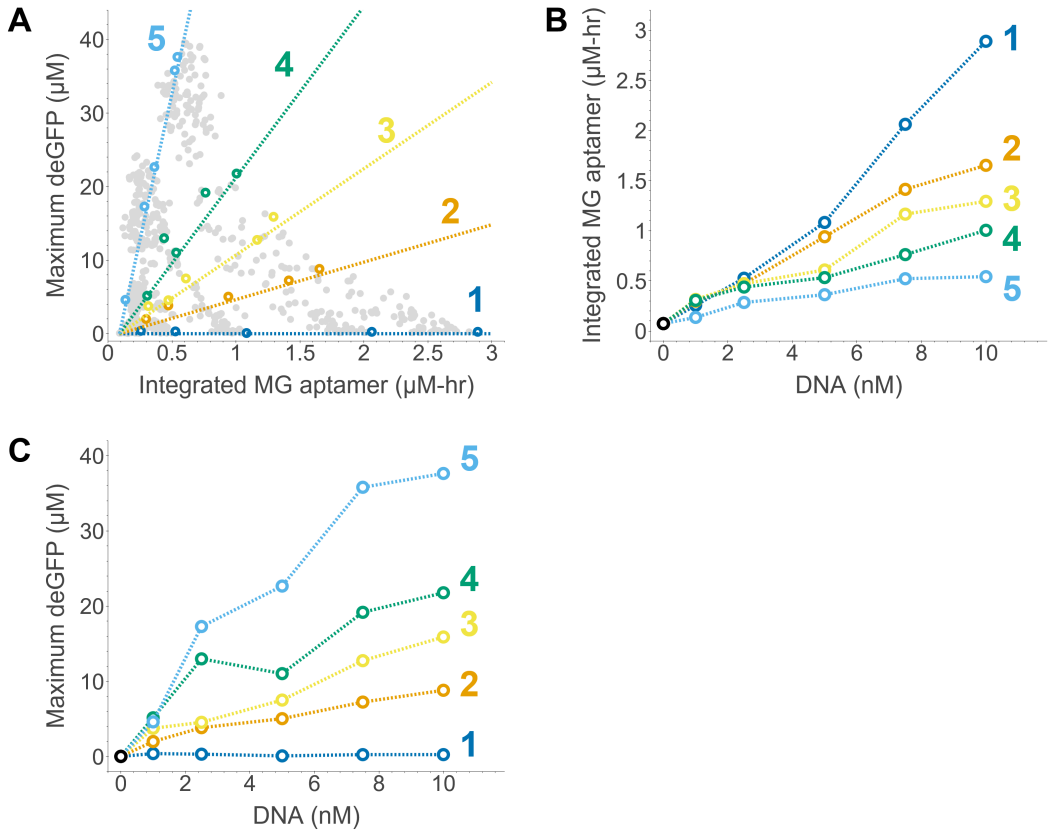

Figure S2.6: Scaling of transcription and translation with increasing DNA concentration. (a) Five lines were chosen to intersect the trade-off curves at roughly equi-angular intervals, and the point on each trade-off curve corresponding most closely to that line is highlighted. (b) Integrated MG aptamer versus DNA concentration for each of the intersecting lines for the points highlighted in (a). (c) Maximum deGFP versus DNA concentration for each of the intersecting lines for the points highlighted in (b). All experiments were performed in Preparation 2 of cell lysate. The data in (a) are the same shown in Figure 2.5.

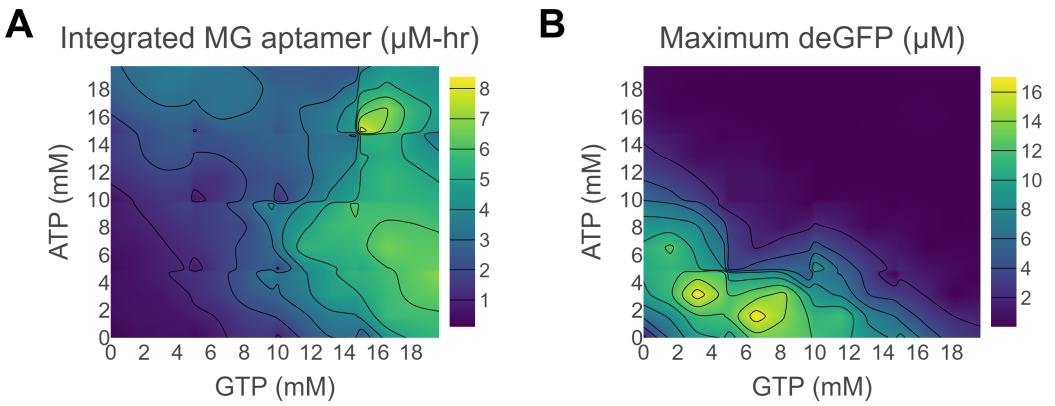

Figure S2.7: Exploring the effects of total ATP versus total GTP concentration in NTP-fueled systems. Here, the systems explored were TX-TL systems using 5 nM DNA to which no central carbon fuel nor Mg^{2+} had been added. Systems fueled by NTPs were implemented using a three-way panel of ATP versus GTP versus NTP mix, where each solution was added at 0, 5, 10, or 15 mM. As the NTP mix also contained ATP and GTP, the total concentrations of ATP and GTP were calculated for each system by summing the amount of ATP or GTP in the NTP mix with the added amount of ATP or GTP, respectively. Results were then averaged over three replicates and two preparations of cell lysate (Preparation 1 and Preparation 2). (a) Integrated MG aptamer values for NTP-fueled systems. (b) Maximum deGFP values for the NTP-fueled systems.

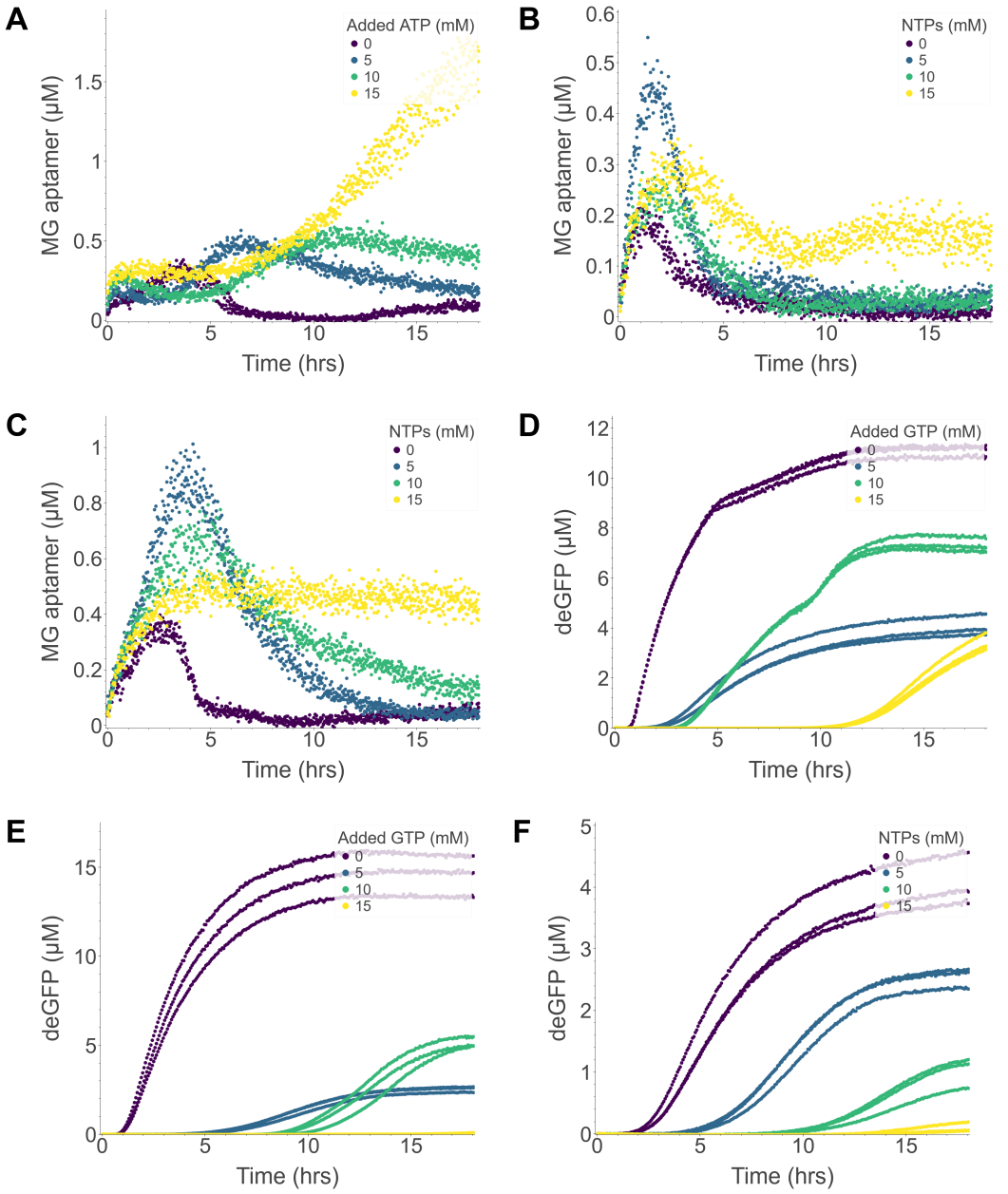

Figure S2.8: Examples of unusual and potentially desirable transcription and translation dynamics in TX-TL systems with no fuel or Mg^{2+} and with additional energy. These systems have the following (NTP, Added ATP, Added GTP) concentrations in mM, where a dashed line (-) indicates that a concentration is being varied in that plot: (a) (0, -, 15), (b) (-, 5, 5), (c) (-, 5, 10), (d) (0, 5, -), (e) (5, 5, -), (f) (-, 5, 5). (a) shows an example of a system (at 15 mM ATP) exhibiting time-delayed transcription albeit with a high MG aptamer yield that continues increasing even at 18 hours. (b) and (c) show examples of systems with biphasic and sustained transcription (both at 15 mM NTPs), respectively. (d) shows examples of systems with varying translation dynamics, ranging from a near-linear initial increase in deGFP (0 mM GTP),

biphasic translation (10 mM GTP), slow translation (5 mM GTP), and extremely time-delayed translation (15 mM GTP). (e) demonstrates that TX-TL systems that have time-delayed translation do not necessarily have lower deGFP yields, as indicated in the comparison between the 5 mM GTP and 10 mM GTP cases. (f) shows that under certain regimes (here at 5 mM ATP and 5 mM GTP), TX-TL systems can exhibit similar translation dynamics, albeit with time delays that are proportional to the amount of NTPs added to the system. Each point represents one of three replicates of a particular set of NTP, Added ATP, and Added GTP concentrations. All experiments were performed at 5 nM DNA in systems using the Preparation 2 lysate. Note: axes have different scales for each plot.

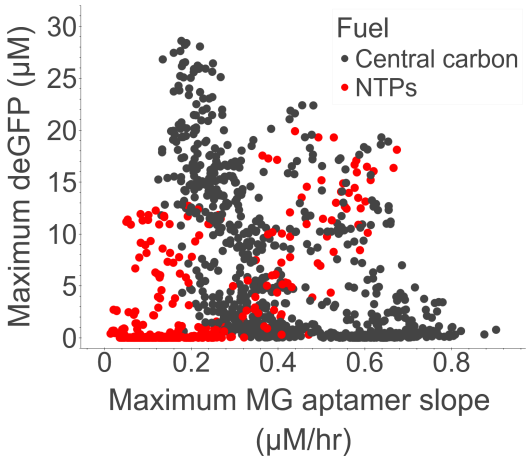

Figure S2.9: Maximum deGFP versus maximum MG aptamer slope for central carbon- and NTP-fueled systems. The data shown here are from the same experiments whose data is shown in Figure 2.7b. Each point represents one of three replicates of a particular set of NTP, added ATP, and added GTP concentrations, colored by the fuel type. Here, the "central carbon" fuel data is the same as in Figure 1, and those reactions all contain 4.8 mM NTPs. The "NTPs" fuel data reflect experiments where no central fuel or Mg^{2+} has been added. Maximum MG aptamer slope was calculated for each experimental condition by computing a series of linear regressions between MG aptamer and time for points spanning a rolling window of 1 hour over a total period of 18 hours; the maximum slope of MG aptamer expression over the 18-hour period was plotted for each experimental condition. The data shown reflect experiments performed in two preparations of cell lysate, Preparation 1 and Preparation 2 (see **Materials and methods** for details), and all experiments were performed using 5 nM DNA.

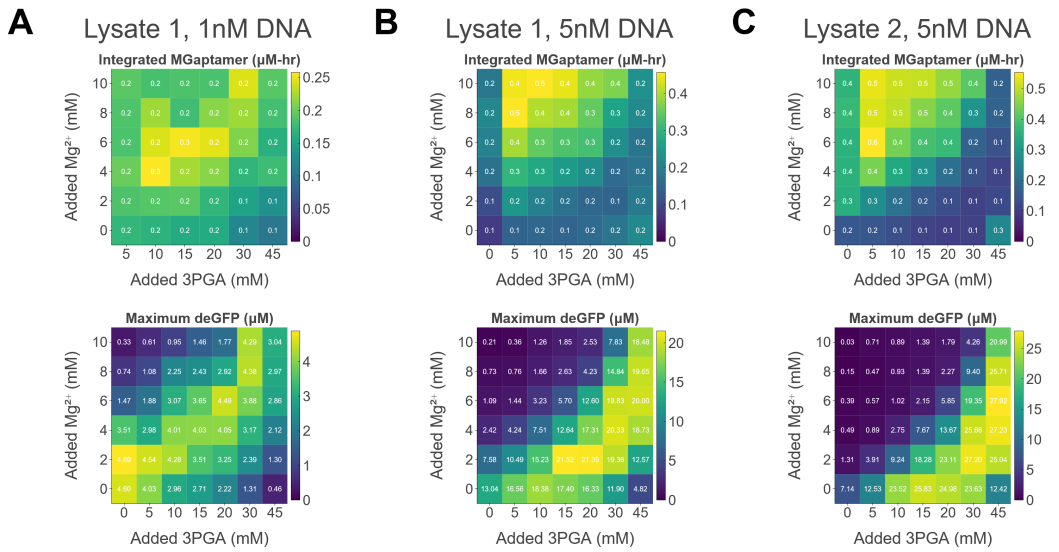

Figure S2.10: Heatmaps of integrated MG aptamer expression and deGFP expression at different Mg^{2+} and 3PGA concentrations at different DNA concentrations. Experiments were performed using (a) Lysate Preparation 1 and 1 nM DNA, (b) Lysate Preparation 1 and 5 nM DNA, (c) Lysate Preparation 2 and 5 nM DNA. Each value is an average of three replicates for that condition. Colorbars were scaled separately for each plot and normalized to a minimum value of zero.

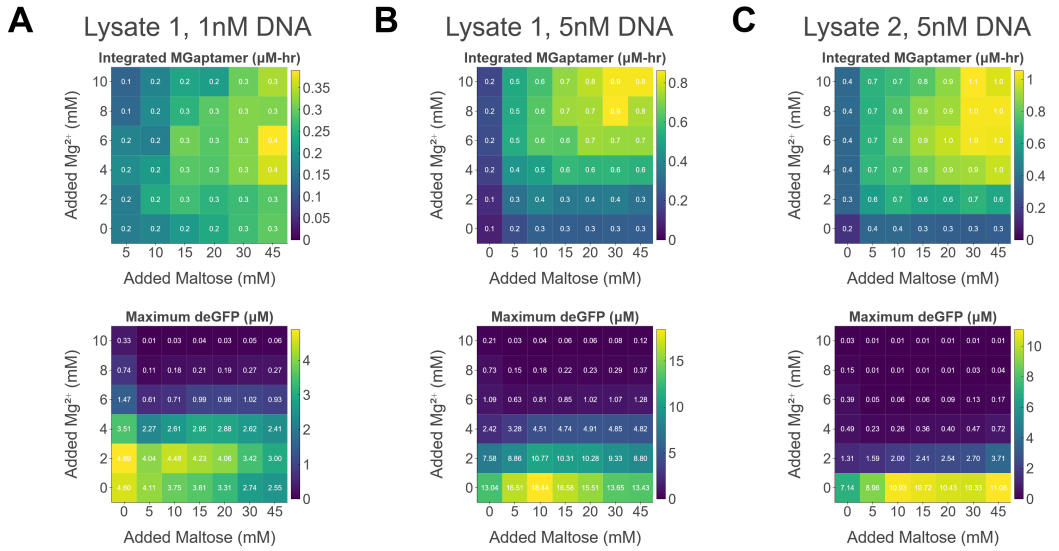

Figure S2.11: Heatmaps of integrated MG aptamer expression and deGFP expression at different Mg^{2+} and maltose concentrations at different DNA concentrations. Experiments were performed using (a) Lysate Preparation 1 and 1 nM DNA, (b) Lysate Preparation 1 and 5 nM DNA, (c) Lysate Preparation 2 and 5 nM DNA. Each value is an average of three replicates for that condition. Colorbars were scaled separately for each plot and normalized to a minimum value of zero.

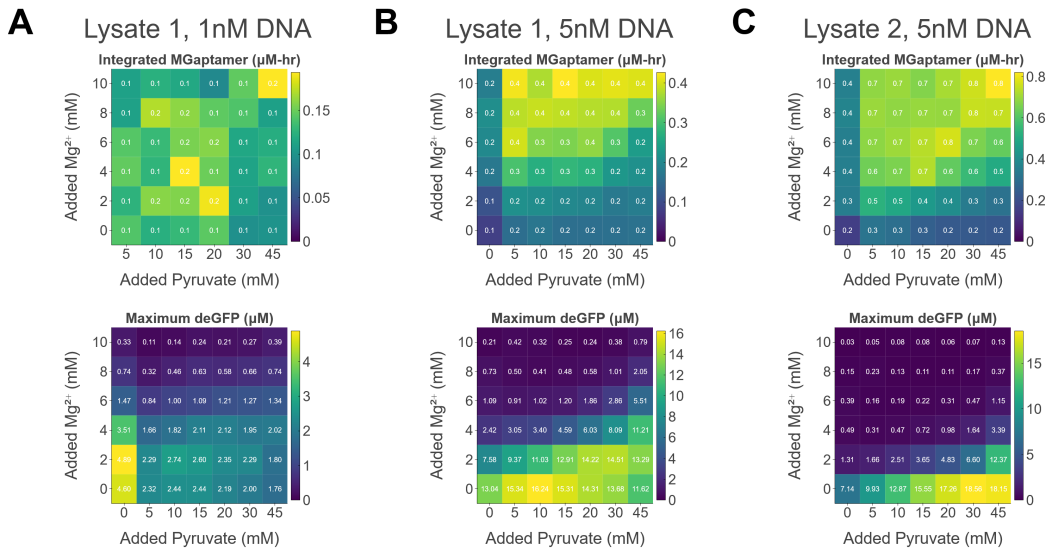

Figure S2.12: Heatmaps of integrated MG aptamer expression and deGFP expression at different Mg^{2+} and pyruvate concentrations at different DNA concentrations. Experiments were performed using (a) Lysate Preparation 1 and 1 nM DNA, (b) Lysate Preparation 1 and 5 nM DNA, (c) Lysate Preparation 2 and 5 nM DNA. Each value is an average of three replicates for that condition. Colorbars were scaled separately for each plot and normalized to a minimum value of zero.

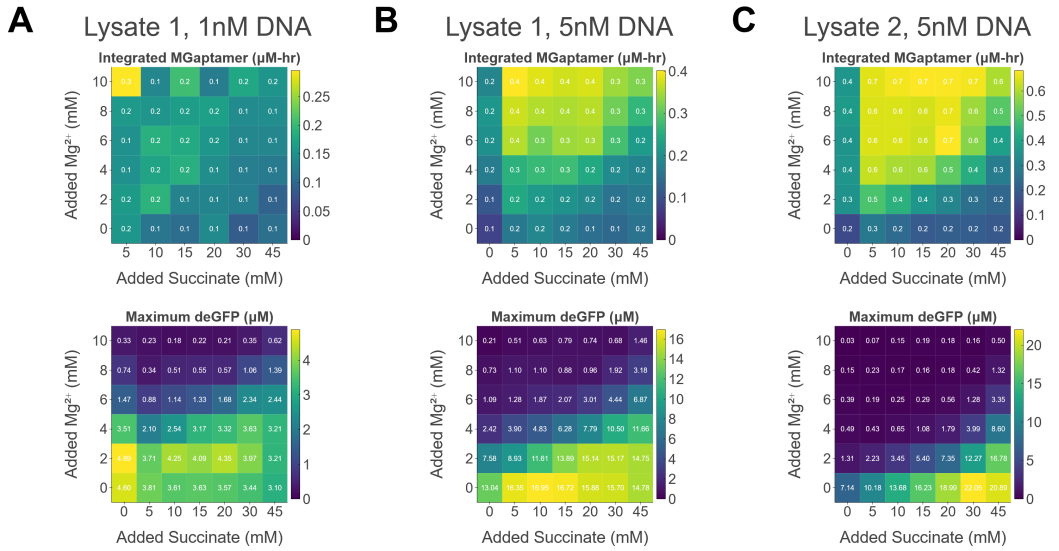

Figure S2.13: Heatmaps of integrated MG aptamer expression and deGFP expression at different Mg^{2+} and succinate concentrations at different DNA concentrations. Experiments were performed using (a) Lysate Preparation 1 and 1 nM DNA, (b) Lysate Preparation 1 and 5 nM DNA, (c) Lysate Preparation 2 and 5 nM DNA. Each value is an average of three replicates for that condition. Colorbars were scaled separately for each plot and normalized to a minimum value of zero.

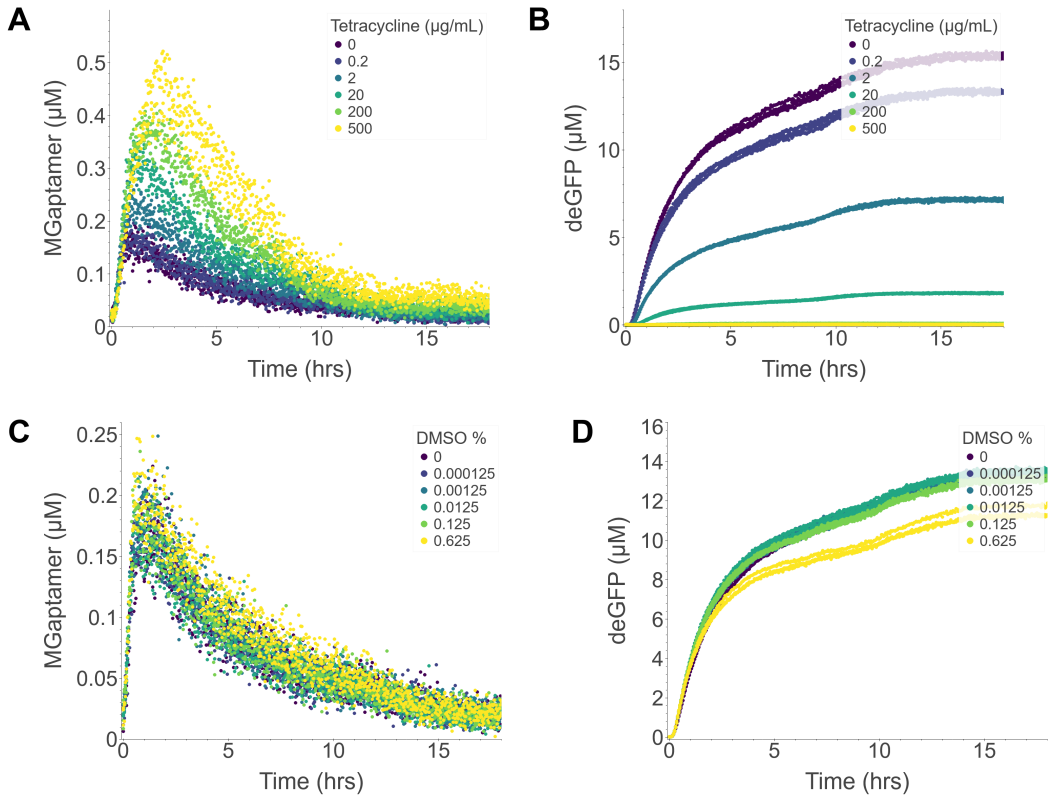

Figure S2.14: Tetracycline titrations. Titrations were performed to determine the concentration of tetracycline necessary for translation inhibition albeit without adding enough DMSO to the reaction to additionally reduce transcription or translation. Controls were performed by adding the equivalent amount of DMSO to make sure the tetracycline alone was impacting translation. (a) and (b) show transcription and translation data, respectively, for TX-TL reactions performed with 200 µg/mL tetracycline. (c) and (d) show transcription and translation data, respectively, for TX-TL reactions performed with the equivalent amount of DMSO for each of the conditions in (a) and (b). TX-TL reactions were performed using the Lysate Preparation 2 with 5 nM DNA at 30 mM 3PGA and 8 mM Mg^{2+}.

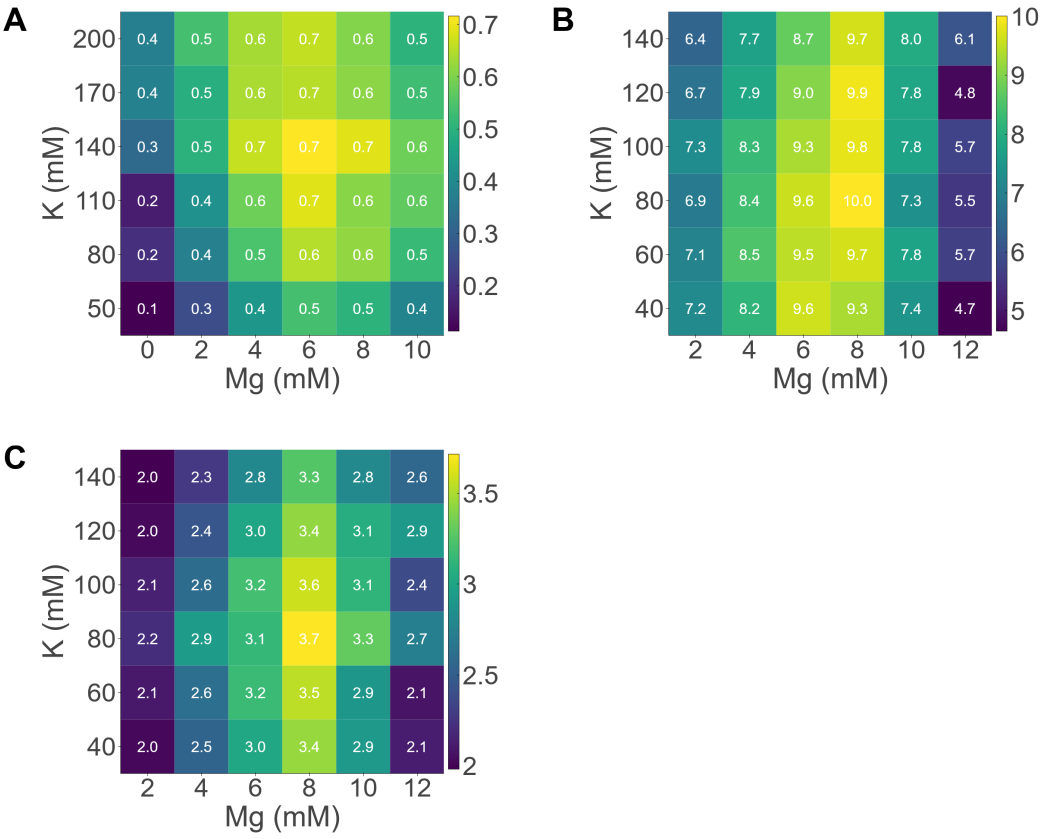

Figure S2.15: Salt calibrations for cell lysate preparations. As each preparation of cell lysate has different optimal Mg^{2+} and K^{+} concentrations, the optimal concentration for each preparation was determined by a salt panel, where TX-TL reactions were performed with the standard formulation, albeit with different pairwise concentrations of Mg-glutamate and K-glutamate. The endpoint deGFP concentration (μM) was recorded after an 18-hour incubation at 29°C for lysate preparations (a) 1, (b) 2, and (c) 3. Colorbars are scaled separately for each plot, and their range spans the minimum and maximum endpoint deGFP value for each experiment.

Additional supporting information

Additional supporting information includes plasmid sequences for most plasmids used in this study (except for the P_{T7}-deGFP-MGapt plasmid) and all data and code used for analysis and figure generation. These are available on GitHub at the following link: https://github.com/mkapasiawala/txtl-tradeoff and on the journal website at the following link: https://pubs.acs.org/doi/10.1021/acssynbio.4c00361. Except for the P_{T7}-deGFP-MGapt plasmid, all plasmids used in this study can be obtained from Addgene using the catalog numbers #227645, #227646, #227647, and #227648.

References

[1] David Garenne et al. "Cell-free gene expression." In: *Nature Reviews Methods Primers* 1.1 (2021), p. 49. ISSN: 2662-8449. DOI: 10.1038/s43586-021-00046-x.

[2] August Brookwell, Javin P. Oza, and Filippo Caschera. "Biotechnology applications of cell-dree expression systems." In: *Life* 11.12 (2021). ISSN: 2075-1729. DOI: 10.3390/life11121367.

[3] Ashty S. Karim et al. "In vitro prototyping and rapid optimization of biosynthetic enzymes for cell design." In: *Nature Chemical Biology* 16.8 (2020), pp. 912–919. ISSN: 1552-4469. DOI: 10.1038/s41589-020-0559-0.

[4] Richard Kelwick et al. "Development of a *Bacillus subtilis* cell-free transcription-translation system for prototyping regulatory elements." In: *Metabolic Engineering* 38 (2016), pp. 370–381. ISSN: 1096-7176. DOI: 10.1016/j.ymben.2016.09.008.

[5] Melissa K. Takahashi et al. "Characterizing and prototyping genetic networks with cell-free transcription–translation reactions." In: *Bacterial and Archaeal Transcription* 86 (2015), pp. 60–72. ISSN: 1046-2023. DOI: 10.1016/j.ymeth.2015.05.020.

[6] Zoe Swank and Sebastian J. Maerkl. "CFPU: a cell-free processing unit for high-throughput, automated in vitro circuit characterization in steady-state conditions." In: *BioDesign Research* 2021 (2021), p. 2968181. ISSN: null. DOI: 10.34133/2021/2968181.

[7] Bastian Vögeli et al. "Cell-free prototyping enables implementation of optimized reverse β-oxidation pathways in heterotrophic and autotrophic bacteria." In: *Nature Communications* 13.1 (2022), p. 3058. ISSN: 2041-1723. DOI: 10.1038/s41467-022-30571-6.

[8] Caitlin E. Sharpes et al. "Assessment of colorimetric reporter enzymes in the PURE System." In: *ACS Synthetic Biology* 10.11 (2021), pp. 3205–3208. DOI: 10.1021/acssynbio.1c00360.

[9] Yan Zhang et al. "Point-of-care analyte quantification and digital readout via lysate-based cell-free biosensors interfaced with personal glucose monitors." In: *ACS Synthetic Biology* 10.11 (2021), pp. 2862–2869. DOI: 10.1021/acssynbio.1c00282.

[10] Peter Q. Nguyen et al. "Wearable materials with embedded synthetic biology sensors for biomolecule detection." In: *Nature Biotechnology* 39.11 (2021), pp. 1366–1374. ISSN: 1546-1696. DOI: 10.1038/s41587-021-00950-3.

[11] Eunhee Cho and Yuan Lu. "Compartmentalizing cell-free systems: toward creating life-like artificial cells and beyond." In: *ACS Synthetic Biology* 9.11 (2020), pp. 2881–2901. DOI: 10.1021/acssynbio.0c00433.

[12] N. Amy Yewdall, Alexander F. Mason, and Jan C. M. van Hest. "The hallmarks of living systems: towards creating artificial cells." In: *Interface Focus* 8.5 (2018), p. 20180023. DOI: 10.1098/rsfs.2018.0023.

[13] Lynn J. Rothschild et al. "Building synthetic cells - from the technology infrastructure to cellular entities." In: *ACS Synthetic Biology* (2024). DOI: 10.1021/acssynbio.3c00724.

[14] Zachary Z. Sun et al. "Protocols for implementing an *Escherichia coli* based TX-TL cell-free expression system for synthetic biology." In: *JoVE* 79 (2013), e50762. ISSN: 1940-087X. DOI: 10.3791/50762.

[15] Nicole E. Gregorio, Max Z. Levine, and Javin P. Oza. "A user's guide to cell-free protein synthesis." eng. In: *Methods and Protocols* 2.1 (2019). ISSN: 2409-9279. DOI: 10.3390/mps2010024.

[16] Yoshihiro Shimizu et al. "Cell-free translation reconstituted with purified components." In: *Nature Biotechnology* 19.8 (2001), pp. 751–755. ISSN: 1546-1696. DOI: 10.1038/90802.

[17] Stephanie D. Cole et al. "Quantification of interlaboratory cell-free protein synthesis variability." In: *ACS Synthetic Biology* 8.9 (2019), pp. 2080–2091. DOI: 10.1021/acssynbio.9b00178.

[18] Katherine A Rhea et al. "Variability in cell-free expression reactions can impact qualitative genetic circuit characterization." In: *Synthetic Biology* 7.1 (2022), ysac011. ISSN: 2397-7000. DOI: 10.1093/synbio/ysac011.

[19] Ankita Roychoudhury. "Understanding the lifetime and rate of protein production in cell-free reactions while maximizing energy use." Undergraduate Thesis. California Institute of Technology, 2021.

[20] Nan Jiang, Xuanwei Ding, and Yuan Lu. "Development of a robust *Escherichia coli*-based cell-free protein synthesis application platform." In: *Biochemical Engineering Journal* 165 (2021), p. 107830. ISSN: 1369-703X. DOI: 10.1016/j.bej.2020.107830.

[21] Tae-Wan Kim, Dong-Myung Kim, and Cha-Yong Choi. "Rapid production of milligram quantities of proteins in a batch cell-free protein synthesis system." In: *Journal of Biotechnology* 124.2 (2006), pp. 373–380. ISSN: 0168-1656. DOI: 10.1016/j.jbiotec.2005.12.030.

[22] Ashty S. Karim et al. "Controlling cell-free metabolism through physiochemical perturbations." In: *Metabolic Engineering* 45 (2018), pp. 86–94. ISSN: 1096-7176. DOI: 10.1016/j.ymben.2017.11.005.

[23] Yiran Wang and Y.H. Percival Zhang. "Cell-free protein synthesis energized by slowly-metabolized maltodextrin." In: *BMC Biotechnology* 9.1 (2009), p. 58. ISSN: 1472-6750. DOI: 10.1186/1472-6750-9-58.

[24] Grace E. Vezeau and Howard M. Salis. "Tuning cell-free composition controls the time delay, dynamics, and productivity of TX-TL expression." In: *ACS Synthetic Biology* 10.10 (2021), pp. 2508–2519. DOI: 10.1021/acssynbio.1c00136.

[25] Alice M. Banks et al. "Key reaction components affect the kinetics and performance robustness of cell-free protein synthesis reactions." In: *Computational and Structural Biotechnology Journal* 20 (2022), pp. 218–229. ISSN: 2001-0370. DOI: 10.1016/j.csbj.2021.12.013.

[26] Angelo C. Batista et al. "Optimising protein synthesis in cell-free systems, a review." In: *Engineering Biology* 5.1 (2021), pp. 10–19. ISSN: 2398-6182. DOI: 10.1049/enb2.12004.

[27] Olivier Borkowski et al. "Large scale active-learning-guided exploration for *in vitro* protein production optimization." In: *Nature Communications* 11.1 (2020), p. 1872. ISSN: 2041-1723. DOI: 10.1038/s41467-020-15798-5.

[28] Vijayalakshmi H. Nagaraj et al. "Translation inhibition and resource balance in the TX-TL cell-free gene expression system." In: *Synthetic Biology* 2.1 (2017), ysx005. ISSN: 2397-7000. DOI: 10.1093/synbio/ysx005.

[29] Filippo Caschera et al. "High-throughput optimization cycle of a cell-free ribosome assembly and protein synthesis system." In: *ACS Synthetic Biology* 7.12 (2018), pp. 2841–2853. DOI: 10.1021/acssynbio.8b00276.

[30] Nicholas Horvath et al. "Toward a genome scale sequence specific dynamic model of cell-free protein synthesis in *Escherichia coli*." In: *Metabolic Engineering Communications* 10 (2020), e00113. ISSN: 2214-0301. DOI: 10.1016/j.mec.2019.e00113.

[31] Michael Vilkhovoy et al. "Sequence specific modeling of *E. coli* cell-free protein synthesis." In: *ACS Synthetic Biology* 7.8 (2018), pp. 1844–1857. DOI: 10.1021/acssynbio.7b00465.

[32] April M. Miguez et al. "Metabolic dynamics in *Escherichia coli*-based cell-free systems." In: *ACS Synthetic Biology* 10.9 (2021), pp. 2252–2265. DOI: 10.1021/acssynbio.1c00167.

[33] William Poole. "Compilation and inference with chemical reaction networks." PhD Thesis. California Institute of Technology, 2021.

[34] Jonathan Garamella et al. "The all *E. coli* TX-TL Toolbox 2.0: a platform for cell-free synthetic biology." In: *ACS Synthetic Biology* 5.4 (2016), pp. 344–355. DOI: 10.1021/acssynbio.5b00296.

[35] Bai-Qing Zhang et al. "Acetylation of translation machinery affected protein translation in *E. coli*." In: *Applied Microbiology and Biotechnology* 104 (2020), pp. 1–13. DOI: 10.1007/s00253-020-10985-2.

[36] Rembrandt J. F. Haft et al. “Correcting direct effects of ethanol on translation and transcription machinery confers ethanol tolerance in bacteria.” In: *Proceedings of the National Academy of Sciences* 111.25 (2014), E2576–E2585. DOI: 10.1073/pnas.1401853111.

[37] Tanya Warnecke and Ryan T. Gill. “Organic acid toxicity, tolerance, and production in *Escherichia coli* biorefining applications.” In: *Microbial Cell Factories* 4.1 (2005), p. 25. ISSN: 1475-2859. DOI: 10.1186/1475-2859-4-25.

[38] Victor Barrenechea et al. “A complementary mechanism of bacterial mRNA translation inhibition by tetracyclines.” In: *Frontiers in Microbiology* 12 (2021). ISSN: 1664-302X. DOI: 10.3389/fmicb.2021.682682.

[39] Charles R. Harris et al. “Array programming with NumPy.” In: *Nature* 585.7825 (2020), pp. 357–362. DOI: 10.1038/s41586-020-2649-2.

[40] Bokeh Development Team. *Bokeh: Python library for interactive visualization.* 2014. URL: http://www.bokeh.pydata.org.

[41] Pauli Virtanen et al. “SciPy 1.0: fundamental algorithms for scientific computing in Python.” In: *Nature Methods* 17 (2020), pp. 261–272. DOI: 10.1038/s41592-019-0686-2.

[42] F. Pedregosa et al. “Scikit-learn: machine learning in Python.” In: *Journal of Machine Learning Research* 12 (2011), pp. 2825–2830.

Chapter 3

FINE-TUNING A METABOLOMICS-INFORMED COARSE-GRAINED MODEL ENABLES FITTING AND PREDICTION OF CELL-FREE PROTEIN EXPRESSION DYNAMICS IN NEW EXPERIMENTAL CONTEXTS

This chapter has been published as part of the pre-print indicated below. M.K.'s contributions to the paper have been reformatted and included here with major edits.

> William Poole, Manisha Kapasiawala, Ankita Roychoudhury, Matthew Haines, Paul Freemont, and Richard M. Murray. "Metabolomics-informed coarse-grained model enables prediction of cell-free protein expression dynamics." In: *bioRxiv* (2025). DOI: 10.1101/2025.06.20.660830.

3.1 Introduction

Synthetic biology harnesses engineering principles and the versatility of biology to enable the manipulation and creation of biological parts and systems. Among its many tools, cell-free systems have emerged as a resourceful tool with diverse applications [1]. The most widespread use of cell-free systems is cell-free protein synthesis (CFPS), where crude cell lysate or purified proteins are supplied with a DNA template and an energy buffer containing building blocks and co-factors for *in vitro* transcription and translation (TX-TL) [2]. Operating outside living cells, CFPS systems offer many advantages, including the ability to produce biomolecules toxic to cell viability and an open reaction environment compatible with lab automation to accelerate design-build-test-learn cycles. These benefits have enabled applications such as biomanufacturing [3]; rapid prototyping of biological parts, pathways, and circuits [4–8]; point-of-care diagnostics and biosensing [9–11]; elucidating the synthesis and assembly of complex biological structures such as membrane proteins and bacteriophages [12–16]; and building synthetic cells [17–19].

Crude cell lysate-based systems remain the most popular type of CFPS systems, although the cellular machinery needed to drive CFPS is increasingly provided in the form of a minimal set of proteins necessary and sufficient for CFPS [20, 21]. Beyond TX-TL machinery, lysate-based systems also contain much of the cytoplasmic content of cells — including metabolic enzymes, organelles like the endoplasmic

reticulum (in eukaryotic lysates), and inverted membrane vesicles — that support processes such as energy regeneration, membrane protein synthesis, and possibly oxidative phosphorylation [22]. While not directly involved in CFPS, these contents enable high expression of a diverse set of proteins, including those that require post-translational modifications, chaperone proteins, and other requirements beyond simple translation. However, while conferring these advantages, this cytoplasmic content also has many unknown and potentially harmful effects on CFPS that lead to poor predictability of CFPS performance. Improving CFPS predictability is crucial for more advanced applications of lysate-based systems, from integrating synthetic cell subsystems to translating *in vitro* learnings into cellular engineering.

Toward improving the predictability of CFPS systems, many previous studies have focused on understanding and modeling the effects of reaction components, particularly small molecules, on CFPS. One study focused on the effects of molecular crowding agents and magnesium (Mg^{2+}) on translation initiation and elongation rates [23]. Another study measured the effects of 20 reaction components on several metrics of CFPS dynamics, including the maximum rate of protein production, the time to reach steady state protein level, and others [24]. A third study focused on characterizing the interactions between CFPS reaction components — specifically, Mg^{2+} and various fuels used to regenerate energy — and their differential effects on total transcription and translation [25]. These studies have provided critical design insights for designing CFPS systems with a desired behavior, but they have not led to improved predictability in systems beyond simple CFPS systems expressing green fluorescent protein (GFP).

Meanwhile, various other studies have focused on creating predictive mathematical models of CFPS [26, 27]. The earliest models varied from small coarse-grained models to complex mechanistic models [28–30], and models that have emerged since then have varied from continuous versus stochastic, ranged from small (<10 reactions) to large (1000+ reactions), and utilized both mass-action kinetics and modeling using ordinary differential equations (ODEs) [26]. Recent models have built on these earlier models and incorporated features like flux balance analysis, metabolic control analysis, resource utilization, and biophysics [26, 31–33]. While these computational efforts have been extremely valuable in providing a breadth of model architectures and approaches, they have focused more on genetic circuit architecture and CFPS machinery (e.g., RNA polymerase, transcription factors, ribosomes, etc.) and less on other proteins with an uncharacterized but substantial

effects on CFPS. Thus, the predictability of these models has been limited to simple GFP-expressing systems or complex biochemical programs in a single environmental context (e.g., a model made for a CFPS system corresponding to a single batch of cell lysate).

Recognizing that CFPS variability is derived largely from the uncharacterized contents of cell lysate, some studies have focused more directly on the interaction between CFPS and cell-free metabolism. Varner and co-workers combined modeling and experiments to create a CFPS model coupled with cell-free metabolism [34, 35]. Using dynamic measurements of nucleotide triphosphates (NTPs), amino acids, and several key metabolites of central carbon metabolism, they were able to construct an ensemble of kinetic models that could predict expression of a reporter protein. Meanwhile, Styczynski and co-workers used metabolomics to characterize and compare central carbon and amino acid metabolism under various reaction conditions, including the absence/presence of CFPS, targeted supplementation of metabolic enzymes, and different methods of cell lysate preparation [36, 37].

While these papers have made important strides towards understanding the relationship between cell-free metabolism and CFPS, this work has focused largely on central carbon, NTP, and amino acid metabolism. The success of cell-free metabolic engineering, which uses innate cell metabolism to generate biochemical intermediates that are then used as precursors for engineered metabolic pathways, suggests that other parts of cell metabolism may be active in cell-free systems [38]. However, the extent to which all metabolic pathways are active in a cell-free context is unknown. Beyond a broad characterization of cell-free metabolism, integrating knowledge of metabolism into predictive models of cell-free protein synthesis, particularly for a wide range of experimental conditions, remains a challenge.

A recent study by Poole and co-workers used untargeted metabolomics to get a high-level view of cell lysate metabolism and found that most *E. coli* metabolic pathways are active in cell lysates, resulting in complex effects on CFPS [39]. These experimental observations were used to motivate a novel coarse-grained mechanistic model of cell lysate metabolism focused on the build-up of metabolic waste products [39]. The model was able to fit experimental data well and capture previously unmodeled experimental phenomena, including reduced protein expression when the addition of DNA to the CFPS reaction was delayed.

In this project, we were interested in exploring the generalizability of the Poole model. In our case, we wondered whether Poole's metabolism model could be read-

ily retrained to fit or even predict protein expression dynamics in new CFPS contexts, including new batches of cell lysate, different experimental initial conditions, and in the presence of complex biochemical interactions.

For our approach, we were encouraged by the recent successes of foundation models in biology, where a base model trained on large amounts of data can be further "fine-tuned" to make it more predictive for a specific application, by retraining the model on a more relevant data set [40–43]. However, foundation models in biology typically consist of deep learning models of millions of parameters trained on large datasets, ranging from hundreds of thousands to millions to billions of data points. These features allow researchers to create highly predictable models at the cost of interpretability and large data sets for training.

Thus, for this work, we were interested in using the Poole model, a small chemical reaction network model whose parameters were previously fit using a large CFPS dataset with Bayesian parameter inference techniques, as a foundation model. Bayesian parameter inference is a statistical method for estimating parameter values for a model — where the value of each parameter is represented as a probability distribution of values — given some experimental data. In recent years, Bayesian inference has been successfully used in estimating parameter distributions for a wide range of models, including chemical reaction network models in biology [44, 45]. Beyond inferring parameter distributions, Bayesian inference has also been used to validate model architectures, choose among various models when model architecture is uncertain, verify properties of models, and create predictive models in spite of parameter uncertainty [46–50].

For our application, we focused on using the Poole model as a foundation model and determining whether the model could be adapted and fine-tuned for use in new experimental contexts using Bayesian inference. We believed that this approach would allow us to conserve and utilize aspects of the model architecture we believed to be true — notably, the effect of cell-free metabolism on CFPS — in addition to parameter values that had previously been estimated by Poole and co-workers. The strategy of using Bayesian inference for model recalibration has been used previously to calibrate CFPS performance between different preparations of CFPS systems, although this approach has only been used to re-fit models rather than modify and adapt model architectures to new contexts [51].

In this work, we first show that the Poole model can be recalibrated to accurately predict protein expression dynamics under novel experimental conditions by fine-

tuning a small subset of its parameters via re-training on smaller condition-specific datasets. We then demonstrate that this approach can be applied to fit and/or predict dynamics under a broad range of new experimental conditions, including various cell lysate batches, DNA concentrations, fuel sources, and more. Finally, we show that the model can be slightly modified to include the effects of Mg^{2+} on CFPS, and that this updated model's prediction recapitulates a previously observed trade-off between energy regeneration and waste mitigation. This work establishes a novel framework for leveraging existing CFPS models in new experimental contexts and provides new predictive insights into the effects of cell-free metabolism on CFPS.

3.2 Results

A fine-tuning strategy for a chemical reaction network parameterized by Bayesian parameter inference

We first sought to determine whether the model architecture of Poole's chemical reaction network, reprinted below, was sufficiently expressive to fit a broad range of protein expression dynamics. Briefly, Poole's CFPS model consists of four reactions. The first reaction is energy regeneration, where fuel F is used to regenerate energy — convert E to E^* — while generating waste W in the process (Equation 3.1). The second reaction is fuel leak, where F is converted to W without regenerating energy (Equation 3.2). The third reaction is energy leak, where energy is consumed — E^* is converted to E — by dissipative processes, such as background metabolic pathways (Equation 3.3). The final reaction is protein expression, where a gene G is transcribed and translated to create protein GFP (Equation 3.4).

$$F + nE \xrightarrow{\rho_{reg}} W + nE^* \quad \rho_{reg}(F, E, W) = V_{reg} \frac{F}{K_F + F} \cdot \frac{E}{K_E + E} \cdot \frac{1}{1 + (W/K_W)^{nw}} \tag{3.1}$$

$$F \xrightarrow{\rho_W^{leak}} W \qquad \rho_W^{leak}(F) = V_W^{leak} \frac{(F/K_F^{leak})^{n_F}}{1 + (F/K_F^{leak})^{n_F}} \tag{3.2}$$

$$E^* \xrightarrow{\rho_E^{leak}} E \qquad \rho_E^{leak}(E^*) = V_E^{leak} \frac{E^*/K_E^{leak}}{1 + E^*/K_E^{leak}} \tag{3.3}$$

$$G \xrightarrow{\rho_{ex}} G + GFP \qquad \rho_{ex}(G, E^*) = V_{ex} G \frac{(E^*/K_E^{ex})^{n_{ex}}}{1 + (E^*/K_E^{ex})^{n_{ex}}} \tag{3.4}$$

In Poole's model, the rate of protein production (in Equation 3.4) depends positively on energy E^*, so the rate of protein increases with increasing energy availability until energy is saturated in the system. Meanwhile, the rate of energy regeneration (in Equation 3.1) depends negatively on waste W, which is generated both during energy

regeneration (Equation 3.1) and fuel leak (Equation 3.2). Thus, as time proceeds and fuel is converted to waste, energy regeneration ceases, and subsequently protein expression ceases.

The model's parameters were originally fit using experimental data of CFPS reactions with different initial conditions using a process known as Bayesian parameter inference. Briefly, Bayesian inference is a statistical methodology that uses Bayes' theorem to estimate the values of parameters in a model. Bayesian inference assumes that each parameter in a model can be described as probability distribution of a given type with appropriate description (e.g., "K_w assumes values according to a uniform distribution bounded by the range (0, 50], n_w assumes values according to a normal distribution with a mean of 5 and standard deviation of 2, etc.").

During Bayesian inference, the likelihood of observing a set of experimental data (given a model) and the probability of a model (parameterized by some best guesses of parameter values, known as "prior distributions") are used to calculate the probability of a set of parameter values given the model and data (an updated set of parameter distributions known as "posterior distributions"). During this iterative process of inference, the parameter space is sampled, the model is simulated, and the error between model prediction and experimental data is calculated, after which the size and direction of the next "step" is calculated and taken in parameter space. Eventually, if the inference problem is well-formed, the samplers (or "walkers") converge to a set of parameter distributions that minimize the error between experimental data and model prediction. Thus, for Bayesian inference to be successful, the following requirements must be met, among others:

1. a model must be capable (in some parameter regime) of capturing a set of experimental data;
2. appropriate prior distributions must be supplied for each parameter;
3. the number steps and walkers must be sufficiently high for the inference to converge to an optimal solution, if one exists at all; and
4. the experimental data must be diverse enough to convey enough information about the system such that model parameters can be informed.

During the original training, all 13 model parameters were inferred by performing Bayesian parameter inference, where inference was split into two runs: one run

with 50 walkers for 5000 steps followed by another run with 100 walkers for 10000 steps. However, as the computational resources required for inference increases with the number of parameters being inferred, we wondered whether it would be possible to utilize the model training Poole and co-workers had already performed and perform "fine-tuning," or re-infer just a few of the model's parameters and keep the remaining parameters at the values Poole had found, rather than re-inferring all parameters from scratch, when adapting the model to new experimental data. We hypothesized that this strategy would allow us to save both computational resources and reduce the amount of data required for training the model.

To perform fine-tuning, we first determined which parameter's values from the original trained model could be kept fixed and which ones should be re-inferred. We hypothesized that we could perform fine-tuning by re-inferring 4 of the 13 total model parameters and fixing the remaining 9 parameters' values to the median value of their posterior distributions. These parameters — V_{ex}, K_E^{ex}, K_W, and n_W — were chosen because they were suspected to most likely be affected by new experimental conditions, such as different fuel sources, cell lysate batches, and promoters. The parameters V_{ex} and K_E^{ex} set the maximum rate of protein production and the energetic requirement of producing the protein, respectively. K_W and n_W determine the extent to which a given fuel's waste negatively affects the rate of energy regeneration. In the case of a modified chemical reaction network, additional parameters resulting from modified or new reaction rates would also be inferred.

Model can be fine-tuned to fit individual time trajectories of new experimental data

Using a previously published data set, we first explored whether the Poole model could be adapted to fit new experimental data, which stems from CFPS systems using various fuel types and concentrations for energy regeneration, different concentrations of Mg^{2+}, multiple cell lysate batches, different promoters for deGFP expression, and different DNA concentrations [25]. We attempted to fit 576 individual time trajectories of deGFP expression by fine-tuning the parameter values for V_{ex}, K_E^{ex}, K_W, and n_W and fixing the remaining 9 parameters' values to the median value of their posterior distributions (Figure 3.1A). After parameter inference, the Mean Absolute Scaled Error (MASE; see **Materials and methods**) was computed to determine, normalize, and compare error values across different experimental data and their corresponding model fits.

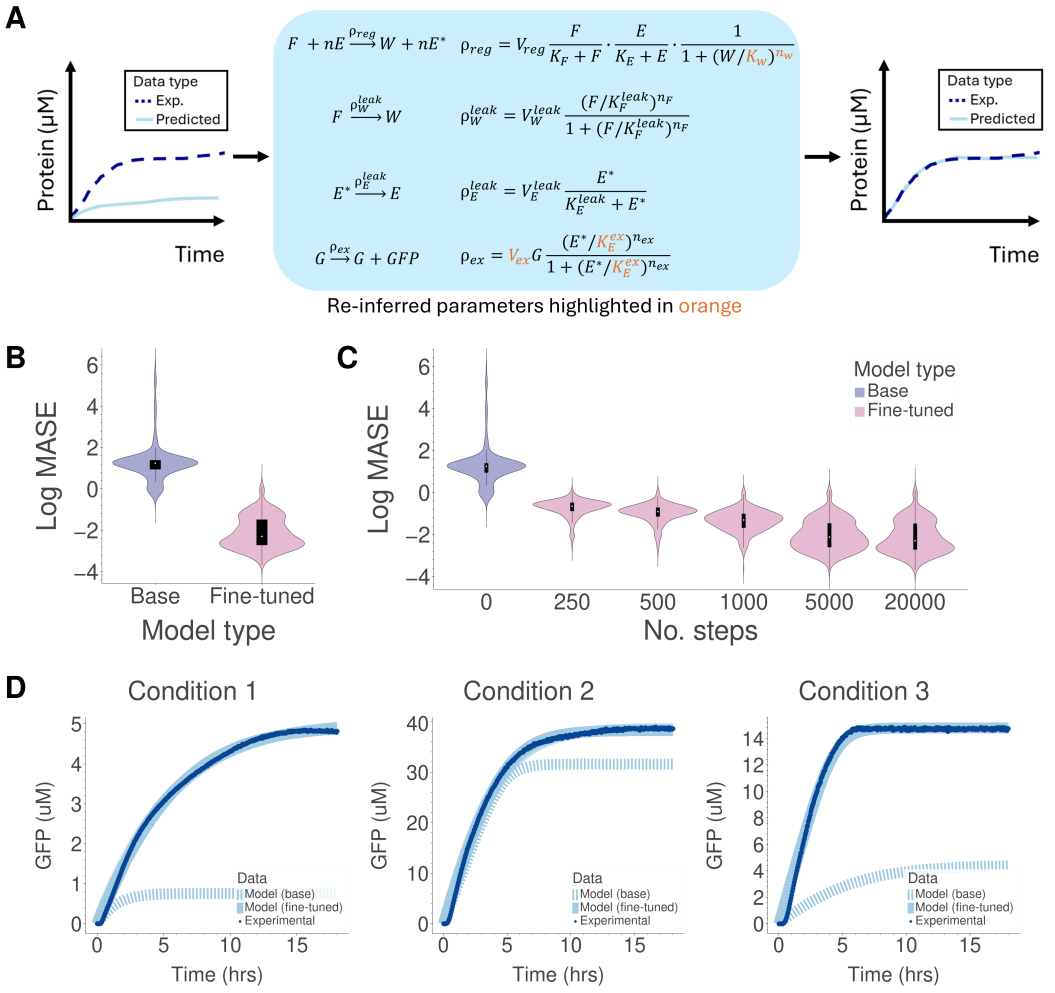

Figure 3.1: Verification of fine-tuning approach for individual experimental conditions. (a) Overview of computational workflow. Four parameters (highlighted in orange) of the already fitted base model were re-inferred to better fit the model to new experimental data. (b) Violin plots of log MASE values before and after fine-tuning the model (aggregated data from the plots shown in Figure 3.2). (c) Violin plots of log MASE values with increasing number of steps taken by walkers during fine-tuning. 0 steps refers to base model, while 20000 steps corresponds the most steps performed during this fine-tuning. The leftmost and rightmost violins are the same as the left and right violins in (b), respectively. (d) Comparison between experimental data and model predictions before and after fine-tuning for three different experimental conditions: Condition 1 (Lysate 1, 30 mM maltose, 4 mM Mg^{2+}, 5 nM DNA with P_{OR1OR2} promoter), Condition 2 (Lysate 2, 30 mM 3PGA, 4 mM Mg^{2+}, 10 nM DNA with P_{OR1OR2} promoter), and Condition 3 (Lysate 3, 20 mM 3PGA, 0 mM Mg^{2+}, 5 nM DNA with P_{T7} promoter).

We found that the fine-tuning approach was very successful; the fine-tuned models better minimized error between model simulations and experimental data, compared to the base model where all parameters were used without further fine-tuning and only the initial conditions of the model were changed to reflect those of the experimental data (Figure 3.1B, 3.2). This simple fine-tuning demonstrated that the metabolism model's architecture was sufficient to capture a broad range of endpoint deGFP concentrations and dynamics (Figure 3.1D), from deGFP expression that rapidly ceased at 5 hours to sustained deGFP expression that continued for 18 hours. Equally importantly, we found that these models could often be fine-tuned in as few as 250 steps and no more than 20000 steps, with model fit increasing as the number of steps was increased (Figure 3.1C). Compared to Bayesian parameter inference of the original model, which took 15000 steps during training, the fine-tuning performed here required comparable or fewer steps (depending on how close of a model fit was desired) and less computational time due to far fewer parameters being inferred.

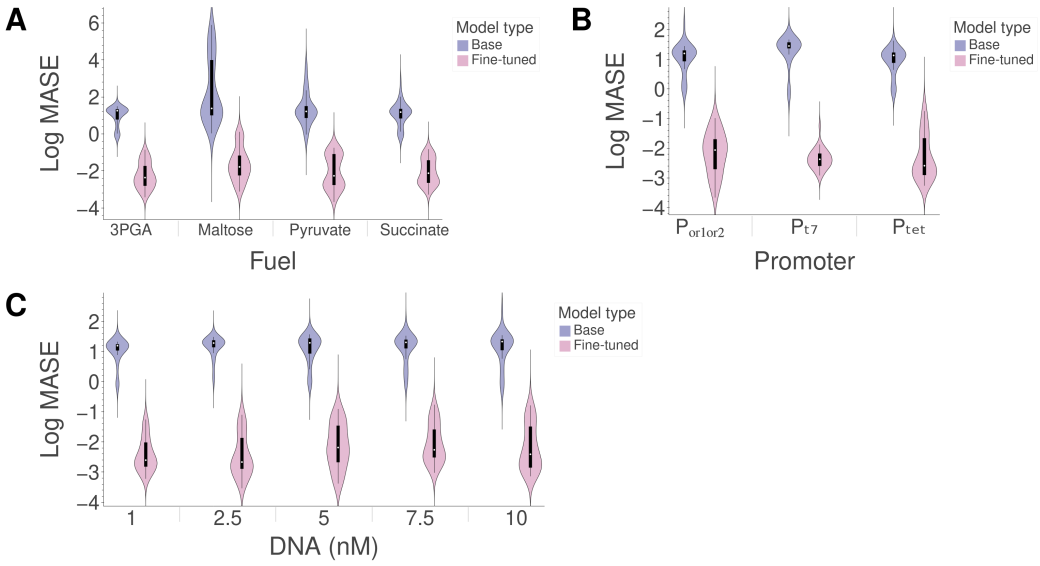

Figure 3.2: Violin plots of log MASE values before and after fine-tuning model. Each of the plots (a), (b), and (c) show data from different experiments. Each violin represents the distribution of the following number of unique experimental conditions: (a) 72 (2 lysate batches x 6 fuel concentration x 6 Mg^{2+} concentrations), (b) 36 (6 fuel concentration x 6 Mg^{2+} concentrations), and (c) 36 (6 fuel concentration x 6 Mg^{2+} concentrations).

Model can be adapted and fine-tuned to fit and predict multiple time trajectories of new experimental data

We next explored whether the fine-tuning approach could be extended to a model that was slightly different from the one it was originally trained on. In the previously published data we used [25], we noticed a DNA saturation effect in CFPS systems, such that after a certain concentration of DNA, deGFP endpoint yields would not change with increasing DNA concentration. Furthermore, in some systems, additional DNA resulted in reduced deGFP yields, perhaps due to a resource competition between transcription and translation. Both of these phenomena seemed to depend heavily on the particular Mg^{2+} and 3PGA concentrations used for the set of experiments. Our original CFPS model did not account for this effect, so we wondered if the fine-tuning approach could be used as before, albeit with (1) a new reaction propensity for deGFP expression and (2) when trying to fit multiple time trajectories instead of a single time trajectory (Figure 3.3A).

For this new fine-tuning workflow, we first created a new model where we kept Equations 3.1-3.3 the same and modified the reaction rate in Equation 3.4. The updated reaction rate for the $G \xrightarrow{\rho_{ex}} G + GFP$ reaction was as shown below:

$$\rho_{ex}(G, E^*) = V_{ex} \frac{(G/K_{min})^{n_{min}}}{1 + (G/K_{min})^{n_{min}}} \cdot \frac{1}{1 + (G/K_{max})^{n_{max}}} \cdot \frac{(E^*/K_E^{ex})^{n_{ex}}}{1 + (E^*/K_E^{ex})^{n_{ex}}} \quad (3.5)$$

In this new reaction rate, the dependence of protein expression on DNA concentration was much like a bandpass filter, where either too much or too little DNA would result in no protein expression and where protein expression was optimized over a range of DNA concentrations. In this new reaction rate, K_{min} and n_{min} determine the minimum amount of DNA necessary for protein expression and the range over which increasing DNA concentration would increase protein expression. Likewise, K_{max} and n_{max} determine the amount of DNA over which protein expression ceases and the range over which increasing DNA concentration would decrease protein expression.

Next, we re-inferred the same 4 parameters as before — V_{ex}, K_E^{ex}, K_W, and n_W — and newly inferred 4 more parameters resulting from the new reaction propensity — K_{min}, K_{max}, K_{max}, and n_{max}. Finally, unlike before, where the fine-tuning was performed separately for each unique time trajectory corresponding to a unique experimental condition, we provided 5 time trajectories of deGFP expression corresponding to 5 different DNA concentrations. We performed 36 different fine-tuning

cases resulting from 36 combinations of Mg^{2+} and 3PGA concentrations (where all other variables were kept the same).

As before, we found that the fine-tuning approach was successful; the fine-tuned models better minimized error between model simulations and experimental data compared to the base model (Figure 3.3B,C). The fine-tuned models were successful at fitting a broad range of deGFP concentrations and dynamics (Figures 3.3B, 3.4) as well as capturing nonintuitive trends, such as deGFP expression being maximized at a DNA concentration that was not the highest used for that experiment (Figure 3.3B, Condition 3). The experimental conditions where the fine-tuning did not work well corresponded to experiments with initial conditions of low 3PGA and high Mg^{2+} concentrations, which resulted in biphasic protein expression that the model was not capable of capturing (Figure 3.4). Even in the presence of unusual dynamics, however, the model often succeeded at matching the endpoint deGFP yields obtained for different initial concentrations of DNA (Figure 3.4).

The experimental mechanism behind biphasic protein expression remains uncertain, but one possible hypothesis is that Mg^{2+} inhibits some crucial CFPS machinery (e.g., energy-regenerating enzyme phosphoglycerate kinase, ribosomes, etc.), and that a downstream byproduct of 3PGA metabolism binds to Mg^{2+} and "rescues" CFPS. Another hypothesis is that Mg^{2+} first binds to a product immediately downstream of 3PGA metabolism (e.g., ATP), and that this complex then inhibits CFPS machinery until a metabolism product further downstream then binds to Mg^{2+} and "rescues" CFPS; both hypotheses are weakly supported by existing experimental evidence [52]. Although we did not focus on biphasic protein expression in this work, future work could explore whether a more complex CFPS model could model this phenomenon and improve the fits of protein expression curves at low 3PGA and high Mg^{2+} concentrations.

To determine whether the model could not only fit data but also predict unseen data, we next explored fine-tuning where the same experimental data was split into training and test sets. Here, the fine-tuning was performed on training data only, after which the test data was compared to model predictions for those experimental conditions. Due to the reaction propensity of the protein expression reaction in Equation 3.5, however, we could not simply randomize the assignment of data into training and test sets. As mentioned above, deGFP yields first increased, then decreased, with increasing DNA concentration in a CFPS system, with the relationship between endpoint deGFP yields and initial DNA concentration resembling the shape of

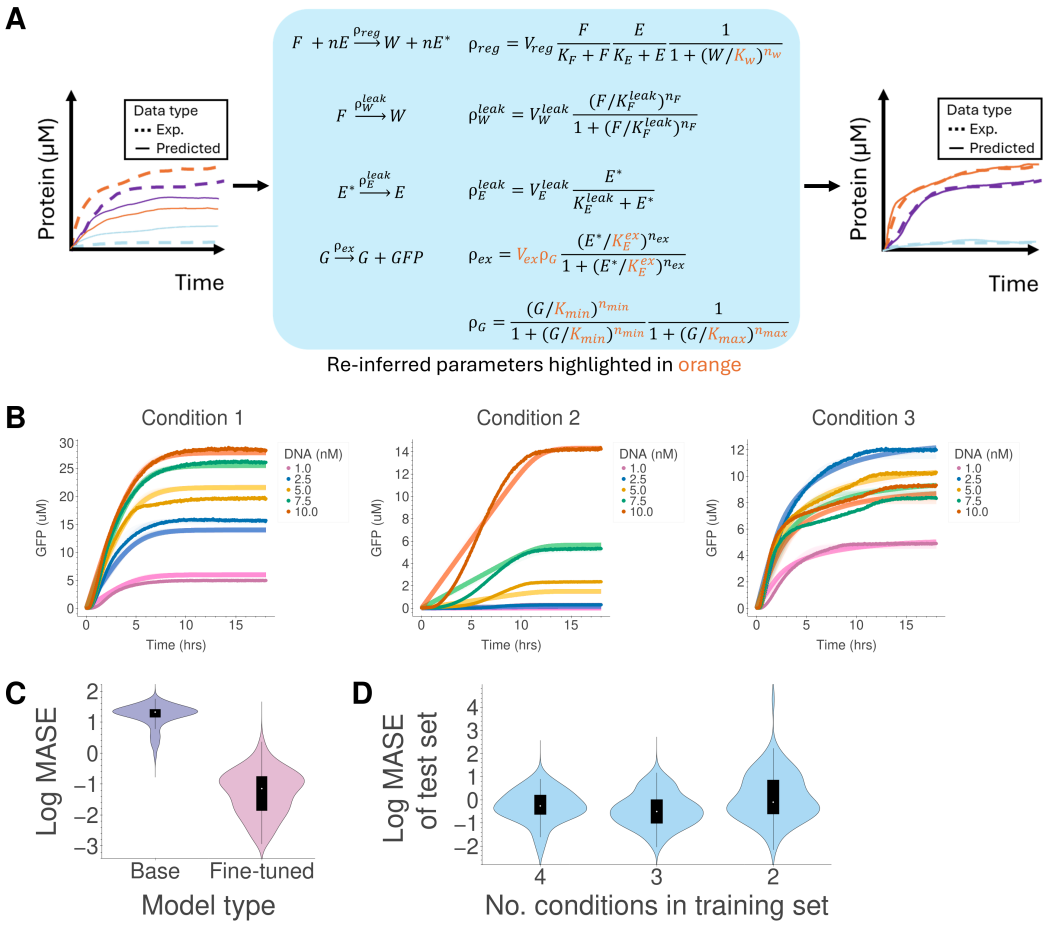

Figure 3.3: Fine-tuning a model with a modified reaction propensity. (a) Overview of computational workflow. Four parameters (highlighted in orange) of the already fitted base model were re-inferred and 4 parameters were newly inferred to better fit the model to new experimental data. Multiple time trajectories corresponding to various [DNA] for a given set of [3PGA] and [Mg^{2+}] were provided for the fine-tuning. (b) Comparison of experimental data (dark points, average of 3 replicates) and model predictions (solid lines) after fine-tuning for 3 different experimental conditions: 5 mM 3PGA and 0 mM Mg^{2+} (Condition 1), 45 mM 3PGA and 0 mM Mg^{2+} (Condition 2), and 20 mM 3PGA and 6 mM Mg^{2+} (Condition 3). (c) Violin plots of log MASE values (see Methods) before and after fine-tuning the model on new data. Each violin represents a distribution of 180 MASE values (5 [DNA] x 6 [3PGA] x 6 [Mg^{2+}]). For each of 36 fine-tuning cases, all 5 time trajectories' data (corresponding to DNA concentrations of 1 nM, 2.5 nM, 5 nM, 7.5 nM, and 10 nM for a particular set of [3PGA] and [Mg^{2+}]) were provided as both training data and test data. (d) The violins correspond to MASE values where the training and test data were split. For each violin, data corresponding to the following [DNA] was used for the test set (and withheld in the training set) for each set of 3PGA and Mg^{2+} concentrations: 5 nM DNA (left violin); 2.5 nM DNA and 7.5 nM DNA (middle violin); and 2.5 nM, 5 nM, and 7.5 nM DNA (right violin).

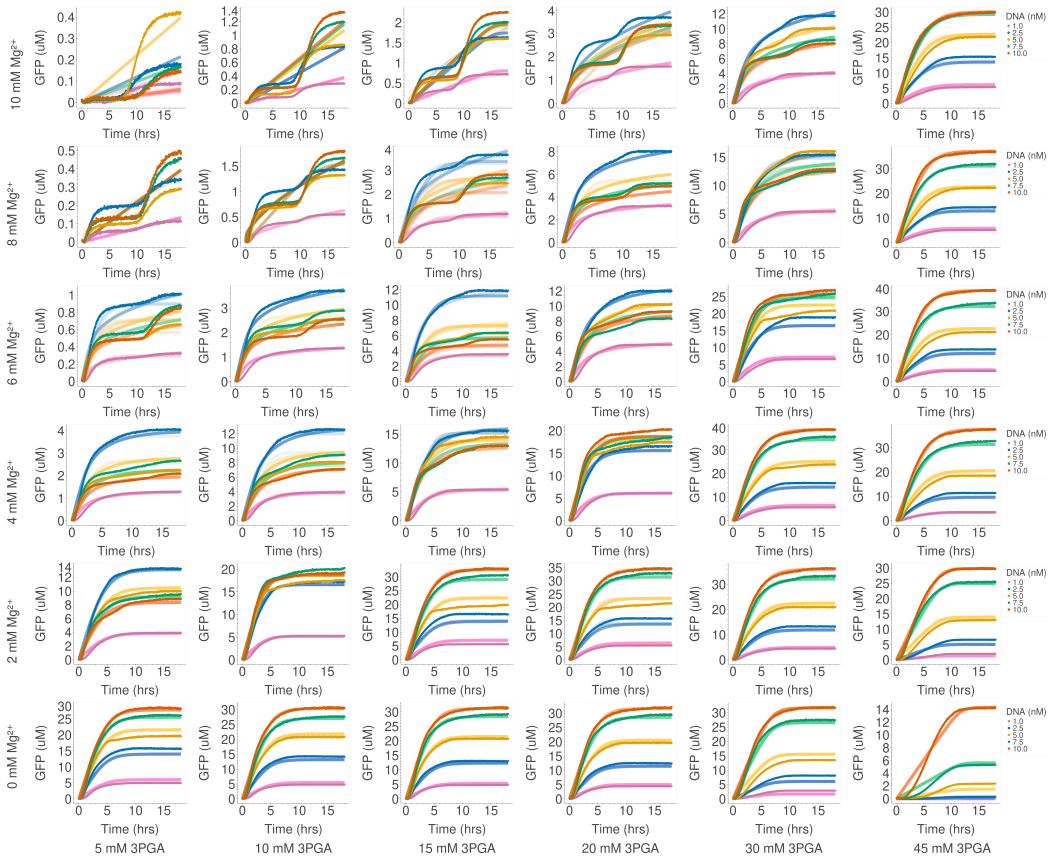

Figure 3.4: Comparison of model prediction and experimental data after fine-tuning as shown in Figure 3.3 and using training data as test data. For each of 36 fine-tuning cases, all 5 time trajectories' data (corresponding to DNA concentrations of 1 nM, 2.5 nM, 5 nM, 7.5 nM, and 10 nM for a particular set of 3PGA and Mg^{2+} concentrations) were provided as training data and as test data. Darker points are experimental data; lighter lines of the same color are model predictions.

a bandpass filter. Thus, providing concentrations on the ends of the range of concentrations used (i.e., 1 nM and 10 nM DNA) was necessary to ensure the shape of the function could be maintained.

Thus, we split the data into training and test sets in the following manner. For each fine-tuning case, we first reserved the time-course deGFP dynamics corresponding to 5 nM DNA for the test set, and used the remaining 4 DNA concentrations' data (1 nM, 2.5 nM, 7.5 nM, and 10 nM) for the training data used during fine-tuning. We next repeated this procedure, albeit using data corresponding to 2.5 nM and 7.5 nM DNA for the test set, and using the remaining 3 DNA concentrations' data (1 nM, 5 nM, and 10 nM DNA) for the training set. Finally, we repeated this procedure again, albeit using the data corresponding to 2.5 nM, 5 nM, and 7.5 nM DNA for the test

set, and using the remaining 2 DNA concentrations' data (1 nM and 10 nM DNA) for the training set. The error between model prediction and experimental data for the test sets are shown in Figure 3.3D (see Figure S3.1 for comparison between Figure 3.3C and Figure 3.3D).

We found that fine-tuned models were generally successfully at capturing the shapes of the deGFP time-course dynamics, although they often struggled to recapitulate the exact concentrations achieved experimentally (Figure S3.2-S3.4, compared to Figure 3.4). This issue was exacerbated, as expected, when less data was provided in the training set. It is worth noting that the fine-tuned models were surprisingly successful at qualitatively predicting some phenomena, including no deGFP expression in a TX-TL system with 2.5 nM DNA (Figure S3.3, at 45 mM 3PGA and 0 mM Mg^{2+}), relatively high deGFP expression with a different TX-TL system with 2.5 nM DNA compared to other DNA concentrations (Figure S3.3, at 5 mM 3PGA and 2 mM Mg^{2+}), and comparable deGFP expression in systems with 7.5 nM and 10 nM DNA (Figure S3.4, at 45 mM 3PGA and 10 mM Mg^{2+}).

Adapted and fine-tuned model can be used to gain novel experimental insights
Having confirmed that the fine-tuning approach was successful at fitting and predicting deGFP protein expression dynamics, we next wondered whether the fine-tuning approach could be used to gain experimental insights in a novel experimental system. The study whose data we were using for fine-tuning had found a compensatory interaction between Mg^{2+} and 3PGA in CFPS systems, where too much of either component reduced protein yields, but enough of both was sufficient to revive protein expression [25]. We wondered if our model could be adapted and our fine-tuning approach applied to qualitatively model and explore causes for this phenomenon.

For this new fine-tuning workflow, we first created a new model where we kept Equations 3.1-3.3 the same and modified the reaction rate in Equation 3.4. The updated reaction rate for the $G \xrightarrow{\rho_{ex}} G + GFP$ reaction was as shown below:

$$\rho_{ex}(G, E^*) = V_{ex} \frac{(E^*/K_E^{ex})^{n_{ex}}}{1 + (E^*/K_E^{ex})^{n_{ex}}} \cdot \frac{1}{1 + (B/K_B)^{n_B}} \tag{3.6}$$

We also added an additional reversible reaction, shown below as two separate reactions:

$$B + 4W \xrightarrow{\rho_{W,F}^{chel}} X \qquad \rho_{W,F}^{chel}(B, W) = V_{W,F}^{chel} B W^4 \tag{3.7}$$

$$X \xrightarrow{\rho_{W,R}^{chel}} B + 4W \qquad \rho_{W,F}^{chel}(X) = V_{R,F}^{chel} X \tag{3.8}$$

In this new model, consisting of Equations 3.1-3.3 and 3.6-3.8, Mg^{2+} was added as a new species B. We also modified our protein expression reaction to account for the inhibitory effects of Mg^{2+} on deGFP expression, and added a reversible reaction for binding of Mg^{2+} to waste in the model (Figure 3.5A). The binding ratio of one molecule of Mg^{2+} to four waste molecules was chosen based on a visual inspection of the experimental data; other binding ratios were tried but resulted in worse model fits.

Next, we re-inferred the same 4 parameters as in Figure 3.1 — V_{ex}, K_E^{ex}, K_W, and n_W — and newly inferred 4 more parameters resulting from the new reaction propensity and new reactions added to the model —K_B, n_B, $V_{W,F}^{chel}$, and $V_{W,R}^{chel}$ (Figure 3.5A). Unlike the previous fine-tuning case, however, where we fine-tuned separately for small sets of experimental data, for each of two fine-tuning cases, we provided 36 time trajectories of deGFP expression corresponding to 6 different 3PGA concentrations and 6 different Mg^{2+} concentrations, where other conditions were kept the same.

We found that while our fine-tuning approach did not do well quantitatively, it captured the experimentally observed deGFP dynamics qualitatively at low 3PGA concentrations (Figures S3.5, S3.6). The model also captured the same general endpoint trends in deGFP yields as observed experimentally (Figure 3.5B,C) in the previously published study [25].

By modeling species not measured experimentally, we were also able to glean some new experimental insights. First, we noticed that the two batches of cell lysate, whose deGFP dynamics were used to parameterize the model separately during their respective fine-tunings, metabolized fuel at different rates, with Lysate Batch 2 metabolizing fuel slower and generating waste slower than Lysate Batch 1 (Figures S3.7, S3.8). Meanwhile, however, energy concentrations were consistent across the two batches of lysate. This seemed to suggest that the higher deGFP yields observed in Lysate Batch 2 were due to lower waste generation rather than improved energy regeneration, which is consistent with our original hypothesis that waste generation limits protein expression to a greater extent than energy regeneration.

Second, our model simulations also suggested the Mg^{2+}-W binding reaction had a fast reaction rate (Figures S3.7, S3.8). This is consistent with a previous paper that found that Mg^{2+} had to be repeatedly titrated into a CFPS reaction, rather than added in a high amount all at once, to improve protein expression yields, since adding too much Mg^{2+} at once inhibited protein expression [53]. Finally, the model

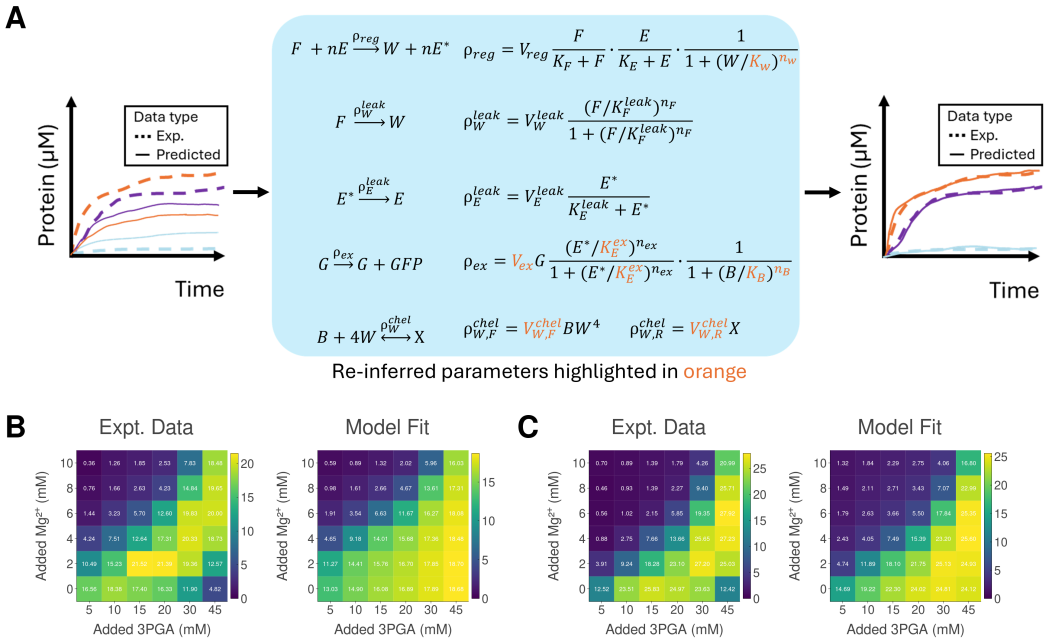

Figure 3.5: Fine-tuning a model with an additional reaction. (a) Overview of computational workflow. Four parameters of the already fitted base model — V_{ex}, K_E^{ex}, K_W, and n_W — were re-inferred and four parameters — K_B, n_B, $V_{W,F}^{chel}$, and $V_{W,R}^{chel}$ — were newly inferred to better fit the model to new experimental data. 36 deGFP time trajectories corresponding to 36 sets of 3PGA and Mg^{2+} concentrations were provided for the fine-tuning for each of the two fine-tuning cases. (b) and (c) show endpoint deGFP comparisons between experimental data and model fit after fine-tuning for Lysate Batches 1 and 2 from the experimental data previously published [25].

simulations suggested that adding additional fuel above 15-20 mM 3PGA to a CFPS reaction does not appreciably increase the concentration of energy available in the system (Figures S3.7, S3.8). This is consistent with the data shown in Figure 5.2 of the work by Poole and co-workers [39], where they also found that the addition of 3PGA to a CFPS system with 30 mM 3PGA did not improve deGFP yields, and with a previous paper that suggested that most of the energy regenerated during CFPS is diverted towards metabolic pathways competing with CFPS for energy [25].

3.3 Discussion

Building accurate and generalizable CFPS models that can be readily trained with an easily obtained experimental dataset is an essential step towards predicting the performance of more complex cell-free biomolecular programs, especially when the combinatorial search space of experimental regimes is too large to be traversed.

Many existing CFPS models are difficult to parameterize and/or adapt to new experimental contexts, which is a challenge for engineering efforts aimed at combining or expanding existing biomolecular programs.

Our approach demonstrates a novel modeling strategy where we fine-tuned an existing coarse-grained metabolism model to fit and predict new protein expression in new experimental contexts. This methodology is similar to the approach taken in a previous work where parameter non-identifiability was exploited in order to correct for batch effects in cell lysates [51]. Our approach is also inspired by modern machine learning methods; foundation models, both in biological applications and more broadly, typically consist of a deep learning model trained on large data sets which are then frequently fine-tuned on more specialized datasets in order to perform specific tasks [40–43]. In biology, these large data sets can include omics data (transcriptomics, genomics, metabolomics, etc.), language data (from the Internet and other sources), and even images.

We have adapted this approach to use an interpretable mechanistic model fit to a carefully constructed panel of CFPS time-coarse data and then fine-tuned to model various CFPS conditions. As our models are simple and mechanistic, we can use our model to provide experimental insights in addition to predictability, a capability not typically possible with "black box" deep learning models. In the example shown in Figure 3.3, we show that model can be readily adapted to fit and predict protein expression dynamics previously unseen in the original training data. In the example shown in Figure 3.5, we show that this model can additionally be used to gain experimental insights into cell-free metabolism and guide future experimental efforts aimed at characterizing and improving cell-free metabolism to benefit CFPS.

While addressing a critical gap in the field, our work raises some interesting questions. First, how exactly does the fine-tuning approach work "under the hood," as in how do the prior distributions of parameters (supplied by the Poole model) affect the posterior distributions of parameters obtained after the fine-tuning? One possibility is that the prior distributions provide a good starting point for fine-tuning, so that parameters for a new experimental context are in the close vicinity of the old parameters and can be easily found. Another possibility is that the prior distributions are sufficiently broad, so that parameters for a new experimental context are found in a subregion of that broad parameter space. As multiple parameters are being inferred during the fine-tuning, it is also possible that a combination of these scenarios is true. Future work — both theoretical and computational — aimed at

investigating the relationship between the Poole model's posterior distributions and the fine-tuned models' posterior distributions can help shed insight on whether the fine-tuning approach is always effective, and if not, highlight the failure modes of the fine-tuning approach.

This work also raises another question: how effective will the fine-tuning approach actually be for creating predictive models of more complex biomolecular programs? This work has demonstrated the first few steps towards answering that question — demonstrating that the metabolism model is sufficiently expressive and readily adaptable — but, just like the work by Poole and co-workers, focuses exclusively on the constitutive expression of a single fluorescent molecule, deGFP. We suspect that building a model based on Poole's metabolism model with subsequent fine-tuning will be a better approach than using existing CFPS models, due to the ease of fine-tuning and the addition of the effects of metabolism on CFPS. However, this does not necessarily mean the approach will be sufficient for adapting the model in more complex scenarios; for example, additional parameters may need to be fine-tuned to more accurately capture the effects of metabolism on CFPS. Future work aimed at exploring how well our approach works for more complex biomolecular programs should help shed insight on the generalizability of our approach.

By providing computational frameworks that can be used to model protein expression dynamics in the presence of metabolic complexity, this work provides a new tool for understanding the interplay between cell-free metabolism and CFPS. Ultimately, this work forms a solid step towards improving the predictability of CFPS systems, which will be necessary for future cell-free applications aimed at building complex systems, from multi-layered biological circuits to synthetic biological cells.

3.4 Materials and methods

Model recalibration

Fine-tuning was performed by first creating a model parameterized by the mean values of parameters of the top 100 parameter sets (as measured by parameter sets that resulted in the lowest error between model simulation and experimental data) from the posterior distribution of the Bayesian inference performed on the data shown in Figure 5.2 in the work by Poole and co-workers [39]. Next, any modifications to model propensities or new reactions were added to the model where applicable, with parameters for those additions hand-tuned to give the model a good starting point. Finally, the indicated parameters were then inferred/re-

inferred by performing Bayesian inference with 100 walkers and a variable number of steps: 20000 steps for the fine-tuning described in Figure 3.1, 50000 steps for the fine-tuning described in Figure 3.3, and 50000 steps for the fine-tuning described in Figure 3.5. As in the case of the original model, models were produced using BioCRNpyler [54], saved as SBML files [55], and then loaded into Bioscrape [56] for inference. Bayesian parameter inference was performed on Caltech's Resnick High-Performance Computing (HPC) cluster using 24 cores and 4 GiB RAM/core. All code is available on GitHub at the following link:

https://github.com/mkapasiawala/cellfree_metabolomics_modeling_finetuning.

Mean Average Scaled Error (MASE) plots

For figures where a MASE value was computed, the following approach was used. First, for each unique experimental condition, the model was simulated using the same initial conditions of model species (fuel (F), DNA (G), and NTP (E) concentrations) as those used in the experiment. Next, the percentage error between experimental data (averaged over 3 replicates) and model prediction was computed at each timepoint. Next, the mean value of these errors was computed to create a single MASE value. Finally, the distribution of MASE values corresponding to a given set of experimental conditions/data was displayed using a violin plot.

Acknowledgments

We note that this work builds on preliminary results from W. Poole's thesis [39]. We thank William Poole for providing critical feedback that helped shape this project. Research was supported by the Army Research Office under Cooperative Agreement Number W911NF-22-2-0210 and Air Force Office of Scientific Research (AFOSR) under MURI grant FA9550-22-1-0316. The views and conclusions contained in this document are those of the authors and should not be interpreted as representing the official policies, either expressed or implied, of the Army Research Office or the U.S. Government. The U.S. Government is authorized to reproduce and distribute reprints for Government purposes notwithstanding any copyright notation herein.

3.5 Supporting information

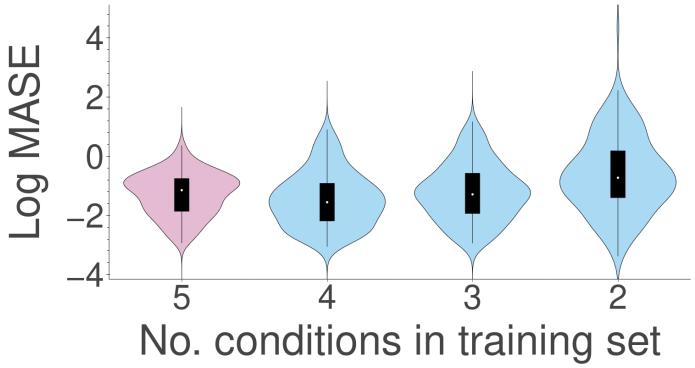

Figure S3.1: Violin plots of log MASE values corresponding to fine-tuning model shown in Figure 3.3a on differentially sized training/test sets. The pink (left) violin corresponds to MASE values of all 180 experimental conditions (5 DNA concentrations x 6 3PGA concentrations x 6 Mg^{2+} concentrations); for each of 36 fine-tuning cases, all 5 time trajectories' data (corresponding to DNA concentrations of 1 nM, 2.5 nM, 5 nM, 7.5 nM, and 10 nM for a particular set of 3PGA and Mg^{2+} concentrations) were provided as training data and as test data. The pink violin is the same as shown in Figure 3.3b. The blue violins correspond to MASE values where the training and test data were split. In the second violin, for each of the 36 fine-tunings, data corresponding to DNA concentrations of 1 nM, 2.5 nM, 7.5 nM, and 10 nM were provided as training data, and the data corresponding to 5 nM DNA for the same set of 3PGA and Mg^{2+} concentrations were provided as test data. Likewise, in the third violin, for each of the 36 fine-tunings, data corresponding to DNA concentrations of 1 nM, 5 nM, and 10 nM were provided as training data, and the data corresponding to 2.5 nM DNA and 7.5 nM DNA for the same set of 3PGA and Mg^{2+} concentrations were provided as test data. Finally, in the last violin, for each of the 36 fine-tunings, data corresponding to DNA concentrations of 1 nM and 10 nM were provided as training data, and the data corresponding to 2.5 nM DNA, 5 nM DNA, and 7.5 nM DNA for the same set of 3PGA and Mg^{2+} concentrations were provided as test data.

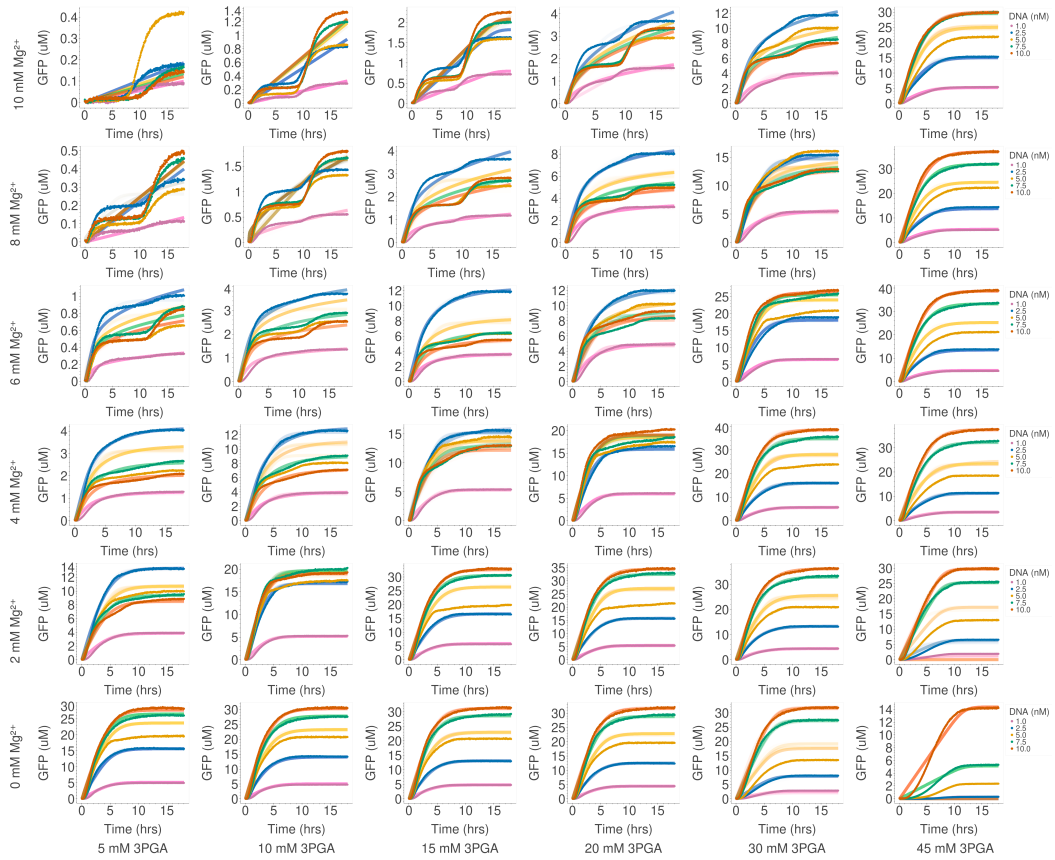

Figure S3.2: Comparison of model prediction and experimental data after fine-tuning as shown in Figure 3.3 and using 4 time trajectories as training data. For each of the 36 fine-tunings, data corresponding to DNA concentrations of 1 nM, 2.5 nM, 7.5 nM, and 10 nM were provided as training data, and the data corresponding to 5 nM DNA for the same set of 3PGA and Mg^{2+} concentrations were provided as test data (yellow lines). Darker points are experimental data; lighter lines of the same color are model predictions.

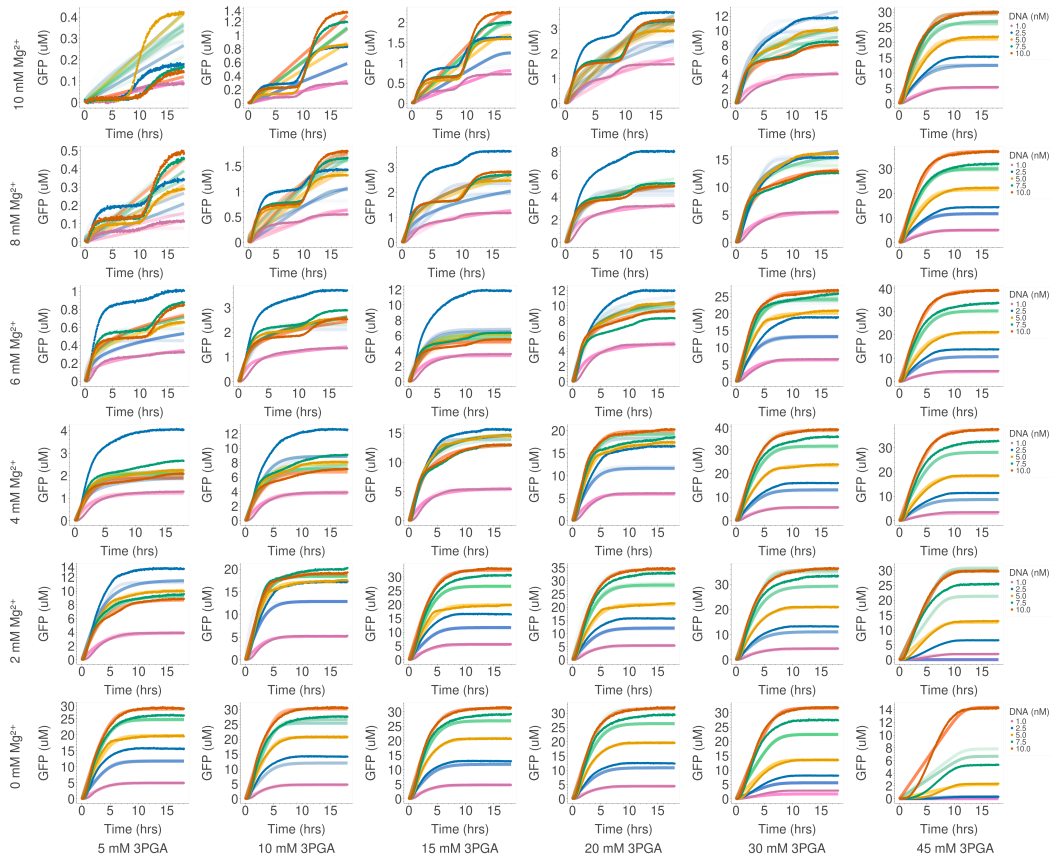

Figure S3.3: Comparison of model prediction and experimental data after fine-tuning as shown in Figure 3.3 and using 3 time trajectories as training data. For each of the 36 fine-tunings, data corresponding to DNA concentrations of 1 nM, 5 nM, and 10 nM were provided as training data, and the data corresponding to 2.5 nM DNA and 7.5 nM DNA for the same set of 3PGA and Mg^{2+} concentrations were provided as test data (green and blue lines). Darker points are experimental data; lighter lines of the same color are model predictions.

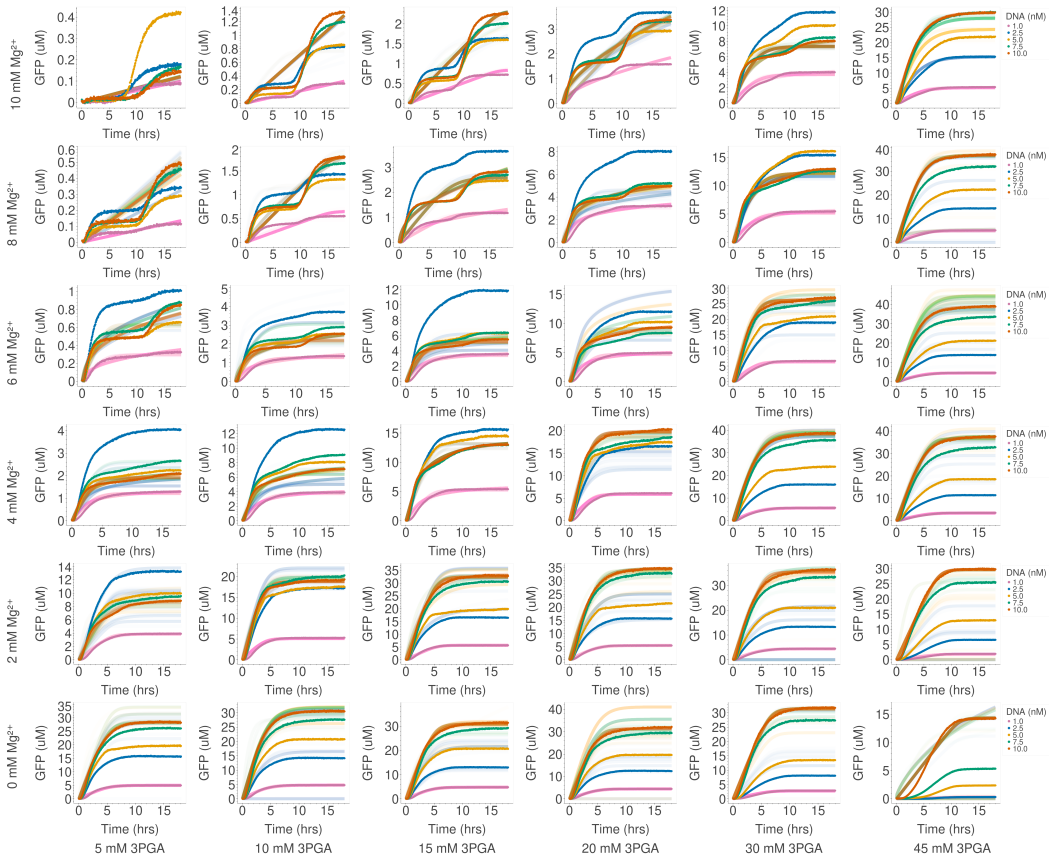

Figure S3.4: Comparison of model prediction and experimental data after fine-tuning as shown in Figure 3.3 and using 2 time trajectories as training data. For each of the 36 fine-tunings, data corresponding to DNA concentrations of 1 nM and 10 nM were provided as training data, and the data corresponding to 2.5 nM DNA, 5 nM DNA, and 7.5 nM DNA for the same set of 3PGA and Mg^{2+} concentrations were provided as test data (yellow, green, and blue lines). Darker points are experimental data; lighter lines of the same color are model predictions. Darker points are experimental data; lighter lines of the same color are model predictions.

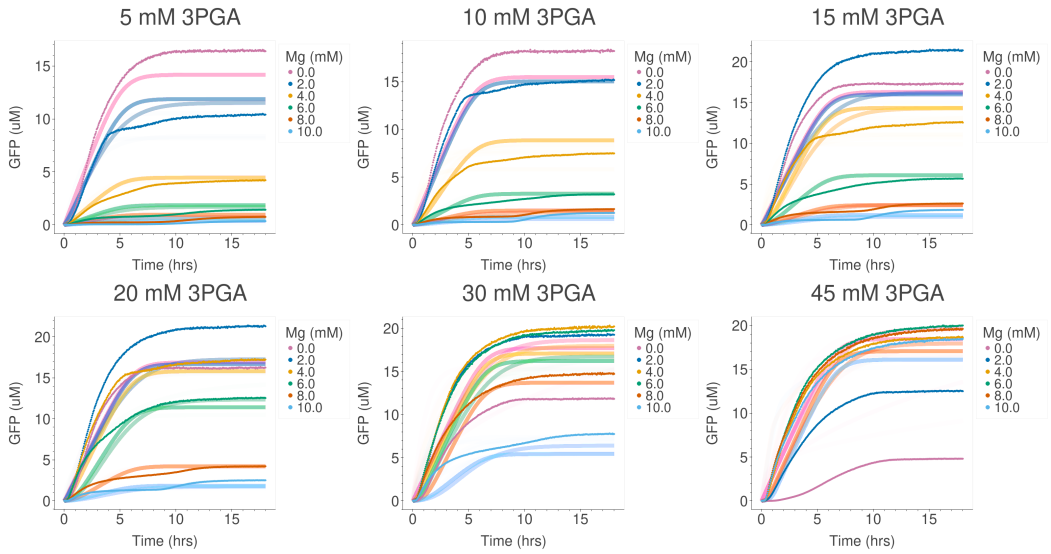

Figure S3.5: Comparison of model prediction and experimental data after fine-tuning as shown in Figure 3.5 and using all 36 time trajectories as training data for Lysate Batch 1 from a previously published study [25].

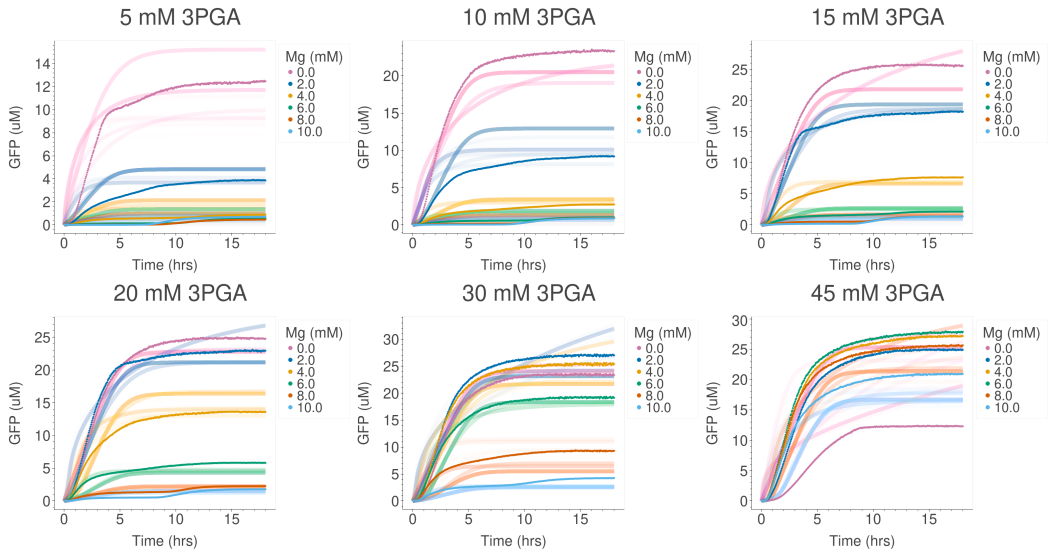

Figure S3.6: Comparison of model prediction and experimental data after fine-tuning as shown in Figure 3.5 and using all 36 time trajectories as training data for Lysate Batch 2 from a previously published study [25].

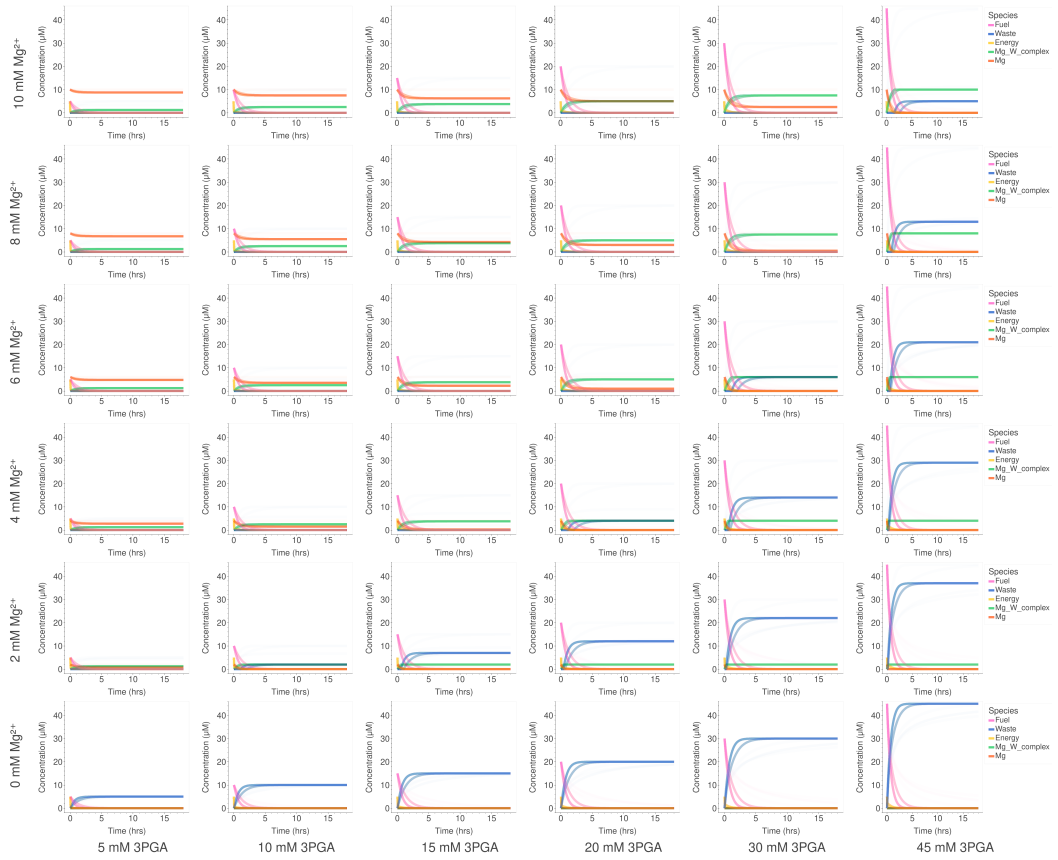

Figure S3.7: Modeling unmeasured species after fine-tuning as shown in Figure 3.5 for Lysate Batch 1 from a previously published study [25]. A single model was trained and parameterized for the 36 experimental conditions shown in the plot. The Mg-W complex species is the same as species X in Figure 3.5A.

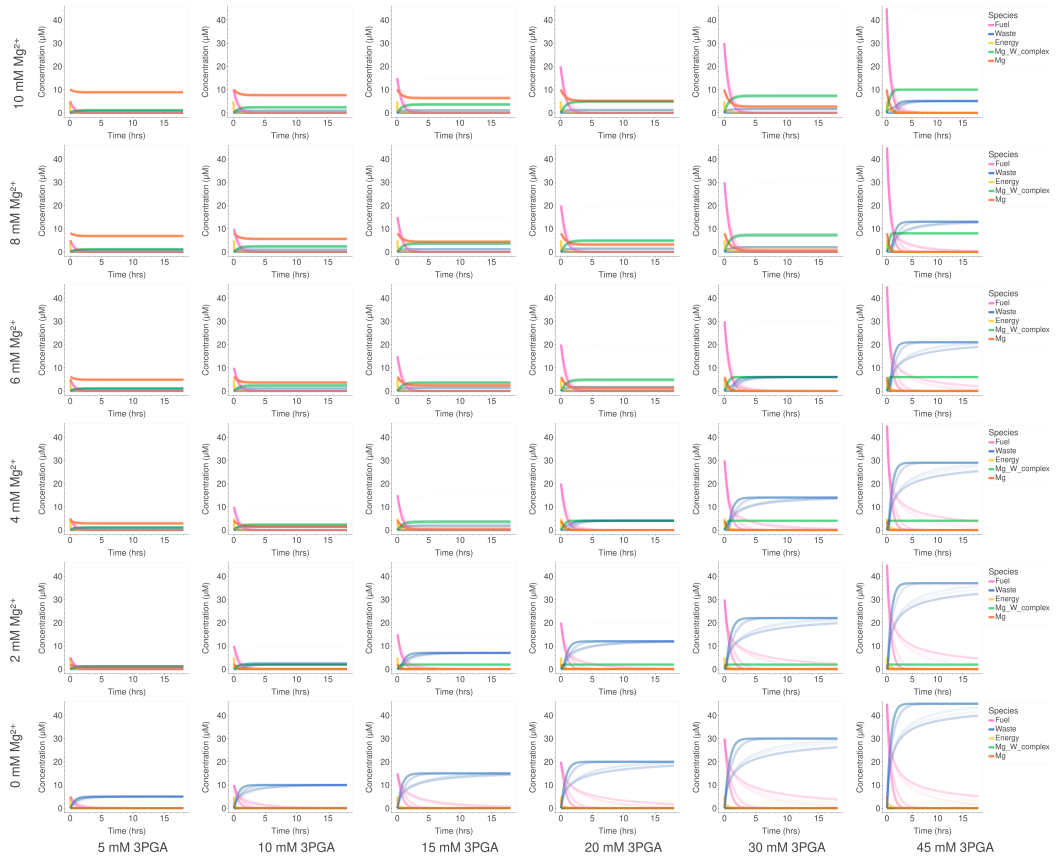

Figure S3.8: Modeling unmeasured species after fine-tuning as shown in Figure 3.5 for Lysate Batch 2 from a previously published study [25]. A single model was trained and parameterized for the 36 experimental conditions shown in the plot. The Mg-W complex species is the same as species X in Figure 3.5A.

Additional supporting information

Additional supporting information includes all data and code used for analysis and figure generation. These are available on GitHub at the following link:

https://github.com/mkapasiawala/cellfree_metabolomics_modeling_finetuning.

References

[1] David Garenne et al. "Cell-free gene expression." In: *Nature Reviews Methods Primers* 1.1 (2021), p. 49. ISSN: 2662-8449. DOI: 10.1038/s43586-021-00046-x.

[2] Zachary Z. Sun et al. "Protocols for implementing an *Escherichia coli* based TX-TL cell-free expression system for synthetic biology." In: *JoVE* 79 (2013). Publisher: MyJoVE Corp, e50762. ISSN: 1940-087X. DOI: 10.3791/50762.

[3] August Brookwell, Javin P. Oza, and Filippo Caschera. "Biotechnology applications of cell-free expression systems." In: *Life* 11.12 (2021). ISSN: 2075-1729. DOI: 10.3390/life11121367.

[4] Melissa K. Takahashi et al. "Characterizing and prototyping genetic networks with cell-free transcription–translation reactions." In: *Bacterial and Archaeal Transcription* 86 (2015), pp. 60–72. ISSN: 1046-2023. DOI: 10.1016/j.ymeth.2015.05.020.

[5] Richard Kelwick et al. "Development of a *Bacillus subtilis* cell-free transcription-translation system for prototyping regulatory elements." In: *Metabolic Engineering* 38 (2016), pp. 370–381. ISSN: 1096-7176. DOI: 10.1016/j.ymben.2016.09.008.

[6] Ashty S. Karim et al. "*In vitro* prototyping and rapid optimization of biosynthetic enzymes for cell design." In: *Nature Chemical Biology* 16.8 (2020), pp. 912–919. ISSN: 1552-4469. DOI: 10.1038/s41589-020-0559-0.

[7] Bastian Vögeli et al. "Cell-free prototyping enables implementation of optimized reverse beta-oxidation pathways in heterotrophic and autotrophic bacteria." In: *Nature Communications* 13.1 (2022), p. 3058. ISSN: 2041-1723. DOI: 10.1038/s41467-022-30571-6.

[8] Zoe Swank and Sebastian J. Maerkl. "CFPU: a cell-free processing unit for high-throughput, automated in vitro circuit characterization in steady-state conditions." In: *BioDesign Research* 2021 (2021), p. 2968181. ISSN: null. DOI: 10.34133/2021/2968181.

[9] Caitlin Sharpes et al. "Assessment of colorimetric reporter enzymes in the PURE system." In: *ACS Synthetic Biology* 10.11 (2021). Publisher: American Chemical Society, pp. 3205–3208. DOI: 10.1021/acssynbio.1c00360.

[10] Yan Zhang et al. "Point-of-care analyte quantification and digital readout via lysate-based cell-free biosensors interfaced with personal glucose monitors." In: *ACS Synthetic Biology* 10.11 (2021). Publisher: American Chemical Society, pp. 2862–2869. DOI: 10.1021/acssynbio.1c00282.

[11] Peter Q. Nguyen et al. "Wearable materials with embedded synthetic biology sensors for biomolecule detection." In: *Nature Biotechnology* 39.11 (2021), pp. 1366–1374. ISSN: 1546-1696. DOI: 10.1038/s41587-021-00950-3.

[12] Jonghyeon Shin, Paul Jardine, and Vincent Noireaux. "Genome replication, synthesis, and assembly of the bacteriophage T7 in a single cell-free reaction." In: *ACS Synthetic Biology* 1.9 (2012), pp. 408–413. DOI: 10.1021/sb300049p.

[13] Erik Henrich et al. "Membrane protein production in *Escherichia coli* cell-free lysates." In: *FEBS Letters* 589.15 (2015), pp. 1713–1722. ISSN: 0014-5793. DOI: 10.1016/j.febslet.2015.04.045.

[14] Lena Thoring et al. "High-yield production of "difficult-to-express" proteins in a continuous exchange cell-free system based on CHO cell lysates." In: *Scientific Reports* 7.1 (2017), p. 11710. ISSN: 2045-2322. DOI: 10.1038/s41598-017-12188-8.

[15] Pawel Leznicki et al. "Co-translational biogenesis of lipid droplet integral membrane proteins." In: *Journal of Cell Science* 135.5 (2021), jcs259220. ISSN: 0021-9533. DOI: 10.1242/jcs.259220.

[16] Yutaro Yamaoka et al. "Characterization and utilization of disulfide-bonded SARS-CoV-2 receptor binding domain of spike protein synthesized by wheat germ cell-free production system." In: *Viruses* 14.7 (2022). ISSN: 1999-4915. DOI: 10.3390/v14071461.

[17] N. Amy Yewdall, Alexander F. Mason, and Jan C. M. van Hest. "The hallmarks of living systems: towards creating artificial cells." In: *Interface Focus* 8.5 (2018), p. 20180023. DOI: 10.1098/rsfs.2018.0023.

[18] Eunhee Cho and Yuan Lu. "Compartmentalizing cell-free systems: toward creating life-like artificial cells and beyond." In: *ACS Synthetic Biology* 9.11 (2020), pp. 2881–2901. DOI: 10.1021/acssynbio.0c00433.

[19] Lynn J. Rothschild et al. "Building synthetic cells - from the technology infrastructure to cellular entities." In: *ACS Synthetic Biology* (2024). DOI: 10.1021/acssynbio.3c00724.

[20] Yoshihiro Shimizu et al. "Cell-free translation reconstituted with purified components." In: *Nature Biotechnology* 19.8 (2001), pp. 751–755. ISSN: 1546-1696. DOI: 10.1038/90802.

[21] Laura Grasemann et al. "OnePot PURE cell-free system." In: *JoVE* 172 (2021), e62625. ISSN: 1940-087X. DOI: 10.3791/62625.

[22] Léa Wagner, Matthieu Jules, and Olivier Borkowski. "What remains from living cells in bacterial lysate-based cell-free systems." In: *Computational and Structural Biotechnology Journal* 21 (2023), pp. 3173–3182. ISSN: 2001-0370. DOI: 10.1016/j.csbj.2023.05.025.

[23] Grace E. Vezeau and Howard M. Salis. "Tuning cell-free composition controls the time delay, dynamics, and productivity of TX-TL expression." In: *ACS Synthetic Biology* 10.10 (2021), pp. 2508–2519. DOI: 10.1021/acssynbio.1c00136.

[24] Alice M. Banks et al. “Key reaction components affect the kinetics and performance robustness of cell-free protein synthesis reactions.” In: *Computational and Structural Biotechnology Journal* 20 (2022), pp. 218–229. ISSN: 2001-0370. DOI: 10.1016/j.csbj.2021.12.013.

[25] Manisha Kapasiawala and Richard M. Murray. “Metabolic perturbations to an Escherichia coli-based cell-free system reveal a trade-off between transcription and translation.” In: *ACS Synthetic Biology* 13.12 (2024), pp. 3976–3990. DOI: 10.1021/acssynbio.4c00361.

[26] Jan Müller, Martin Siemann-Herzberg, and Ralf Takors. “Modeling cell-free protein synthesis systems —– approaches and applications.” In: *Frontiers in Bioengineering and Biotechnology* 8 (2020). DOI: 10.3389/fbioe.2020.584178.

[27] Thales R. Spartalis et al. “Current application of modeling and cell-free system for synthetic gene circuit design.” In: *Synthetic Biology and Engineering* (2024). DOI: sbe.2024.10013.

[28] Sabine Arnold et al. “Model-based inference of gene expression dynamics from sequence information.” In: *Biotechnology for the Future* (2005), pp. 89–179. DOI: 10.1007/b136414.

[29] Eyal Karzbrun et al. “Coarse-grained dynamics of protein synthesis in a cell-free system.” In: *Physical Review Letters* 106.4 (2011), p. 048104. DOI: 10.1103/PhysRevLett.106.048104.

[30] Tobias Roland Stögbauer et al. “Experiment and mathematical modeling of gene expression dynamics in a cell-free system.” In: *Integrative Biology: Quantitative Biosciences from Nano to Macro* 4.5 (2012), pp. 494–501. DOI: 10.1039/c2ib00102k.

[31] Abhinav Adhikari et al. “Effective biophysical modeling of cell free transcription and translation processes.” In: *Frontiers in Bioengineering and Biotechnology* 8 (2020). DOI: 10.3389/fbioe.2020.539081.

[32] Vipul Singhal et al. “A MATLAB toolbox for modeling genetic circuits in cell-free systems.” In: *Synthetic Biology* 6.1 (2021), ysab007. ISSN: 2397-7000. DOI: 10.1093/synbio/ysab007. (Visited on 10/19/2022).

[33] Angelina Yurchenko et al. “Mechanism-based and data-driven modeling in cell-free synthetic biology.” In: *Chemical Communications* (2024). DOI: 10.1039/d4cc01289e.

[34] Michael Vilkhovoy et al. “Sequence specific modeling of *E. coli* cell-free protein synthesis.” In: *ACS Synthetic Biology* 7.8 (2018). Publisher: American Chemical Society, pp. 1844–1857. DOI: 10.1021/acssynbio.7b00465.

[35] Nicholas Horvath et al. "Toward a genome scale sequence specific dynamic model of cell-free protein synthesis in *Escherichia coli*." In: *Metabolic Engineering Communications* 10 (2020), e00113. ISSN: 2214-0301. DOI: 10.1016/j.mec.2019.e00113.

[36] April M. Miguez, Monica P. McNerney, and Mark P. Styczynski. "Metabolic profiling of *Escherichia coli*-based cell-free expression systems for process optimization." In: *Industrial & Engineering Chemistry Research* 58.50 (2019), pp. 22472–22482. ISSN: 0888-5885. DOI: 10.1021/acs.iecr.9b03565.

[37] April M. Miguez et al. "Metabolic dynamics in *Escherichia coli*-based cell-free systems." In: *ACS Synthetic Biology* 10.9 (2021). Publisher: American Chemical Society, pp. 2252–2265. DOI: 10.1021/acssynbio.1c00167.

[38] Xiunan Yi et al. "Establishing a versatile toolkit of flux enhanced strains and cell extracts for pathway prototyping." In: *Metabolic Engineering* 80 (2023), pp. 241–253. ISSN: 1096-7176. DOI: 10.1016/j.ymben.2023.10.008.

[39] William Poole. "Compilation and inference with chemical reaction networks." PhD Thesis. California Institute of Technology, 2021.

[40] Zachary A. Martinez, Richard M. Murray, and Matt W. Thomson. "TRILL: Orchestrating modular deep-learning workflows for democratized, scalable protein analysis and engineering." In: *bioRxiv* (2023). ISSN: 2692-8205. DOI: 10.1101/2023.10.24.563881.

[41] Sepideh Maleki et al. *Efficient fine-tuning of single-cell foundation models enables zero-shot molecular perturbation prediction.* 2025. DOI: 10.48550/arXiv.2412.13478. arXiv: 2412.13478 [cs.LG].

[42] Yunda Si et al. "Foundation models in molecular biology." eng. In: *Biophysics Reports* 10.3 (2024), pp. 135–151. ISSN: 2364-3420 2364-3439. DOI: 10.52601/bpr.2024.240006.

[43] Qing Li et al. "Progress and opportunities of foundation models in bioinformatics." In: *Briefings in Bioinformatics* 25.6 (2024), bbae548. ISSN: 1477-4054. DOI: 10.1093/bib/bbae548.

[44] Kevin S. Brown and James P. Sethna. "Statistical mechanical approaches to models with many poorly known parameters." In: *Physical Review E: Statistical, Nonlinear, and Soft Matter Physics* 68 2 Pt 1 (2003), p. 021904. DOI: 10.1103/PHYSREVE.68.021904.

[45] Pavel Loskot, Kolmon Atitey, and Lyudmila Mihaylova. "Comprehensive review of models and methods for inferences in bio-chemical reaction networks." In: *Frontiers in Genetics* 10 (2019). ISSN: 1664-8021. DOI: 10.3389/fgene.2019.00549.

[46] Pakpoom Subsoontorn, Jongmin Kim, and Erik Winfree. "Ensemble Bayesian analysis of bistability in a synthetic transcriptional switch." In: *ACS Synthetic Biology* 1.8 (2012), pp. 299–316. DOI: 10.1021/sb300018h.

[47] Nikhil Galagali and Youssef M Marzouk. "Bayesian inference of chemical kinetic models from proposed reactions." In: *Chemical Engineering Science* 123 (2015), pp. 170–190. DOI: 10.1016/j.ces.2014.10.030.

[48] Gareth W Molyneux, Viraj B Wijesuriya, and Alessandro Abate. "Bayesian verification of chemical reaction networks." In: *International Symposium on Formal Methods*. Springer. 2019, pp. 461–479. DOI: 10.1007/978-3-030-54997-8_29.

[49] Ryan N. Gutenkunst et al. "Universally sloppy parameter sensitivities in systems biology models." In: *PLoS Computational Biology* 3 (2007). DOI: 10.1371/journal.pcbi.0030189.

[50] Mark K. Transtrum et al. "Perspective: sloppiness and emergent theories in physics, biology, and beyond." In: *The Journal of Chemical Physics* 143.1 (2015), p. 010901. ISSN: 0021-9606. DOI: 10.1063/1.4923066.

[51] Vipul Singhal and Richard M. Murray. "Transforming data across environments despite structural non-identifiability." In: *2019 American Control Conference (ACC)*. IEEE. 2019, pp. 5639–5646. DOI: 10.23919/ACC.2019.8814953.

[52] Lillian Garfinkel and David Garfinkel. "Magnesium regulation of the glycolytic pathway and the enzymes involved." In: *Magnesium* 4.2-3 (1985), pp. 60–72.

[53] Tae-Wan Kim, Dong-Myung Kim, and Cha-Yong Choi. "Rapid production of milligram quantities of proteins in a batch cell-free protein synthesis system." In: *Journal of Biotechnology* 124.2 (2006), pp. 373–380. ISSN: 0168-1656. DOI: 10.1016/j.jbiotec.2005.12.030.

[54] William Poole et al. "BioCRNpyler: Compiling chemical reaction networks from biomolecular parts in diverse contexts." In: *BioRxiv* (2020). DOI: 10.1101/2020.08.02.233478.

[55] Michael Hucka et al. "The systems biology markup language (SBML): a medium for representation and exchange of biochemical network models." In: *Bioinformatics* 19.4 (2003), pp. 524–531. DOI: 10.1093/bioinformatics/btg015.

[56] Ayush Pandey et al. "Fast and flexible simulation and parameter estimationfor synthetic biology using bioscrape." In: *Journal of Open Source Software* 8.83 (2023). DOI: 10.21105/joss.05057.

Chapter 4

TOWARDS AN ATP SYNTHASE-POWERED PROTOFLAGELLUM FOR SYNTHETIC CELL MOTILITY

4.1 Introduction

Motility is a hallmark of cellular life. In many multicellular organisms, cell motility enables complex processes like morphogenesis, growth, wound healing, and reproduction [1, 2]. In unicellular organisms, motility is essential for survival, allowing an organism to traverse its environment to search for food, escape predators, seek microbial communities, exchange genetic information, and reproduce [2]. Unicellular organisms lacking motility can be found in nutrient-rich environments, like *K. pneumoniae* in soil, or have adapted to take advantage of their environments, such as diatoms propelled by ocean currents [3, 4]. In humans, cell motility plays important in roles in cancer, pathogenicity, and the immune response [5, 6].

Inspired by the prevalence and implications of cell motility, several efforts have been made towards engineering microswimmers for novel applications. Recent examples include a DNA origami nanorobot programmed to find tumors and subsequently release a drug payload in mice, magnetic helical microswimmers functionalized with pDNA on their surfaces for gene delivery, and optimizing oil-eating marine bacterium *A. borkumensis* for improved degradation of hydrocarbons during oil spills [7, 8]. Given the need for biocompatibility in many of these applications, several studies have focused on engineering microorganisms, due to their abilities to carry cargo, process signals from environmental inputs, and make complex decisions in response to those signals [9, 10]. However, using microorganisms comes with its own set of challenges, including lack of predictability, arising from crosstalk among native and engineered cell components, and major safety and efficacy concerns, including the potential for microorganisms to rapidly mutate and become non-functional, invasive, or even pathogenic [9, 10].

Seeking the advantages of microbial microswimmers while addressing these challenges, synthetic biology has aimed to construct motility in synthetic cells [11]. Synthetic cells, built from the bottom up from individual biological components, are microscopic compartments encapsulating a mixture that enables a biomolecular program. In the simplest case, synthetic cells are liposomes, bounded by a phos-

pholipid bilayer and containing an aqueous solution; however, other biological/non-biological boundaries and inner solutions have been deployed. Ultimately, the field of synthetic cell research aims to understand the origins and limits of life, gain insight into existing biological systems, and even engineer life from scratch [12]. Past work has focused on reconstituting many functions of living cells in synthetic cells, including transcription and translation (TX-TL), DNA replication, metabolism, cell division, biochemical sensing, membrane transport, and more [12].

Many previous efforts have focused on engineering motility in synthetic cells; these efforts have ranged from bio-inspired design to novel motility mechanisms [11, 13]. In one study, the authors extracted the flagellar filaments of *Chlamydomonas reinhardtii* and by directly reattaching the filaments to microbeads and liposomes (the latter via a biotin-streptavidin system), demonstrated ATP-driven motion of these flagellate micro-objects [14]. Several other studies have described non-flagellar motion of liposomes, self-propelled by processes such as phototaxis [15], ion exchange [16], and osmosis [17]. In another study, the authors demonstrated tumbling motility of a liposome along a patterned surface [18].

While each of these studies have shown directed motion of liposomes, the need for a precisely controlled motility environment in each of these experiments underscores the need for a self-contained actuation system, where velocity and direction of motility are governed predictably by separate mechanisms and where direction can be controlled by desired inputs. Here, we describe efforts made towards constructing a new motility mechanism in synthetic cells: an artificial "proto-flagellum."

4.2 Experimental design

Cells move using one of many different mechanisms [19, 20]. Flagella, one of the most widespread motility mechanisms, are tail-like appendages that propel the cell by (1) rotation of a filament attached to a rotary motor or (2) active beating of the flagellum induced by the action of motor proteins along the flagellum. Cilia, another motility mechanism, consist of hundreds or thousands of small hairlike membrane protrusions on the exterior of a cell whose beating induces movement of eukaryotic cells. Meanwhile, unicellular organisms belonging to the phylum Spirochaetes or the genus *Spiroplasma* have a helical morphology that allows them to move by twisting. Cells using amoeboid movement can crawl along a surface by extending their cytoplasm along a surface to form psuedopodia or uropods "false feet"); amoeboid movement also includes gliding and non-flagellar swimming as

motility mechanisms. Beyond these mechanisms, additional motility mechanisms include twitching and non-amoeboid gliding motility, among others [19].

Perhaps the best studied example is flagellar motility in *E. coli*, which are propelled by a proton-powered rotor that drive rotation of long protein filaments. In *E. coli*, these filaments bundle together and rotate at a rotational speed of about 130 Hz, enabling the cell to swim at a translational speed of about 25 µm/s [20]. The *E. coli* flagellum would be extremely challenging to functionally reconstitute in a synthetic cell; recent efforts have only been able to reproduce assembly of a bacterial flagellum starting from partially complete structures, and it remains unknown whether the flagellum produced was functional [21]. However, these efforts provide a blueprint for generating a flagellum-inspired motility mechanism consisting of an alternative rotary engine fused to protein filaments that act as external propellers (Figure 4.1).

In our design, we chose a simpler rotary motor, *E. coli* F_1F_O ATP synthase, a membrane protein complex central to energy metabolism [22]. In the proposed design (Figure 4.1), liposomes would be co-reconstituted with a proton pump and ATP synthase. The proton pump would create the transmembrane pH gradient necessary for ATP synthase rotation. This would drive the helical rotation of an actin filament, bound to the ATP synthase via a streptavidin-biotin complex, and subsequent propulsion of the liposome.

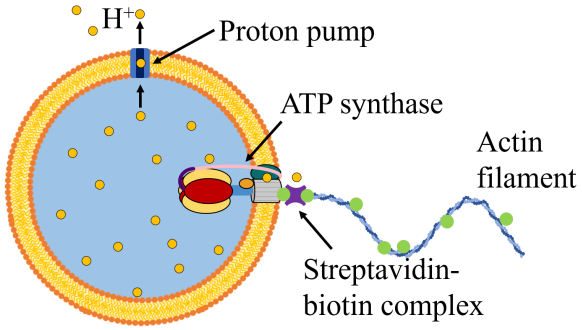

Figure 4.1: Synthetic cell powered by an ATP synthase-based proto-flagellum.

Three different experimental approaches were considered for implementing the proposed design: reconstitution of existing actuation complexes, reconstitution of modified actuation complexes, and *in vesicle* expression of membrane proteins.

Approach 1: simple reconstitution of functional actuation complexes

In this first approach, the proposed design (Figure 4.1) would be implemented as is, by simply putting together two individually working systems described previously in the literature: (1) proteoliposomes co-reconstituted with proton pumps and ATP synthase, and (2) rotation of actin filaments bound to ATP synthase (Figure 4.2).

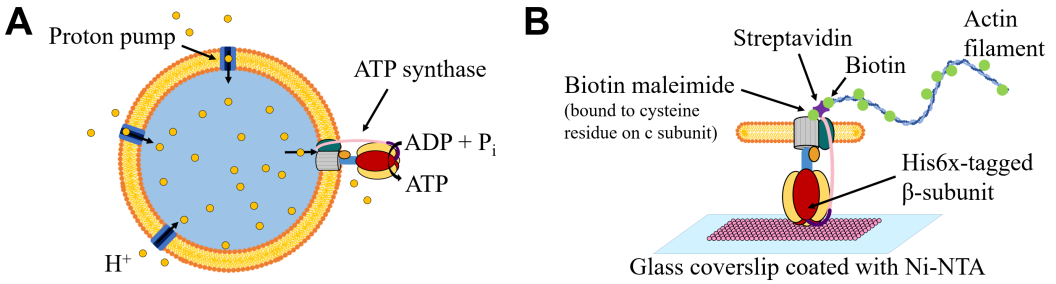

Figure 4.2: Building blocks for an ATP synthase-based protoflagellum. (a) A proteoliposome co-reconstituted with a proton pump and ATP synthase. (b) Rotation of an actin filament covalently attached to a coverslip-bound ATP synthase.

Many prior studies have described the purification and co-reconstitution of ATP synthase and proton pumps, such as bacteriorhodopsin and bo3 oxidase, into liposome membranes [11]. The resulting proteoliposomes produced ATP either continuously, with bo3 oxidase (with the appropriate chemical substrates present), or inducibly, with bacteriorhodopsin (which pumps protons upon illumination by green light).

Many studies have also described the successful rotation of actin filaments covalently attached to coverslip-bound ATP synthase [23–25]. In these experiments, ATP synthase was His6x-tagged on one end and bound to a coverslip coated with Ni-NTA resin, a substrate that is commonly used in the purification of His6x-tagged proteins. The otherwise cysteine-less ATP synthase had cysteine residues on a protein subunit on the opposite end of the complex, allowing for the covalent attachment of biotin maleimide. The subsequent sequential addition of streptavidin and a biotinylated actin filament resulted in an ATP synthase with an attached actin filament. Upon the addition of ATP, the resulting ATP hydrolysis caused rotation of the ATP synthase, and thus rotation of the bound actin filament, as observed under microscopy.

The simplest assembly of an ATP synthase-based protoflagellum would consist of incubating proteoliposomes with biotinylated actin filaments. The streptavidin and biotin maleimide could be incubated with either the proteoliposomes before their incubation with the biotinylated actin filaments, or with the latter before their incubation with the former. Depending on whether the proton pump used is bacteriorhodopsin or bo3 oxidase, subsequent illumination by green light or addition of ubiquinone Q1 and DTT, respectively, would drive synthetic cell motility.

While this approach is the simplest of the three discussed here, its efficiency is severely limited by the orientation of the reconstituted membrane proteins. Membrane proteins usually have a preferred orientation during insertion, and the desired

orientation for both the proton pumps and ATP synthase as shown in Figure 4.1 is only achieved about 10-30% of the time, per protein [26]. This is especially problematic because membrane proteins that are oriented the wrong way can undo the proton gradient required for ATP synthase rotation. While various methods have been employed to manipulate the orientations of membrane proteins, whether by using charged lipids or different detergents during reconstitution, these methods have only improved efficiency of the opposite orientation, as that orientation is the preferred one used for membrane protein assays and energy regeneration modules [27, 28]. Thus, while we attempted to implement this approach, we also considered two additional approaches towards creating an ATP synthase-based protoflagellum.

Approach 2: reconstitution of modified actuation complexes

Since achieving the desired orientation of the proton pump and ATP synthase, shown in Figure 4.1, is difficult, an alternative strategy is to use the preferred orientation of the membrane proteins as an experimental advantage. Understanding this approach requires a brief introduction to the structure and function of ATP synthase.

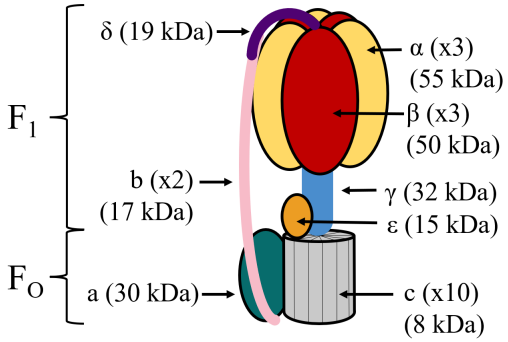

Figure 4.3: F_1F_O ATP synthase structure.

As mentioned previously, ATP synthase is a protein complex central to energy metabolism. The bacterial F_1F_O ATP synthase consists of a total of 20-25 membrane protein subunits that assemble to form a complex with motors: the F_O motor, located in transmembrane region, and the F_1 motor, located in the cytoplasm (Figure 4.3). The F_O motor can use a transmembrane proton gradient to catalyze the production of ATP from ADP and P_i, while the F_1 motor can use ATP hydrolysis to pump protons outside the cytoplasm and into the intermembrane space, i.e., between the inner and outer membranes [29]. In the case of the former, torque is generated from the rotation of the c-ring, while in the case of the latter, torque is generated from the rotation of the γ shaft.

A previous study found that the two motors, while coupled, function independently; notably, a functional F_O complex can be assembled *in vivo* even in the absence of the α, β, ϵ, and γ subunits [30]. This raises an interesting possibility: could we

create an ATP synthase-powered protoflagellum using a modified ATP synthase, specifically one lacking its α and β subunits? The advantage of this approach is that the orientations of the membrane proteins do not need to be changed; an actin filament could simply be attached to the now-exposed γ shaft and rotate upon the generation of a transmembrane proton gradient (Figure 4.4).

This approach would require more effort than Approach 1, since some molecular cloning is required to generate plasmids encoding the ATP synthase variants. An even greater hurdle is the expression and purification of these variants from *E. coli*; the modified ATP synthase complexes would likely dissipate the proton gradients normally maintained in these cells and thus reduce the viability of the cells expressing the variants. To mitigate these growth effects, several variants can be explored, each with different subunits absent from the protein complex (Figure 4.5).

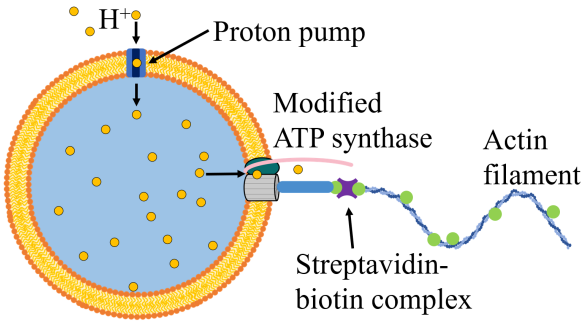

Figure 4.4: Synthetic cell powered by a modified ATP synthase-based proto-flagellum. The α, β, and δ subunits have been removed.

While molecular cloning was used to make the ATP synthase variants, downstream bottlenecks encouraged us to prioritize our efforts towards other parts of the project.

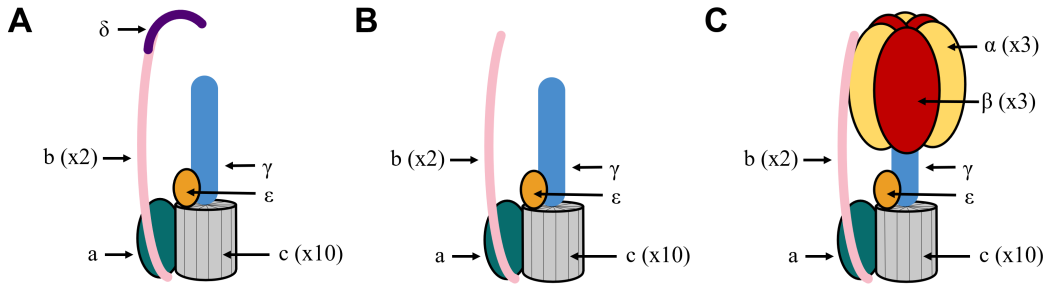

Figure 4.5: F_1F_O ATP synthase variants that can used as part of a protoflagellar complex. (a) Variant with α and β subunits removed to expose the rotating γ subunit. (b) Variant (a) but with δ subunit removed to prevent any possible interference with the rotation of an attached actin filament. (c) Variant with δ subunit, to see if absence of δ subunit enables the rotation of the α/β ring.

Approach 3: *in vesicle* expression of membrane proteins

An alternative strategy towards mitigating the membrane protein orientation issue in Approach 1 is the *in vesicle* expression of both the ATP synthase and the proton pump. Previous studies have demonstrated the cell-free expression and assembly of ATP synthase and bacteriorhodopsin [28, 31]. Using synthetic cells encapsulating transcription and translation (TX-TL) machinery, along with plasmids encoding the expression of ATP synthase and either bacteriorhodopsin or bo3 oxidase, would enable the insertion of the membrane complexes in the correct orientation. Once proteoliposomes have been constructed, actin filaments could be attached as described in the sections above, by incubating proteoliposomes successively with biotin maleimide, streptavidin, and biotinylated actin filaments. If this strategy is successful, one could also express actin monomers via the TX-TL system inside the liposome and export them outside the synthetic cell using export machinery such as the Twin-Arginine Translocation (Tat) protein export pathway [32], to make a fully self-assembled actuation complex.

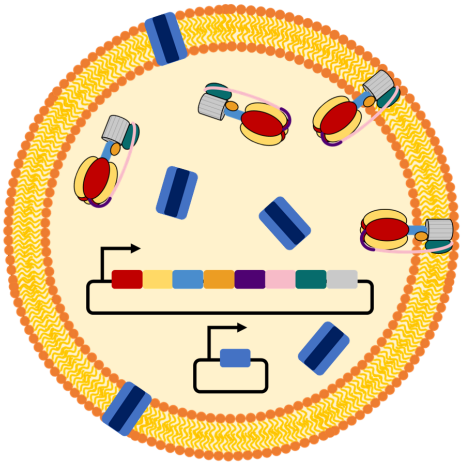

Figure 4.6: Synthetic cell containing TX-TL machinery and plasmids for *in vesicle* expression of ATP synthase and a proton pump.

4.3 Results

As the various experimental approaches share many of the same experimental milestones, this project mostly focused on building and testing individual components of the protoflagellar system.

ATP synthase expression, purification, and reconstitution

The first milestone of this project was the expression, purification, and reconstitution of ATP synthase, which cannot be readily purchased. More details regarding the protocol can be found in the **Materials and methods** section.

For expression of ATP synthase, *E. coli* DK8, a strain with a genome deletion of the *unc* operon encoding for ATP synthase, was used. This strain was transformed with a plasmid pBH2 containing the *unc* operon encoding for a cysteine-less ATP synthase variant with a His6x tag. Expression and affinity purification of ATP synthase was

performed according to a recently published protocol [33]. An SDS-PAGE gel of the purified complex revealed that all of the subunits were present in the complex, at roughly the correct positions on the gel with respect to the ladder (Figure 4.7a).

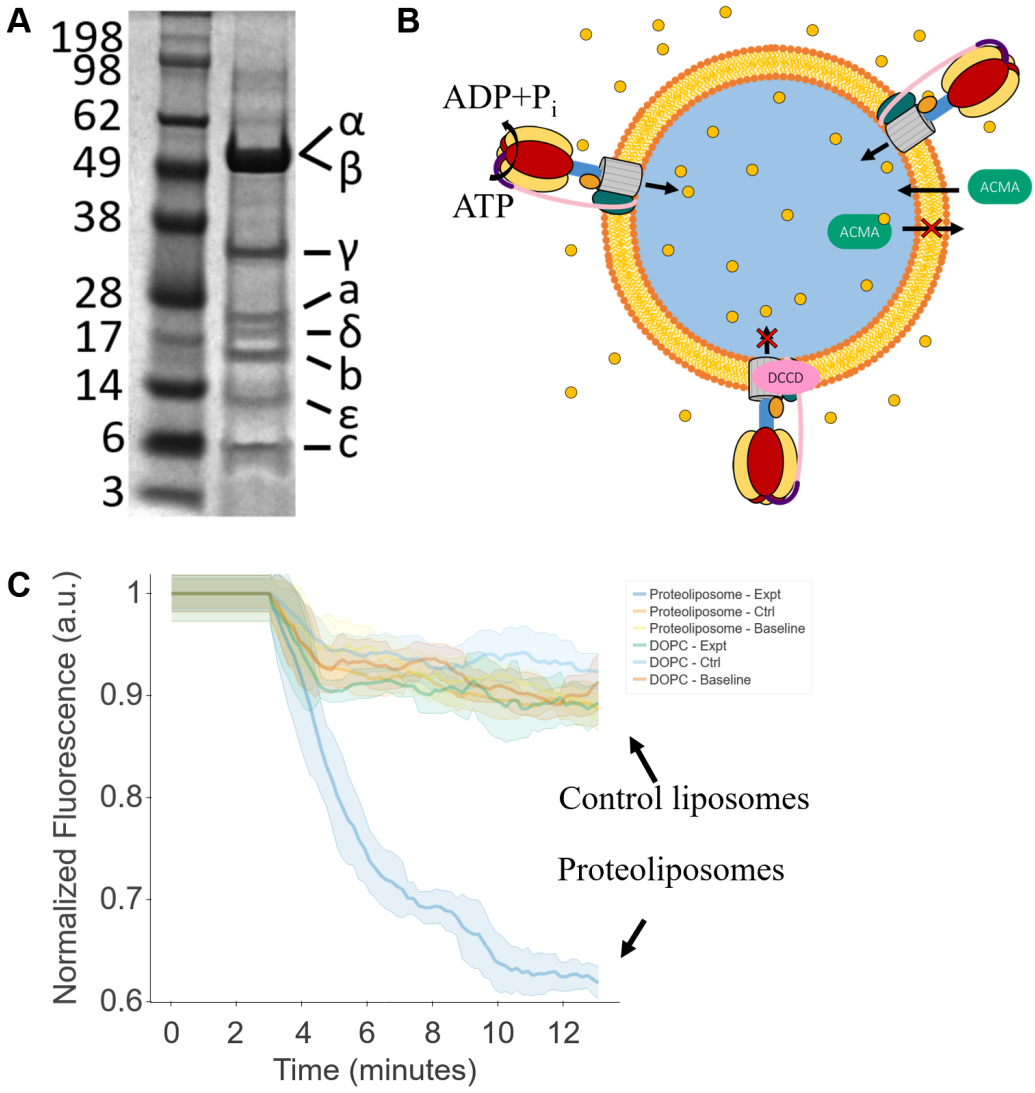

Figure 4.7: ATP synthase expression, purification, and reconstitution. (a) SDS-PAGE gel showing bands for each of the subunits in the purified ATP synthase complex. (b) ACMA quenching assay. (c) Results of the ACMA quenching assay.

To verify that the purified ATP synthase was functional, an ACMA (9-amino-6-chloro-2-methoxyacridine) quenching assay was used, as previously described [33]. Briefly, ACMA is a fluorescent, membrane-permeable small molecule that can be reversibly quenched by protons. In its quenched state, ACMA cannot cross a lipid membrane. Proteoliposomes reconstituted with ATP synthase begin pumping

protons into the liposome upon the addition of ATP to the bulk liposome solution. In the presence of ACMA, protons in the liposome lumen rapidly quench and trap any ACMA inside the liposome. This results in a fluorescence drop that can be measured using a spectrofluorometer or plate reader (in our case, a BioTek Synergy H1 plate reader). As a control, ATP synthase inhibitor DCCD (dicyclohexylcarbodiimide) can be added, to ensure that any observed fluorescence drop is due to ATP synthase activityy (Figure 4.7b).

In our case, ATP synthase was first reconstituted into 100 nm liposomes made of the lipids DOPC (1,2-dioleoyl-sn-glycero-3-phosphocholine) and Lissamine Rhodamine B DHPE (1,2-Dihexadecanoyl-sn-Glycero-3-Phosphoethanolamine) to form proteoliposomes, using the aforementioned protocol [33]. As seen in the results of this assay (Figure 4.7c), only proteoliposomes to which ATP was added and DCCD was not had a large fluorescence drop. Proteoliposomes to which DCCD was added, or to which water was added in place of ATP, did not have a fluorescence drop, nor did liposomes lacking ATP synthase. Having verified that we could express, purify, and functionally reconstitute ATP synthase, we moved on to other parts of the actuation complex.

Actin polymerization and attachment to proteoliposomes

A key part of the protoflagellar complex is an attached filament whose rotation drives motility of the liposome. To this end, we first polymerized fluorescently labeled and biotinylated rabbit muscle actin. We next attached them to silanized coverslips coated with anti-biotin antibody, based on a modified version of an existing protocol [34]. Finally, we imaged the actin under TIRF microscopy, a method used to image samples within 100nm of a coverslip. Microscopy showed that the actin was polymerized successfully (Figure 4.8).

To determine whether actin filaments could selectively bind to ATP synthase on liposomes, we next sequentially incubated proteoliposomes with biotin anti-His6x, streptavidin, and finally biotinylated, fluorescent actin filaments (Figure 4.9a). It is important to note here that the orientation of ATP synthase is the opposite of the desired orientation; here we simply wanted to test whether actin filaments bound to proteoliposomes would be visible under a microscope. While the antibody incubation process resulted in liposome clumping, we were able to observe actin filaments bound only to proteoliposomes and not to control liposomes (Figure 4.9b), although the phenotype was observed at a rate of roughly 5 bound actin filaments

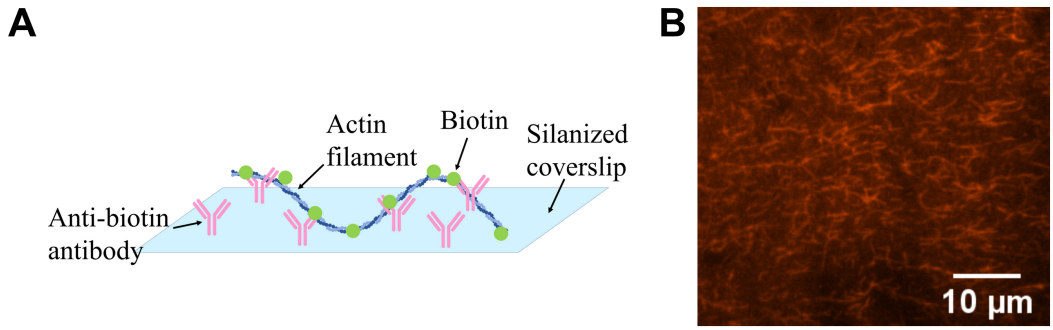

Figure 4.8: Actin attachment to silanzed coverslips. (a) Schematic for the attachment of actin filaments to silanized coverslips. (b) TIRF microscopy of actin filaments.

per 1000 proteoliposomes.

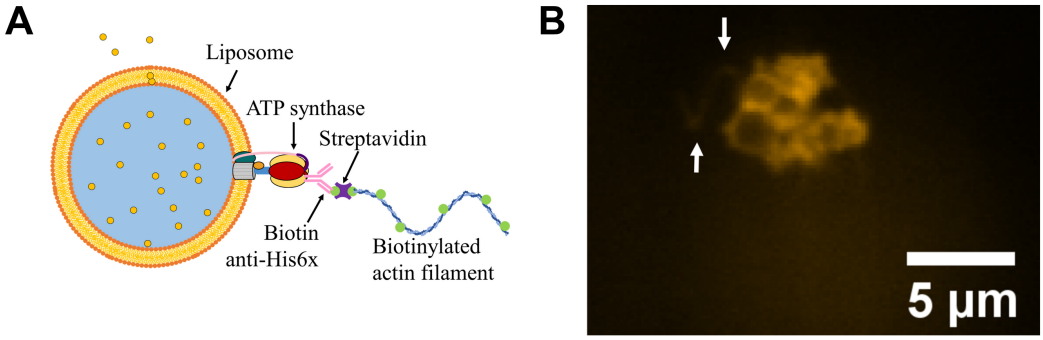

Figure 4.9: Actin attachment to proteoliposomes. (a) Schematic for the attachment of actin filaments to proteoliposomes. (b) Confocal microscope image of actin filament attached to a cluster of proteoliposomes.

This low rate of success is a concern because if the rate of actin filament attachment is low, finding and characterizing motile synthetic cells upon construction of a complete actuation complex may be difficult or close to impossible. Efforts to increase this phenotype were unsuccessful.

Another relevant issue we encountered is that proteoliposomes subjected to the antibody-attachment protocol demonstrated no ATP hydrolysis activity (data not shown). This was likely due to the combination of liposome clumping and the prolonged exposure to protein destabilizing conditions resulting from prolonged incubation at the non-freezing temperatures required for antibody binding.

Rotation of actin filaments attached to coverslip-bound ATP synthase

A key milestone necessary en route to the proposed protoflagellar complex is the observed rotation of actin filaments attached to coverslip-bound ATP synthase (Fig-

ure 4.2b). We attempted to replicate the results of previous studies [23–25]. While we were able to achieve the binding of actin filaments to coverslip bound ATP synthase, as indicated by the rotational pivoting of actin filaments around a central point (Figure 4.10), we were unable to observe the repeated, rapid rotations reported in the literature.

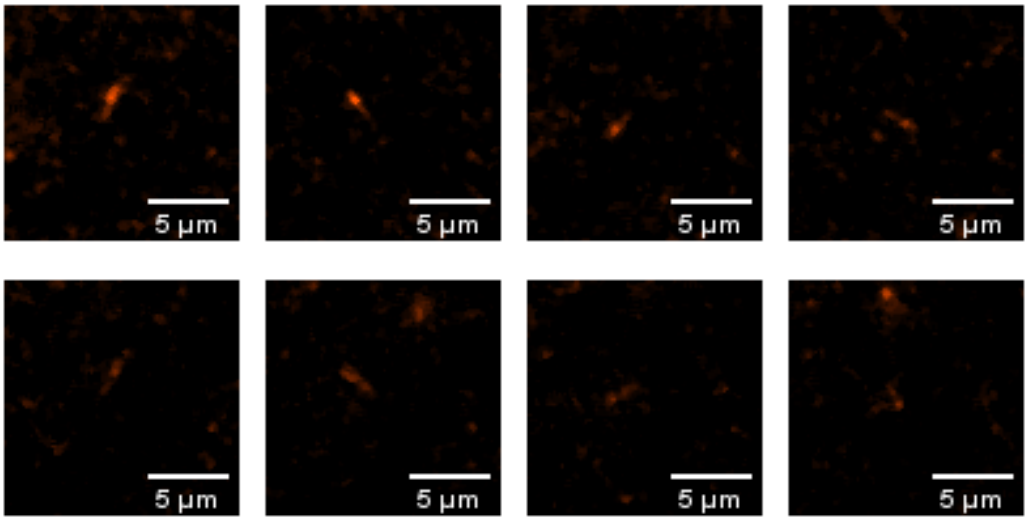

Figure 4.10: Rotation of actin filament attached to ATP synthase-bound coverslip (from top-left to bottom-right). 1.5 counterclockwise rotations were observed over a span of 30 seconds.

Coupled with the difficulty of finding actin filaments that rotated at all, as well as rapid photobleaching of the actin filaments, further troubleshooting is required to confirm that ATP synthase-bound actin filaments can rotate via ATP hydrolysis.

***In vitro* expression of membrane proteins**

Alongside achieving the other milestones, we were interested in expressing the actuation complexes from inside the synthetic cell. Even without a functional protoflagellar complex, achieving this milestone would result in the first reported instance of the assembly of a large membrane protein complex inside a liposome.

Before moving on to *in vesicle* expression, we first attempted to express ATP synthase in a bulk TX-TL system. We tested expression of ATP synthase in both NEB PURExpress as well as a cell lysate-based system. NEB PURExpress is a commercial platform consisting of a mixture of proteins and metabolites necessary for *in vitro* transcription and translation [35]. For the cell lysate-based system, we used lysate prepared from *E. coli* BL21 Rosetta2 cells and followed our lab's protocol for

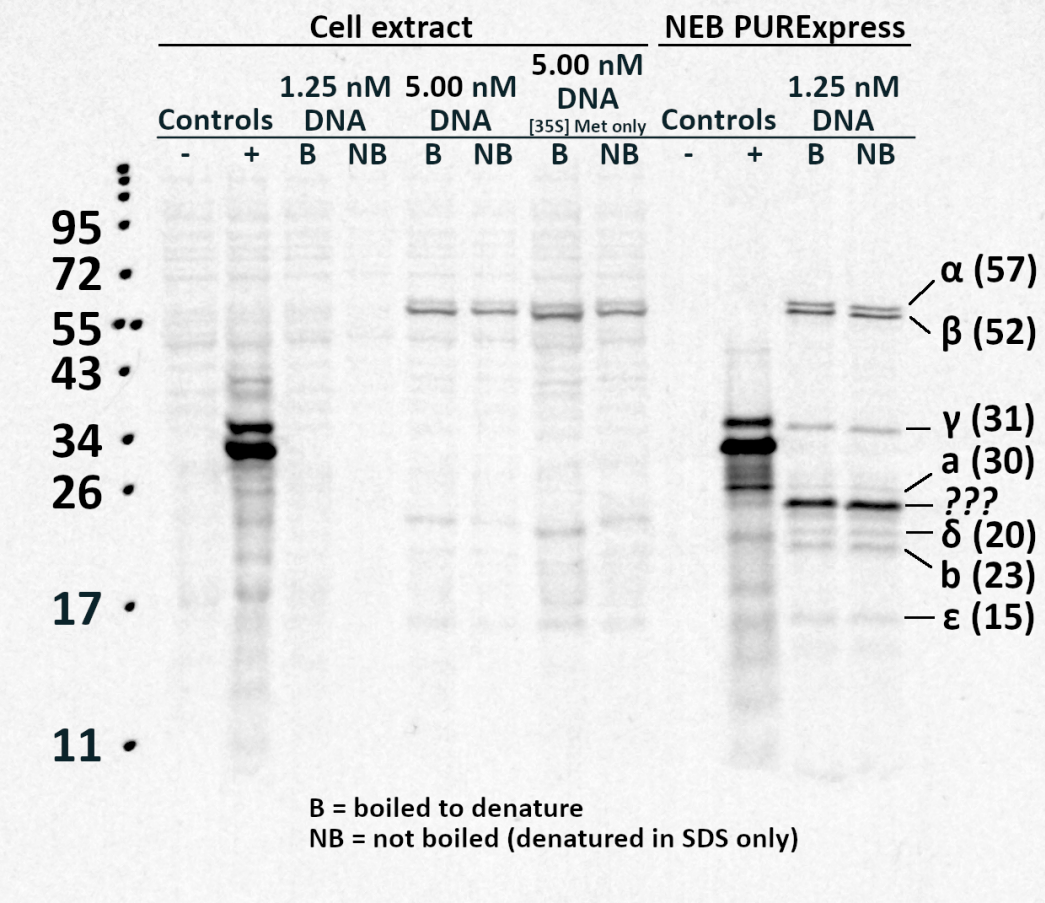

Figure 4.11: *In vitro* expression of ATP synthase in cell-free systems containing radioactive 35S-Methionine. TX-TL systems prepared from cell lysate and NEB PURExpress were supplied with varying amounts of DNA and subjected to different lysis methods (denaturing in SDS versus denaturing in SDS plus incubation at 65°C, i.e., "boiling"). ATP synthase subunits are labeled by their name and molecular weight, with the δ and b subunits assumed to be flipped in order of molecular weight on SDS-PAGE gels [33].

cell lysate preparation [36], although we used a French cell press instead of bead-beating for cell lysis. In both cases, we labeled newly made proteins with radioactive 35S-Methionine, so that running the completed reactions on a SDS-PAGE gel and subsequent exposure would indicate only bands for proteins made in the reaction mixtures (and not the dozens or hundreds of bands corresponding to the proteins that make up each TX-TL system).

With the exception of the c subunit, which ran off the gel since it is only 8 kDa, we were able to observe bands for ATP synthase subunits in both TX-TL systems (Figure 4.11).

Expression in the cell lysate-based system was poor, with only bands for the α, β, and ϵ subunits visible, as well as a band that did not clearly correspond to a single subunit but could correspond to the a, δ, and b subunits. Interestingly, there were many bands not corresponding to any of the subunits, which suggests that may be some background expression from remaining genomic DNA in the cell lysate (Figure S4.1). Future efforts towards troubleshooting expression in cell lysate include adding more DNA to the reaction mixture, using a batch of cell lysate with a higher TX-TL capacity (as measured by a positive control such as deGFP expression), and/or adding liposomes to the reaction mixture to help aid the assembly of the protein complex. A previously published study reported success in using a cell lysate-based TX-TL systems to express ATP synthase [31], so it is also possible that expression is present but the bands are not visible.

Expression in the NEB PURExpress system was better, and the pattern of bands seemed to be consistent with the bands for the purified complex (Figure 4.7), with the exception of a single band that could not be identified. It is worth noting that a previous attempt to express ATP synthase in PURE was unsuccessful; it was suggested that this was due to expression of the subunits in the incorrect ratios, perhaps due to the lack of membrane protein insertases in PURE [28]. However, that previous study did not elaborate on whether ATP synthase expression, assembly, or both were unsuccessful. Thus, to date, the data shown in Figure 4.11 is the first evidence showing it is possible to express all the individual protein subunits of ATP synthase in PURExpress. As large membrane protein complexes like ATP synthase are known to require membrane insertion machinery that is absent in PURE, ongoing work in the field is focusing on developing a membrane protein expression platform in PURE to enable proper expression and assembly of protein complexes.

4.4 Discussion

Given the experimental results, it seems that Approaches 2 and 3 seem to be the ones with the greatest likelihood of success, albeit with some modifications and further work. The following sections highlight some suggestions for troubleshooting and improving upon the proposed experimental approaches.

Actin attachment to proteoliposomes via biotin maleimide

For both approaches, immediate next steps would be to troubleshoot the attachment of actin to proteoliposomes. Since the proteoliposomes generated for the ACMA assay were the same ones used for actin attachment, the ATP synthase was the cysteine-less His6x-tagged pBH2 variant. As a result, the means of attaching the actin filament to the ATP synthase was via a biotin anti-His6x antibody rather than biotin maleimide. Since then, however, we have generated ATP synthase variants with a cysteine residue on the appropriate subunit to enable the actin filament to bind to the ATP synthase via a covalent bond. This should enable stronger binding of the filament, since the free energy of a covalent sulfur-sulfur bond (formed between the sulfur atoms of biotin maleimide and cysteine) is about -266 kJ/mol [37]. While the binding free energy of the anti-His6x biotin mouse antibody to its antigen, the His6x region on ATP synthase, is unknown, the limit of binding affinity between antibodies and protein antigens is about 10^{-11} L mol^{-1}, which roughly corresponds to a free energy of -60 kJ/mol [38]. For a weaker antibody-antigen interaction, the free energy could be as small as -15 kJ/mol [39]. While many more troubleshooting steps may be required to create a functional protoflagellar complex, testing out actin filament attachment via biotin maleimide, as originally planned, should result in 4-10X stronger binding of the filament, thereby increasing the likelihood of observing bound actin filaments under microscopy.

Improvement of the immunolabeling protocol

As mentioned in Section 4.3, proteoliposomes subjected to immunolabeling, prior to the attachment of the actin filament, did not demonstrate ATP hydrolysis activity. Part of the reason behind this is that the immunolabeling protocols were adapted from those designed for cell/tissue cultures and are not necessarily suited for immunolabeling of liposomes.

A typical immunolabeling protocol consists of fixation (preservation of cell components in their current state), permeabilization (penetration of the cell membrane

to allow large molecules to flow through the membrane), and blocking (using a molecule such as Bovine Serum Albumin (BSA) to bind non-specifically to proteins and thus reduce background signal). This is followed by prolonged (several hours to overnight) incubations with a primary antibody, to bind to the molecule of interest, and secondary antibody, to bind to the primary antibody and label it using a fluorescent molecule. Each step is followed by multiple wash steps to get rid of excess molecules from the prior step and enable efficient binding of antibodies.

Mammalian cells and tissues are large (10-150 μm in diameter) and have the structural integrity to withstand the wash steps required for efficient immunolabeling. Meanwhile, the proteoliposomes used in this project were on the order of 100 nm in diameter, roughly 100-1000x smaller. Since the proteoliposomes were in a regime where thermal energy-induced Brownian motion was on the order of gravity, the liposomes would not settle out of solution after the wash steps. This required us to centrifuge the liposomes after each step, which subsequently caused clumping and lysis of the liposomes. After the immunolabeling process, we were typically left with about 10% of the total number of liposomes we started with.

Despite eliminating the fixation and permeabilization steps prior to blocking, we were unable to reduce the loss of liposomes. There is a large search space of steps that can be optimized for improved immunolabeling, but immediate next steps include the following:

- using a greater number of liposomes to start with;
- reducing incubation times with the primary/secondary antibodies to prevent degradation of ATPase machinery;
- running liposomes through a Sephadex G50 column instead of centrifuging them during wash steps; and
- eliminating the blocking step.

Finally, rather than simply incubating proteoliposomes with unpolymerized actin and adding actin polymerization buffer, we could also try to running the proteoliposomes - with their actin filaments - through the Sephadex G50 column. This would enable the removal of any unpolymerized actin and unattached actin filaments. By reducing background fluorescence, this should help improve the visibility of proteoliposomes with attached actin filaments.

Purification and reconstitution of ATP synthase variants

In Section 4.2, we described several ATP synthase variants without the α and β subunits, among others. This would allow for us to use existing membrane protein reconstitution protocols while using the preferred protein orientation to our advantage.

A promising next step would be to perform protein purification of these variants. While these variants prevented growth when transformed into the *E. coli* DK8 strain, likely due to a lethal dissipation of native proton gradients in these cells, they only slowed growth in the *E. coli* NiCo21 strain, a strain optimized for the expression and purification of His6x-tagged proteins. An ACMA assay cannot be used after subsequent reconstitution into liposomes, since the subunits with ATP hydrolysis activity have been removed. However, co-reconstituting the liposomes with a proton pump (see Section 4.4) and subsequent attachment of an actin filament should yield, in the best case scenario, a successful implementation of an actuation complex capable of generating motility upon illumination by green light.

Improved ATP regeneration system for actin rotation assay

Although we were able to observe numerous actin filaments that were bound to the coverslip on one end and capable of pivoting around the contact point, we were unable to observe rapid, repeated rotations of the actin filaments. A possible cause for this is the rapid hydrolysis of ATP by coverslip ATP synthases to which *no* actin filaments have bound. While prior protocols have used an ATP regeneration system involving catalase and glucose oxidase, in addition to ATP and phosphoenolpyruvate (PEP), to power the rotation of ATP synthase, we did not have success with their approaches.

An alternative ATP regeneration strategy, particularly one that has been used successfully for cell-free systems, is the creatine kinase - creatine phosphate system [35]. Here, the phosphate from creatine phosphate is transferred to ADP to regenerate ATP. Using a simplified ATP regeneration system that has been shown to be successful in many labs in various contexts may help us to observe actin filament rotation.

Co-reconstitution of bacteriorhodopsin and ATP synthase

Although the co-reconstitution of Bacteriorhodopsin and ATP synthase has been demonstrated successfully in numerous prior studies [11, 27, 28], we have not yet

done so in our lab. Using commercially purchased bacteriorhodopsin, we aim to co-reconstitute the membrane proteins and demonstrate another step towards a functional actuation complex.

Development of a PURE-based membrane protein expression platform

Thus far, we have described achieved and ongoing efforts towards the specific goal of generating a protoflagellar complex. Ongoing research efforts and discussions surrounding the expression of membrane proteins in *in vitro* TX-TL systems have led us to propose the following: how might we create a minimal platform for membrane protein expression?

A good starting point is the minimal TX-TL platform NEB PURExpress (a commercial version of a published protocol [35]), or the equivalent but cheaper in-house preparation of OnePot PURE [40]. However, these systems are not sufficient. While small membrane proteins have no difficulty folding and inserting themselves into membranes, larger membrane proteins and protein complexes such as ATP synthase require membrane protein insertases for proper folding and insertion [41]. In bacteria, the most widely used ones are SecYEG, YidC, and MPIase [42, 43]. Part of the reason why membrane protein expression is successful in cell lysate-based TX-TL systems [31], and not in PURE [28] may be because cell lysates contain inverted membrane vesicles which may contain these membrane protein insertases and thus aid the assembly and insertion of these proteins.

A previous study found that performing TX-TL of membrane proteins in the presence of proteoliposomes reconstituted with SecYEG, YidC, and MPIase led to the successful expression of membrane proteins dependent on these insertases [43]. However, this system was only used for the TX-TL of small membrane proteins. We hope to adapt and optimize this system for the construction of a minimal *in vitro* TX-TL platform capable of synthesizing large membrane proteins and protein complexes.

4.5 Conclusion

While unsuccessful in its grand goal, this project and its reported progress have generated a significant advancement towards the construction of actuation complexes in synthetic cell membranes. The skills developed by our researchers over the course of this project - membrane protein purification, TIRF microscopy, working with various cell-free protein expression platforms, and more - have enabled us to start working on projects that will greatly increase the capabilities of synthetic cells,

notably through the construction of a PURE-based membrane protein expression platform. Furthermore, by informing us of the experimental challenges that lay ahead with the proposed experimental approaches, this project has guided the development of alternative mechanisms for synthetic cell motility. Ultimately, this work has shed light on the creative approaches that will be required to engineer synthetic cells capable of complex functions.

4.6 Materials and methods

Preparation of electrocompetent *E. coli* DK8 cells

E. coli DK8 cells were obtained from Dr. Gabriele Deckers-Hebestreit (Universität Osnabrück, Germany). *E. coli* DK8 cells contain a knockout of the *unc* operon and do not natively encode for their own ATP synthase unless they are supplied with a plasmid encoding the protein complex, such as the pBH2 plasmid (see next section).

To make electrocompetent *E. coli* DK8 cells, we used the following protocol, slightly modified from Murray Lab in-house protocol:

1. Pre-chill all tubes and pipettes in the fridge at 4°C.
2. Autoclave (1) three 500 mL Erlenmeyer flasks filled with 450 mL MilliQ water and covered loosely with aluminum foil and (2) a 1 L bottle with 1 L MilliQ water and a loosely fastened lid to remove any residual detergents.
3. Prepare 500 mL LB Lennox and pre-warm it in an incubator at 37°C.
4. Inoculate 2 tubes of 5 mL LB Lennox with *E. coli* DK8 cells. Grow the overnight (about 14 hours).
5. To start a larger culture, first add 150 mL LB Lennox to each of the Erlenmeyer flasks. Then add about 1.5 mL overnight culture to each flask and incubate them at 37°C with with shaking at 220 rpm until the OD600 is about 0.5. This growth step should take about 3 hours.
6. Meanwhile, pre-chill a large floor centrifuge and tabletop centrifuge with appropriate rotors at 4°C. After dumping out the water from the autoclaved 1 L bottle of MilliQ water, rinse the bottle a few times with fresh MilliQ water, fill it with fresh MilliQ water, and chill it at 4°C.
7. Once the cultures have reached the appropriate OD600, pour the cultures into a 1 L centrifuge bottle.

8. Place the tubes on ice for 60 minutes. Change the ice at the 30-minute mark (or sooner) if the ice is melting. Note: an incubation time as little as 15 minutes may be sufficient, but to ensure the highest competency of the cells, we opted to incubate the full 60 minutes.

9. Perform the following set of steps two times, ensuring that cells are kept cold:

    - Centrifuge the bottle for 10 min at 2000*g* and 4°C.
    - Remove the supernatant completely.
    - Gently resuspend the cell pellet first with 20 mL cold MilliQ water, then with an additional 180 mL cold MilliQ water.

10. Incubate the cells on ice for 30 min.

11. Centrifuge the cells for 15 min at 2000*g* and 4°C.

12. While the cells are being centrifuged, prepare a 30 mL solution of 10% (v/v%) glycerol in ice cold MilliQ water.

13. Remove the supernatant completely and gently resuspend the pellet with 25 mL of the glycerol solution. Transfer the solution to a 50 mL conical tube.

14. Incubate the cells on ice for 30 min.

15. Centrifuge liposomes for 15 min at 1500*g* and 4°C.

16. Remove the supernatant completely and add 500 µL of 10% glycerol. Note: adjust that amount so that the cells are resuspended in a final volume of approximately 1 mL.

17. Create 50 uL aliquots of the cells in PCR tubes.

18. Flash-freeze the tubes in liquid nitrogen and store them at –80°C.

Transformation of electrocompetent *E. coli* DK8 cells

Once the *E. coli* DK8 cells were made electrocompetent, they were transformed with plasmids using the following protocol:

1. Incubate a 1.5 mL Eppendorf tube containing 450 µL SOC medium in a 37°C incubator.

2. Chill an electroporation cuvette on ice.

3. Thaw a 50 µL aliquot of electrocompetent *E. coli* DK8 cells.
4. Turn on the electroporator to the appropriate setting for bacteria.
5. Add 1.5 µL DNA to the cells and pipette up and down to mix.
6. Pipette the mixture of cells and DNA into the cuvette. Wipe excess moisture off the outside of the cuvette and immediately place it the cuvette in the electroporation chamber. Press the button to electroporate.
7. Pipette the pre-warmed SOC to the electroporated cells. Pipette up and down to mix and transfer the mixture back to the Eppendorf tube. Place the Eppendorf tube back into the 37°C incubator for 60 min.
8. While the cells are growing, place an LB agar plate with 100 µL/mL carbenicillen in a 37°C incubator.
9. Pipette 50 µL of the cell culture onto the pre-warmed LB agar plate. Add 3-4 glass beads, cover the plate, and shake the plate to spread the culture across the plate. Place the plate agar side up in an incubator overnight for roughly 16 hr at 37°C.
10. Pick three colonies to sequence-verify. Specifically, use those colonies to inoculate three 5 mL liquid cultures in LB media containing 100 µL/mL carbenicillin, grow the cultures overnight at 37°C and 200 rpm, and separately reserve 0.5 mL of each culture. Mini-prep the remaining 4.5 mL of each culture and send off the plasmid DNA for sequencing. Mix the remaining 0.5 mL of each culture with 0.5 mL of 50% glyercol solution in a cryogenic vial, label the vial, and store at –80°C. For each plasmid, keep one or more glycerol stocks corresponding to the correctly sequenced colonies.

ATP synthase purification

A plasmid containing the ATP synthase operon (*unc* operon, containing genes atpABCDEFGHI) was obtained from Dr. Gabriele Deckers-Hebestreit (Universität Osnabrück, Germany). The plasmid, pBH2, encodes for a cysteine-less ATP synthase with a His6x tag on the N-terminus of the β subunit protein (coded for by the atpD gene). ATP synthase was purified using the protocol established by Sobti and co-workers [33] with some modifications, as noted below.

In the preparation of buffers, described in the Materials section of the protocol, we noted the following:

- The term CV refers to column volume, which itself refers to bed volume, i.e., the amount of TALON resin that has been added to the column during purification. So for example, in section "3.2.2 Affinity Purification" in step 5 [33], we interpreted "Wash with(*sic*) column with 20 CV of buffer C" as "Wash column with 60 mL of buffer C."

- Digitonin was difficult to dissolve in buffers C, D, and E. To effectively dissolve the digitonin, for each buffer, we measured the amount of digitonin needed in grams, added it to an Eppendorf tube with 750-1000 µL of the appropriate buffer, and centrifuged it in a personal/mini microcentrifuge until the digitonin pellet completely dissolved. The entire solution was then transferred to the larger bottle/tube of buffer, and the Eppendorf tube was washed several times to transfer any residual digitonin to the main container for the buffer.

- As the volume of buffer D we made was very small (7 mL), we did not vacuum-filter buffer D as we did for buffers C and E. However, we assumed that any precipitate in buffer D would have settled to the bottom of the Falcon tube we used to store the buffer, so extra care was taken to pipette out buffer D during the elution step of the protocol to ensure 1 mL remained in the tube.

In the Expression subsection of the Methods section [33], the following modifications/clarifications to the protocol were made:

- ATP synthase was expressed in *E. coli* DK8 cells expressing the pBH2 plasmid rather than the pFV2 plasmid.

- 100 µL/mL carbenicillin was used instead of ampicillin.

- The plating steps were skipped. A pipette tip was used to directly inoculate three 6 mL liquid cultures of LB medium from a glycerol stock, which were later combined and split equally to inoculate four 1.5 L cultures.

- The large cultures were grown at 37°C and 220 rpm (rather than 150 rpm).

- To harvest the cells, the liquid cultures were first distributed across six 1 L bottles and centrifuged in a pre-chilled centrifuge for 15 min at 5000*g* and 4°C. Most of the supernatant was removed from the cultures, leaving about 30 mL, and the bottles were placed on ice. The remaining amount of supernatant in each bottle was used to resuspend the cell pellet, and a serological pipette

was used to transfer the resuspended cell cultures to 3-6 50 mL conical tubes. The tubes were then centrifuged in a pre-chilled centrifuge for 15 min at 5000g and 4°C. Finally, the supernatant was removed and the pellets were flash-frozen in liquid nitrogen and stored at –80°C.

In the Protein Purification subsection of the Methods section [33], the following modifications/clarifications to the protocol were made:

- As the DNase I was purchased from New England Biolabs, it did not have a concentration written on the tube. During the step of resuspension of cells in buffer A, 100 uL of DNase I was added along with 200 uL of the 10X reaction buffer supplied with the tube. These volumes were arbitrarily chosen.
- During membrane preparation, to perform the freeze-thaw cycles, the 100 mL cell mixture was flash-frozen in liquid nitrogen in 50 mL conical tubes and thawed in tube rack in a room-temperature water bath.
- The membrane was pelleted by ultracentrifugation at 38000 rpm in a Type 45 Ti Rotor (Beckman Coulter).
- During affinity purification, the membrane pellet was resuspended with a soft bristle paintbrush.
- During affinity purification, when incubating the supernatant with TALON beads, the whole column was placed on a rocking platform (nutator) and positioned to allow the fluid inside to rock and forth from one end of the column to the other.
- When using the Amicon 100 kDa MWCO centrifugal concentrator, the sample was centrifuged at 4000g in 30-60 sec intervals and pipetted up and down between each spin. These steps were performed to help prevent adsorption of the protein onto the walls of the concentrator and aggregation of the protein complexes.
- Size-exclusion chromatography was performed by staff at the Caltech Protein Expression Center. As a consequence, eluted fractions were stored overnight at 4°C until they could be retrieved the next day. In subsequent purifications, the size-exclusion chromatography step was skipped. The concentrations obtained after purification ranged from 400-800 µg/mL.

Preparation of DOPC liposomes for ATP synthase reconstitution

Liposomes made from 1,2-dioleoyl-sn-glycero-3-phosphocholine (DOPC) and Lissamine Rhodamine B, DHPE (LissRhodB) were made using the following protocol. To a 50 mL beaker in a fume hood, 600 µL of 25 mg/mL DOPC in chloroform was combined with 15 µL of 1 mg/mL LissRhodB, and the beaker was swirled to mix the lipids. Next, the chloroform was evaporated by placing the beaker in a metal bead bath in the fume hood at 55°C for 2 h, after which the beaker was removed and cooled for 10 min. Next, 1 mL of ice-cold Buffer F (100 mM KCl, 50 mM MOPS pH 7.4, and 1 mM $MgCl_2$) to the lipid thin film, the beaker was covered with Parafilm, and the beaker was vortexed at the maximum setting for 3 min continuously.

To reduce the size and lamellarity of the liposomes, the liposome solution was transferred to a 2 mL cryogenic tube and six freeze-thaw cycles were performed. For each cycle, the tube was placed in liquid nitrogen for 1 min, thawed in a metal bead bath at 30°C for 30 min, and vortexed at the maximum setting for 30 s.

Finally, the liposomes were reduced further in size to 100 nm using an extruder. A 100 nm extruder membrane was first pre-wet with Buffer F, after which liposomes were pushed across the membrane 21 times. Once liposomes were verified via microscopy at 100X zoom, they were stored in aliquots of 52 µL in PCR tubes, flash-frozen in liquid nitrogen, and stored at –80°C until further use.

Reconstitution of ATP synthase into liposome membranes

Liposomes were reconstituted using the protocol established by Sobti and coworkers [33] with some modifications and clarifications as noted. Prior to the reconstitution, 100 nm liposomes were made as described in the previous step. Additionally, Sephadex G50 was swelled in MilliQ water for 1 h; swelling the Sephadex G50 overnight was found to result in bacterial contamination, so fresh Sephadex G50 was swelled the day it was needed.

For the reconstitution, 300 µL of liposomes and 200 µL of Buffer F (100 mM KCl, 50 mM MOPS pH 7.4, and 1 mM $MgCl_2$) were added to a cuvette kept on ice. Next, 170 µL of 0.75 mg/mL purified ATP synthase was added. The solution was mixed well, and the OD650 was measured. Next, 0.1 mg/mL sodium cholate was slowly titrated at about 0.5 µL at a time, followed by pipetting to mix the liposome solution, a 5-min incubation on ice, and a subsequent OD650 measurement. Once a roughly 16% drop in OD650 was achieved, this procedure was terminated; the total volume of sodium cholate added was about 10 µL. For control samples, the procedure was

repeated, albeit with 300 µL Buffer E (20 mM Tris/Cl pH 8.0, 100 mM NaCl, 1 mM digitonin, and 2 mM $MgCl_2$) instead of liposomes, and using the same volume of sodium cholate added to the liposome samples.

To remove the detergent from the samples, a 3 mL plastic column was first filled with about 1 mL final volume of the Sephadex G50 beads and pre-equilibrated with 10 mL of Buffer F (100 mM KCl, 50 mM MOPS pH 7.4, and 1 mM $MgCl_2$). Next, the liposome solution was added to the column, and turbid (in this case, pink) fractions were collected. An additional 1 mL or more of Buffer F was added until the column ran clear. This procedure was repeated with a new column for the control sample. Finally, each sample was centrifuged at 100000*g* (75000 rpm using a TLA-100.3 rotor). Their supernatants were discarded, and each liposome sample was resuspended in 1 mL of buffer F. Finally, the liposomes were stored in aliquots of 52 µL, flash-frozen, and stored at –80°C until further use. Although not required, ATP synthase's presence in proteoliposome membranes can be verified by running the proteoliposome on an SDS-PAGE protein gel and using a standard stain (e.g., SimplyBlue SafeStain).

ACMA quenching assay

ATP synthase activity in proteoliposome membranes was measured using the ACMA quenching assay described Sobti and co-workers [33] with some modifications and clarifications as noted to adapt the assay for a plate reader. 241 µL of buffer F was mixed with 2.5 µL 100 µM ACMA, 50 µL of either liposomes or proteoliposomes, and 0.25 uL of one of the following: 100% EtOH (two samples per liposome type) or 50 mM DCCD dissolved in 100% EtOH (one sample per liposome type). The liposomes were incubated for 1 h at room temperature, covered to protect them from light, on a platform shaker. Next, to a 96-well glass-bottom plate, 250 µL of each of the six samples was added to a separate well.

Once the plate was in the plate reader, the following protocol as used. First, a fluorescence read was taken to normalize time-course values by the number of liposomes present in a well (excitation: 560 nm, emission: 583 nm, optics: bottom, gain: 61). Next, a kinetic run was performed to get baseline fluorescence readings for each sample (a run was performed for 3 min with reads taken every 20 s using the following settings - excitation: 419 nm, emission: 483 nm, optics: bottom, gain: 61). Next, the plate was removed, 5 µL 10 mM ATP was added to each well, and the plate was re-inserted into the plate reader. The kinetic run was then repeated,

albeit for 10 min at 10 s intervals, with 3 s of linear shaking performed prior to each read. For one of the 100% EtOH samples for each liposome type, MilliQ water was added instead, to ensure that any fluorescence drop was due to the addition of ATP. The expected result is that fluorescence drops dramatically after the addition of ATP only in the proteoliposome sample with no DCCD (i.e., 100% EtOH instead) and with ATP added instead of MilliQ water.

Actin polymerization and visualization via TIRF microscopy

Actin was reconstituted and polymerized using a protocol and materials from Cytoskeleton, Inc. with one modification as noted. Instead of using just pyrene actin, an actin solution was prepared in G-buffer (General Actin Buffer supplemented with 0.2 mM ATP and 1 mM DTT) at a concentration of 0.45 mg/mL, at a mass ratio of 10:1:1 of pyrene actin to biotin actin to rhodamine actin. Polyermization was performed as per the provided protocol.

A previously described protocol was used for silanization of glass coverslips and preparation of microfluidic chambers for TIRF microscopy of actin filaments [34]. For the functionalization of the coverslip for actin filament attachment, a slightly modified protocol from the original paper was used [34]. First, goat anti-biotin antibodies at 1 mg/mL in PBS were introduced into a flow cell of the microfluidic chamber and immobilized on the surface for 10 min. Next, 1% Pluronic F127 in Brb80 buffer (80 mM PIPES, 1 mM $MgCl_2$, 1 mM EGTA) was perfused into the flow cell. After 30 min, the chamber was rinsed with Brb80 and actin was introduced, either in the form of monomeric G-actin supplemented with actin polymerization buffer or polymerized F-actin alone. Finally, the excess actin was washed away with Brb80 and then Brb20 (20 mM PIPES, 1 mM $MgCl_2$, 1 mM EGTA). The flow cell channels were sealed on each end with clear acrylic nail polish to prevent evaporation during TIRF microscopy. Finally, TIRF microscopy was performed using a Nikon Ti2-E Motorized Inverted confocal microscope with TIRF and STORM capabilities under a 100X objective.

Attachment of actin filaments to proteoliposomes

Actin filaments were attached to proteoliposomes using two different methods: polymerizing actin filaments onto proteoliposomes and incubating polymerized actin filaments with proteoliposomes.

The following protocol was used to polymerize actin filaments onto proteoliposomes:

1. Proteoliposomes and control liposomes (of the same lipid composition and treated with the reconstitution protocol albeit without the addition of ATP synthase) were thawed on ice and pelleted by centrifugation at 100g for 15 min. Their supernatant was removed.

2. About 25 µL of liposome pellet was resuspended with a 100 µL solution of 1 (w/v)% (equivalent to 0.01 g/mL) bovine serum albumin (BSA) in 1X phosphate-buffered solution (PBS) in a 1.5 mL microcentrifuge tube.

3. An additional 1.2 mL of PBS was added, and liposomes were centrifuged at 14000g for 10 min at room temperature. The supernatant was removed, the pellet was resuspended in 1 mL PBS, and the liposomes were centrifuged at 14000g for 5 min at room temperature to remove any residual BSA. Note: liposomes did not pellet without this PBS addition.

4. The pellet was resuspended with 1 mL PBS supplemented with 1 µL of 1 mg/mL biotin anti-His6x mouse antibody (Biolegend, Cat #906103), with the mixture pipetted well to mix thoroughly. The liposomes were incubated at room temperature for 1 h.

5. After the incubation, the liposomes were centrifuged at 14000g for 10 min at room temperature and the supernatant was removed. The pellet was resuspended in 1 mL PBS, and the liposomes were centrifuged again, albeit at 14000g for 5 min at room temperature, to remove any residual antibody.

6. G-actin was prepared as described in the **Actin polymerization and visualization via TIRF microscopy** section above.

7. 1 µof the liposome pellet was mixed with 60 µL of G-actin containing 1 µg/mL streptavidin (i.e., 0.6 µL of 0.1 mg/mL streptavidin was mixed in at the time of adding the liposomes). The whole mixture was pipetted up and down to mix.

8. 6 µL of actin polymerization buffer was added, and the mixture was pipetted up and down to mix. The mixture was incubated for 20 min at room temperature.

9. Flow channels were prepared as previously described [34], and about 15 µL of the liposome mixture was loaded into the flow channels. The ends of the flow channel were sealed with clear acrylic nail polish, and the liposomes

were imaged under a Nikon Ti2-E Motorized Inverted confocal microscope using a 100X objective.

When incubating polymerized actin filaments with proteoliposomes, the same protocol was used as the one above, with one exception. The actin was first polymerized in a separate tube as described in the **Actin polymerization and visualization via TIRF microscopy** section. After incubating the mixture for 30 min, the liposomes were loaded into the flow channel and imaged.

Rotation of actin filaments attached to coverslip-bound ATP synthase

Slides were cleaned and dried as described in a previously published protocol [34]. Flow cells were also prepared as described, but silanization and other steps were omitted.

The actin rotation assay was performed as described in a previously published protocol [25]. Briefly, 600 µL/mL (0.96 µM) purified ATP synthase was incubated with 100 µM biotin maleimide for 1 h at 4°C. Next, a solution of 0.8 µM Ni-NTA HRP conjugate in Buffer A* (Buffer A as described in the protocol but without BSA or Triton X-100) was made, perfused into the flow cell, and incubated for 5 min. To minimize non-specific binding, a solution of 1 (w/v)% Pluronic F127 in Buffer A was perfused into the channel and incubated for 30 min. Next, the biotinylated ATP synthase was diluted to 10 nM in Buffer A, perfused into the flow channel, and incubated for 10 min. Next, Streptavidin AlexaFluor 647 was diluted from its 2 mg/mL stock solution to 4 µM in Buffer A, perfused into the flow channel, and incubated for 5 min. Next, the flow channel was washed with Buffer A to remove any unbound streptavidin.

Pyrene-biotin-rhodamine actin was added either as (1) monomeric G-actin, prepared as described in the section above and supplemented immediatelty before use with polymerization buffer in a 1:10 ratio of polymerization buffer to actin, or as (2) pre-polymerized F-actin. The actin was perfused in and incubated in the flow channel for 20 min. Finally, immediately before loading the microfluidic chamber onto a microscope, a simplified reaction mixture for rotation (100 mM ATP and 1% β-mercaptoethanol in Buffer A) was perfused into the flow channel. (Note: the addition of the other components from the original protocol, antioxidants and energy regeneration components, did not change the outcome of the assay). The reaction mixture for rotation was perfused into the channel in increments of 15 µL, with more of the mixture being added until the unbound filaments had washed away.

Preparation of the pMK2 plasmid

To express ATP synthase under a P_{T7} promoter, an additional plasmid containing the ATP synthase operon (*unc* operon, containing genes atpABCDEFGHI) was first obtained from Dr. Gabriele Deckers-Hebestreit (Universität Osnabrück, Germany). The plasmid, pBH2.2, encodes for a cysteine-less ATP synthase and is derived directly from the pBWU13 plasmid, which has been used canonically for ATP synthase expression and purification. Next, the ATP synthase coding region (starting directly from the beginning of the *atpI* gene to a few bases after the end of the *atpC* gene) was PCR-amplified, purified using a DNA gel extraction, and annealed to a pET21(+) backbone a using Gibson assembly to form the pMK2 plasmid. The backbone contains a P_{T7} promoter and T7 terminator. The pMK2 plasmid was sequence-verified by Nanopore sequencing prior to use.

***In vitro* expression of membrane proteins**

Cell-free expression of ATP synthase was performed in three different cell-free systems: (1) a commercial New England Biolabs (NEB) PURExpress system, and (2) an *E. coli* NiCo21 cell lysate-based system (see above for details of how cell lysate was prepared), and (3) *E. coli* NiCo21 cell lysate-based system without methionine added to the reaction mixture.

Lysate-based cell-free reactions were prepared as per the protocol by Sun and co-workers [36]. Unless otherwise noted, each 10 µL reaction consisted of the following: 33% (by volume) of cell lysate, 1.5 mM of each amino acid (except for leucine, which was added at 1.25 mM), 4.8 nM of NTP mix (containing 1.5 mM each of ATP and GTP, 0.9 mM each of CTP and UTP, pH adjusted to 7.5 using KOH), 50 mM HEPES pH 8, 0.2 mg/mL tRNA, 0.26 mM coenzyme A, 0.33 mM NAD+, 0.75 mM cyclic AMP (cAMP), 0.068 mM folinic acid, 1 mM spermidine, 0.05X ^{35}S-methionine (using a 1X stock solution of Methionine, L-[35S]-EasyTag, 5 mCi (Revvity #NEG709A005MC)), 30 mM 3PGA, 10 mM magnesium glutamate and 100 mM potassium glutamate; these salt concentrations were chosen because they optimized deGFP expression in TX-TL reactions supplied with 1 nM P_{OR1OR2}-deGFP plasmid for this batch of cell lysate. Finally, a variable amount of pMK2 plasmid was added, and the remaining volume of the 10 µL of reaction mixture was filled with nuclease-free water. Reactions were incubated at 30 °C for 18 h.

NEB PURExpress reactions were prepared as per the standard protocol included with the kit, albeit with the addition of 0.025X RNAsin Ribonuclease Inhibitor

(Promega #N2111) and 0.05X ^{35}S-methionine. The pMK2 plasmid was added at a concentration of 1.25 nM. Reactions were incubated for 2 h at 37 °C.

After the cell-free reactions were performed, proteins were denatured via a 15X dilution in SDS and subsequent incubation at 65 °C and loaded onto a SDS-PAGE protein gel. After the gel was run at 120 V for about 60-90 min, the gel was dried at 80°C for 30 min in a gel dryer. The gel was finally analyzed using phosphor screen autoradiography.

Acknowledgments

The idea of propelling a liposome by a repurposed ATP synthase motor with an attached filament came out of synthetic cell discussions among the faculty at Caltech (Austin Minnich, Richard Murray) and Imperial College London (Oscar Ces, Yuval Elani, Tom Ellis, and Paul Freemont), and we thank them for their contributions, both direct and indirect, to this work. We would especially like to thank Prof. Yuval Elani and his group for feedback on the proposed work prior to grant submission and later during Caltech-Imperial meetings.

We would also like to thank Zoila Jurado and Miki Yun for extensive experimental training and feedback throughout this project. Learning how to make liposomes and perform membrane protein purification, especially of a large protein complex like ATP synthase (and during a pandemic when close contact with colleagues was limited!), would have been impossible without their guidance.

We would further like to thank Prof. Gabriele Deckers-Hebestreit (Universität Osnabrück, Germany) for providing the ATP synthase plasmids and *E. coli* DK8 strain used in this study. Prof. Deckers-Hebestreit provided extensive information regarding the use of these parts, including annotated sequence information, and we thank her and her lab for sending these parts.

We would additionally like thank the following individuals/facilities for their help: Prof. Rebecca Voorhees and Masami Hazu, for allowing us to use their lab and assisting us in performing the radioactive labeling experiment whose result is shown in Figure 4.11; Prof. Doug Rees and Allen Lee, for training and allowing us to use their ultracentrifuges, which was necessary for membrane protein purification and reconstitution; Giada Spigolon and the Caltech Beckman Imaging Facility, for assisting us in getting trained in TIRF microscopy; and Annie Lam and the Caltech Protein Expression Center, for their assistance in performing cell lysis with a cell disruptor and performing size-exclusion chromatography of samples.

Research was sponsored by the National Science Foundation (NSF) under Award Number 2039277. The views and conclusions contained in this document are those of the authors and should not be interpreted as representing the official policies, either expressed or implied, of the U.S. Government. The U.S. Government is authorized to reproduce and distribute reprints for Government purposes notwithstanding any copyright notation herein.

4.7 Supporting information

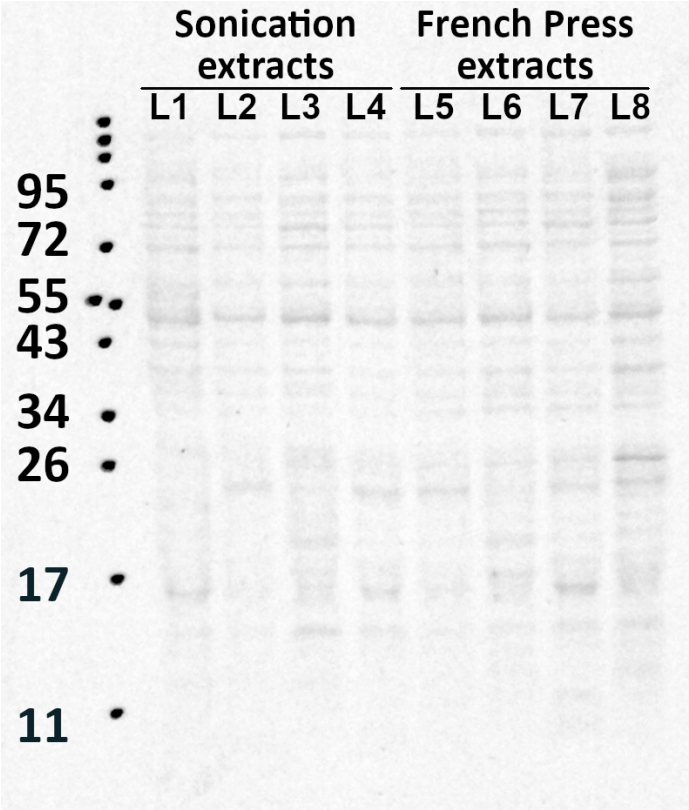

Figure S4.1: *In vitro* expression of unknown proteins in cell-free systems containing 35S-methionine. TX-TL systems prepared from 8 different batches of cell lysate were supplied with no DNA but still showed bands on an SDS-PAGE gel subjected to autoradiography, suggesting the expression of proteins from genomic DNA lingering in the cell lysate. The lanes corresponding to TX-TL systems using cell lysate prepared as described. L1-L4: lysates were prepared from cells lysed by sonication. L5-L8: lysates were prepared from cells lysed by French press. All lysates were prepared from *E. coli* Rosetta2 cells except for the lysate in L1, which was prepared from *E. coli* NiCo21 cells. The lysates in L4 and L6 were dialyzed against S30B buffer before use in TX-TL reactions [36].

References

[1] Xavier Trepat, Zaozao Chen, and Ken Jacobson. "Cell migration." eng. In: *Comprehensive Physiology* 2.4 (2012), pp. 2369–2392. ISSN: 2040-4603. DOI: 10.1002/cphy.c110012.

[2] Makoto Miyata et al. "Tree of motility – a proposed history of motility systems in the tree of life." eng. In: *Genes to Cells* 25.1 (2020), pp. 6–21. ISSN: 1365-2443 1356-9597. DOI: 10.1111/gtc.12737.

[3] Sara Araújo et al. "From soil to surface water: exploring *Klebsiella's* clonal lineages and antibiotic resistance odyssey in environmental health." eng. In: *BMC microbiology* 25.1 (2025), p. 97. ISSN: 1471-2180. DOI: 10.1186/s12866-025-03798-8.

[4] Zuzanna M. Abdala et al. "Examining ecological succession of diatoms in California current system cyclonic mesoscale eddies." In: *Limnology and Oceanography* 67.11 (2022), pp. 2586–2602. ISSN: 0024-3590. DOI: 10.1002/lno.12224.

[5] Marianne Lintz, Adam Muñoz, and Cynthia A. Reinhart-King. "The mechanics of single cell and collective migration of tumor cells." eng. In: *Journal of biomechanical engineering* 139.2 (2017), pp. 0210051–0210059. ISSN: 1528-8951 0148-0731. DOI: 10.1115/1.4035121.

[6] L. David Sibley. "Invasion and intracellular survival by protozoan parasites." eng. In: *Immunological reviews* 240.1 (2011), pp. 72–91. ISSN: 1600-065X 0105-2896. DOI: 10.1111/j.1600-065X.2010.00990.x.

[7] Vibhuti Agrahari et al. "Intelligent micro-/nanorobots as drug and cell carrier devices for biomedical therapeutic advancement: promising development opportunities and translational challenges." In: *Biomaterials* 260 (2020), p. 120163. ISSN: 0142-9612. DOI: 10.1016/j.biomaterials.2020.120163.

[8] Tayssir Kadri et al. "Nanoencapsulation and release study of enzymes from *Alkanivorax borkumensis* in chitosan-tripolyphosphate formulation." In: *Biochemical Engineering Journal* 137 (2018), pp. 1–10. ISSN: 1369-703X. DOI: 10.1016/j.bej.2018.05.013.

[9] Kai Jin et al. "Engineered bacteria for disease diagnosis and treatment using synthetic biology." In: *Microbial Biotechnology* 18.1 (2025), e70080. ISSN: 1751-7915. DOI: 10.1111/1751-7915.70080.

[10] David J. Lea-Smith et al. "Engineering biology applications for environmental solutions: potential and challenges." In: *Nature Communications* 16.1 (2025), p. 3538. ISSN: 2041-1723. DOI: 10.1038/s41467-025-58492-0.

[11] Sungwoo Jeong et al. "Toward artificial cells: novel advances in energy conversion and cellular motility." In: *Advanced Functional Materials* 30.11 (2020), p. 1907182. ISSN: 1616-301X. DOI: 10.1002/adfm.201907182.

[12] Lynn J. Rothschild et al. “Building synthetic cells - from the technology infrastructure to cellular entities.” In: *ACS Synthetic Biology* (2024). DOI: 10.1021/acssynbio.3c00724.

[13] Zihan Wang et al. “Soft bio-microrobots: toward biomedical applications.” In: *Advanced Intelligent Systems* 6.2 (2024), p. 2300093. ISSN: 2640-4567. DOI: 10.1002/aisy.202300093.

[14] Nobuhito Mori, Kaori Kuribayashi, and Shoji Takeuchi. “Artificial flagellates: analysis of advancing motions of biflagellate micro-objects.” In: *Applied Physics Letters* 96.8 (2010), p. 083701. DOI: 10.1063/1.3327522.

[15] Anders N Albertsen, Jan K Szymański, and Juan Pérez-Mercader. “Emergent properties of giant vesicles formed by a polymerization-induced self-assembly (PISA) reaction.” In: *Scientific Reports* 7.1 (2017), pp. 1–8. DOI: 10.1038/srep41534.

[16] Takaaki Miura et al. “Autonomous motion of vesicle via ion exchange.” In: *Langmuir: The ACS Journal of Surfaces and Colloids* 26.3 (2010), pp. 1610–1618. DOI: 10.1021/la9038599.

[17] Kan Shoji and Ryuji Kawano. “Osmotic-engine-driven liposomes in microfluidic channels.” In: *Lab on a Chip* 19.20 (2019), pp. 3472–3480. DOI: 10.1039/C9LC00788A.

[18] Chapin S. Korosec et al. “Motility of an autonomous protein-based artificial motor that operates via a burnt-bridge principle.” In: *Nature Communications* 15.1 (2024), p. 1511. ISSN: 2041-1723. DOI: 10.1038/s41467-024-45570-y.

[19] Marcos F. Velho Rodrigues, Maciej Lisicki, and Eric Lauga. “The bank of swimming organisms at the micron scale (BOSO-Micro).” In: *PLOS ONE* 16.6 (2021), e0252291. DOI: 10.1371/journal.pone.0252291.

[20] Navish Wadhwa and Howard C. Berg. “Bacterial motility: machinery and mechanisms.” In: *Nature Reviews Microbiology* 20.3 (2022), pp. 161–173. ISSN: 1740-1534. DOI: 10.1038/s41579-021-00626-4.

[21] Hiroyuki Terashima et al. “*In vitro* autonomous construction of the flagellar axial structure in inverted membrane vesicles.” In: *Biomolecules* 10.1 (2020), p. 126. ISSN: 2218-273X. DOI: 10.3390/biom10010126.

[22] Prashant Neupane et al. “ATP synthase: structure, function and inhibition.” In: *Biomolecular Concepts* 10.1 (2019), pp. 1–10. DOI: 10.1515/bmc-2019-0001.

[23] Kazuaki Nishio et al. “Subunit rotation of ATP synthase embedded in membranes: a or β subunit rotation relative to the c subunit ring.” In: *Proceedings of the National Academy of Sciences* 99.21 (2002), pp. 13448–13452. DOI: 10.1073/pnas.202149599.

[24] Hiroyuki Noji et al. “Direct observation of the rotation of F1-ATPase.” In: *Nature* 386.6622 (1997), pp. 299–302. ISSN: 1476-4687. DOI: 10.1038/386299a0.

[25] Yoshihiro Sambongi et al. “Mechanical rotation of the c subunit oligomer in ATP Synthase (F_OF_1): direct observation.” In: *Science* 286.5445 (1999), pp. 1722–1724. DOI: 10.1126/science.286.5445.1722.

[26] Sabina Deutschmann, Lukas Rimle, and Christoph von Ballmoos. “Rapid estimation of membrane protein orientation in liposomes.” In: *ChemBioChem* 23.2 (2022), e202100543. DOI: 10.1002/cbic.202100543.

[27] Lado Otrin et al. “En route to dynamic life processes by SNARE-mediated fusion of polymer and hybrid membranes.” In: *Nature Communications* 12.1 (2021), p. 4972. ISSN: 2041-1723. DOI: 10.1038/s41467-021-25294-z.

[28] Samuel Berhanu, Takuya Ueda, and Yutetsu Kuruma. “Artificial photosynthetic cell producing energy for protein synthesis.” In: *Nature Communications* 10.1 (2019), p. 1325. ISSN: 2041-1723. DOI: 10.1038/s41467-019-09147-4.

[29] Daichi Okuno, Ryota Iino, and Hiroyuki Noji. “Rotation and structure of FoF1-ATP synthase.” In: *The Journal of Biochemistry* 149.6 (2011), pp. 655–664. ISSN: 0021-924X. DOI: 10.1093/jb/mvr049.

[30] Robert H Fillingame et al. “Synthesis of a functional F0 sector of the *Escherichia coli* H+-ATPase does not require synthesis of the alpha or beta subunits of F1.” In: *Journal of Bacteriology* 165.1 (1986), pp. 244–251. DOI: 10.1128/jb.165.1.244-251.1986.

[31] Doreen Matthies et al. “Cell-free expression and assembly of ATP synthase.” In: *Journal of Molecular Biology* 413.3 (2011), pp. 593–603. ISSN: 0022-2836. DOI: 10.1016/j.jmb.2011.08.055.

[32] Tracy Palmer and Ben C. Berks. “The twin-arginine translocation (Tat) protein export pathway.” In: *Nature Reviews Microbiology* 10.7 (2012), pp. 483–496. ISSN: 1740-1534. DOI: 10.1038/nrmicro2814.

[33] Meghna Sobti, Robert Ishmukhametov, and Alastair G Stewart. “ATP synthase: expression, purification, and function.” In: *Protein Nanotechnology*. New York, NY: Humana, 2020, pp. 73–84. DOI: 10.1007/978-1-4939-9869-2_5.

[34] Michał Szkop, Beata Kliszcz, and Andrzej A. Kasprzak. “A simple and reproducible protocol of glass surface silanization for TIRF microscopy imaging.” In: *Analytical Biochemistry* 549 (2018), pp. 119–123. ISSN: 0003-2697. DOI: 10.1016/j.ab.2018.03.020.

[35] Yoshihiro Shimizu et al. “Cell-free translation reconstituted with purified components.” In: *Nature Biotechnology* 19.8 (2001), pp. 751–755. ISSN: 1546-1696. DOI: 10.1038/90802.

[36] Zachary Z. Sun et al. “Protocols for implementing an *Escherichia coli* based TX-TL cell-free expression system for synthetic biology.” In: *JoVE* 79 (2013), e50762. ISSN: 1940-087X. DOI: 10.3791/50762.

[37] Martin Silberberg. *Principles of General Chemistry*. 3rd. New York, NY, USA: McGraw-Hill, 2013. ISBN: 978-0-07-340269-7.

[38] Kouhei Tsumoto and Jose M.M. Caaveiro. “Antigen–antibody binding.” In: *eLS*. John Wiley and Sons, Ltd, 2016, pp. 1–8. ISBN: 9780470015902. DOI: 10.1002/9780470015902.a0001117.pub3.

[39] Thom Vreven et al. “Prediction of protein–protein binding free energies.” In: *Protein Science* 21.3 (2012), pp. 396–404. DOI: 10.1002/pro.2027.

[40] Laura Grasemann et al. “OnePot PURE cell-free system.” In: *Journal of Visualized Experiments* 172 (2021), e62625. ISSN: 1940-087X. DOI: 10.3791/62625.

[41] Gabriele Deckers-Hebestreit. “Assembly of the *Escherichia coli* FoF1 ATP synthase involves distinct subcomplex formation.” In: *Biochemical Society Transactions* 41.5 (2013), pp. 1288–1293. ISSN: 0300-5127. DOI: 10.1042/BST20130096.

[42] Ross E. Dalbey and Andreas Kuhn. “Membrane insertases are present in all three domains of life.” In: *Structure* 23.9 (2015), pp. 1559–1560. ISSN: 0969-2126. DOI: 10.1016/j.str.2015.08.002.

[43] Masaru Sasaki et al. “The bacterial protein YidC accelerates MPIase-dependent integration of membrane proteins.” In: *Journal of Biological Chemistry* 294.49 (2019), pp. 18898–18908. ISSN: 0021-9258. DOI: 10.1074/jbc.RA119.011248.

Chapter 5

CONCLUSION

The work in the preceding chapters has attempted to address many critical gaps in synthetic cell research — irreproducibility, lack of predictability, subsystem integration, and a need for autonomous, programmable functionalities. In doing so, this work has highlighted many design considerations for synthetic cells.

In Chapter 2, we show how specific TX-TL reaction components contribute to variability in TX-TL performance. We further show that TX-TL performance is constrained in energy availability, resulting in a trade-off between transcription and translation. As users begin to implement more complex biomolecular programs in synthetic cells, they must consider how to use these insights to minimize variability and maximize performance in their systems. Regarding variability, beyond traversing the performance space by modifying the concentrations of TX-TL components as per our suggested guidelines, another promising approach is to design biomolecular programs that are robust to cell-free metabolic variability over ranges that are typical in lab preparations of cell lysate. Regarding performance, biomolecular programs can be designed keeping in mind energy limitations. Alternatively, NTP-fueled systems without 3PGA can be further explored to determine whether these systems are better for biomolecular programs with higher energy requirements.

In Chapter 3, we provide a methodology for adapting and fine-tuning an existing TX-TL model for improved predictability in new experimental contexts. We show early work that suggests that synthetic cell users looking to design and implement their own programs can readily adapt the model to their own systems, although it remains to be determined whether the approach is sufficient for predicting performance of complex biomolecular programs. In the case of complex TX-TL programs, it will still be necessary to perform additional experiments to determine parameter values corresponding to expression of individual proteins (similar work has been achieved previously [1]), after which a more complex (and hopefully predictive) model can be built. In the case biophysical programs such as genetically-driven synthetic cell division, a promising approach is to combine the Poole model (see Reference [2]) with biophysical models using tools like Vivarium [3].

In Chapter 4, we propose a design by which autonomous, programmable motility can

be realize in synthetic cells by combining energy and motility subsystems. Although our efforts were largely unsuccessful, we show preliminary work suggesting that ATP synthase may be expressed in PURExpress, a minimal TX-TL system, and that filaments can be attached to proteins in liposome membranes. We further highlight several design considerations for continuing this work or similar work, such as considerations for using an immunolabeling protocol to attach filaments to liposomes and for development of a PURE-based membrane protein expression platform using SecYEG (or other Sec proteins), YidC, and MPIase. A particularly promising approach, both for this project and for designing synthetic cells, is to consider using proteins that are wildly different than those seen in nature, such as ATP synthase variants with missing subunits.

The future of synthetic cell research

Beyond these design considerations, as we look to the future, there are many more promising avenues in synthetic cell research. Perhaps the most promising is artificial intelligence-guided protein design and evaluation, which can open up the protein design space considerably [4]. In due time, synthetic cell users will be able to use AI to design proteins that are less promiscuous (i.e., only perform one function), smaller (and therefore less burdensome for TX-TL systems to produce), and more effective at their function, enabling synthetic cells that are more capable and more efficient.

Another useful approach includes looking beyond *E. coli*, from which many synthetic cell components have been derived, to nature, which offers an abundance of biomolecular parts that can be used in synthetic cells. Some previous work has not only utilized components from non-*E. coli* organisms but also combined components from different organisms, such as a synthetic cell containing bacteriorhodopsin from *Halobacterium salinarum* and ATP synthase from *Bacillus* PS3 [5]. As we begin to sequence the genome and proteome of more organisms, including extremophiles, the set of novel or improved components available for use in synthetic cells will rapidly expand, as will the functionalities of synthetic cells.

As we look beyond understanding life as we know it, a final consideration in designing synthetic cells is less a technical approach and more a useful thought exercise pertaining to the two previous points. Once we overcome some of the challenges and adopt approaches like the ones I have highlighted in this chapter, I argue that we can and should begin to think more freely about what we want a synthetic cell to be.

For example, how might we implement cell division using a novel, more efficient implementation? How might we implement a function in synthetic cells that is not found anywhere in nature? How might we design a collection of synthetic cells that rapidly self-assemble to form a novel synthetic life form? Perhaps most importantly, at what point does this research start to become an ethical concern? As research in the field progresses, addressing these types of questions can help us to ethically navigate the boundaries of life and engineer synthetic cells to benefit mankind.

References

[1] Vipul Singhal. "Modeling, computation, and characterization to accelerate the development of synthetic gene circuits in cell-free extracts." PhD Thesis. California Institute of Technology, 2019.

[2] William Poole. "Compilation and inference with chemical reaction networks." PhD Thesis. California Institute of Technology, 2021.

[3] Eran Agmon et al. "Vivarium: an interface and engine for integrative multiscale modeling in computational biology." In: *Bioinformatics* 38.7 (2022), pp. 1972–1979. DOI: 10.1093/bioinformatics/btac049.

[4] Arjuna M Subramanian et al. "Unexplored regions of the protein sequence-structure map revealed at scale by a library of foldtuned language models." In: *bioRxiv* (2025), pp. 2023–12. DOI: 10.1101/2023.12.22.573145.

[5] Samuel Berhanu, Takuya Ueda, and Yutetsu Kuruma. "Artificial photosynthetic cell producing energy for protein synthesis." In: *Nature Communications* 10.1 (2019), p. 1325. ISSN: 2041-1723. DOI: 10.1038/s41467-019-09147-4.